GESP-7025
DEC 1969

SPACE SYSTEMS

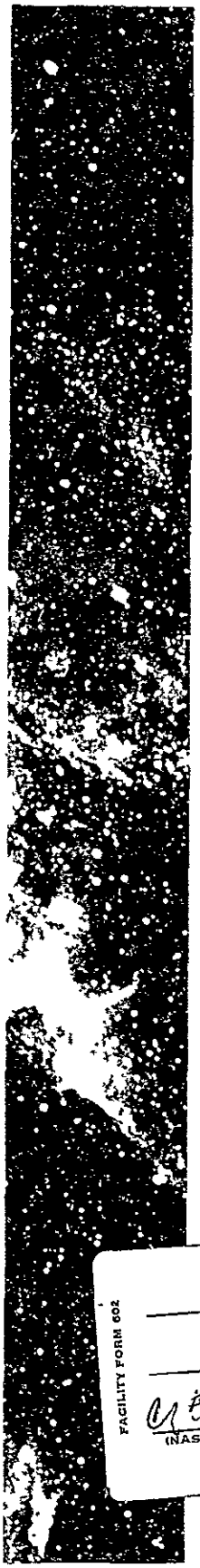

A DESIGN STUDY FOR A MAGNETOHYDRODYNAMIC POWER SYSTEM FOR A NUCLEAR ELECTRIC PROPELLED UNMANNED SPACECRAFT

MIDTERM REPORT

COVERING THE PERIOD 26 MAY 1969 TO 25 DECEMBER 1969

PREPARED UNDER CONTRACT JPL 952415

FOR

PROPULSION RESEARCH AND ADVANCED CONCEPTS SECTION
JET PROPULSION LABORATORY
4800 OAK GROVE DRIVE
PASADENA, CALIFORNIA, 91103

GENERAL ELECTRIC

A DESIGN STUDY FOR A MAGNETOHYDRODYNAMIC POWER SYSTEM FOR A NUCLEAR ELECTRIC PROPELLED UNMANNED SPACECRAFT

General Electric
King of Prussia Park
Philadelphia, Pennsylvania

1969

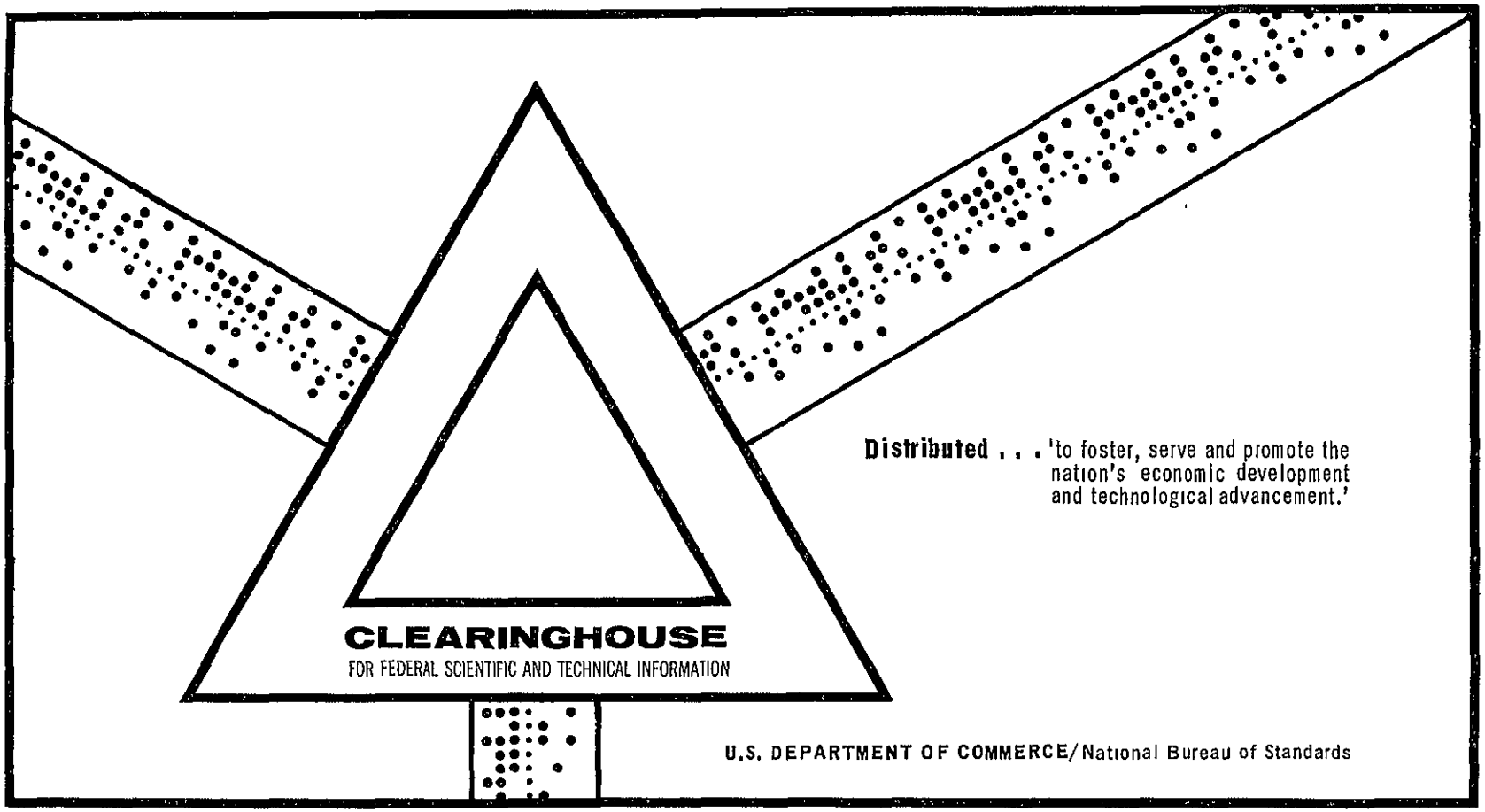

NSP NUCLEAR SYSTEMS PROGRAMS
ISOTOPE POWER SYSTEMS OPERATION

GESP-7025
DEC 1969

A DESIGN STUDY FOR A MAGNETOHYDRODYNAMIC POWER SYSTEM FOR A NUCLEAR ELECTRIC PROPELLED UNMANNED SPACECRAFT

MIDTERM REPORT

COVERING THE PERIOD 26 MAY 1969 TO 25 DECEMBER 1969

PREPARED UNDER CONTRACT JPL 952415

FOR

PROPULSION RESEARCH AND ADVANCED CONCEPTS SECTION
JET PROPULSION LABORATORY
4800 OAK GROVE DRIVE
PASADENA, CALIFORNIA, 91103

THIS WORK WAS PERFORMED FOR THE JET PROPULSION LABORATORY, CALIFORNIA INSTITUTE OF TECHNOLOGY AS SPONSORED BY THE NATIONAL AERONAUTICS AND SPACE ADMINISTRATION UNDER CONTRACT NAS7-100

ISOTOPE POWER SYSTEMS OPERATION
GENERAL ELECTRIC
SPACE DIVISION
KING OF PRUSSIA PARK
P O Box 8661 • Philadelphia, Penna 19101

2 /

This report contains information prepared by the General Electric Company under JPL subcontract. Its content is not necessarily endorsed by the Jet Propulsion Laboratory, California Institute of Technology, or the National Aeronautics and Space Space Administration.

TABLE OF CONTENTS

LIST OF ILLUSTRATIONS

LIST OF ILLUSTRATIONS (Cont)

LIST OF ILLUSTRATIONS (Cont)

LIST OF TABLES

ABSTRACT

This report discusses the progress made in the first half of a one-year design study of nuclear-electric propelled unmanned spacecraft using a magnetohydrodynamic (MHD) power system. The study guidelines and approach are defined here, and the characteristics of one launch vehicle, the thruster subsystem, and the payload and communications system are presented.

The MHD power conversion system is described and methods used to calculate MHD system parameters are discussed. This report includes a discussion of the arrangement and structural arguments used to select system configuration. The system startup technique is identified, and the detailed design and weight summary of the baseline 300 kWe system are presented.

INTRODUCTION

1. INTRODUCTION

On May 26, 1969, the General Electric Company began a design study for the magneto-hydrodynamic (MHD) power system for a nuclear-electric propelled unmanned spacecraft. This work is being performed for the Jet Propulsion Laboratory under contract number JPL 952415, and is based on MHD system technology being developed by the Jet Propulsion Laboratory. The purpose of this study is to provide size, weight and mission performance estimates for nuclear-electric propelled unmanned spacecraft using MHD power systems rated at 100 kWe to 3 MWe. This study is also intended to guide future MHD development by discovering specific requirements associated with spacecraft power system design. The spacecraft design of principal interest is one whose unconditioned power output is a nominal 300 kW(e). The weight goal for this spacecraft is 10,000 pounds including reactor, shielding, MHD conversion equipment, power distribution and conditioning equipment, thruster subsystems, and structure.

The work of this study program is divided into four principal tasks:

a. Task 1 - System Evaluation - The purpose of this task is to establish guidelines and design requirements for the program and to measure the designs generated in the program against these guidelines and requirements.

b. Task 2 - Powerplant Design - The purpose of this task is to provide the engineering analysis and design information necessary for spacecraft design layout. This will include parametric analyses to identify the influence of major plant variables on powerplant and spacecraft characteristics. This task also includes evaluation of the effects of changes in technology levels associated with the powerplant components.

c. Task 3 - Spacecraft Design - The purpose of this task is to define the arrangement, mechanical design and weight estimation for the MHD spacecraft designs.

d. Task 4 - Mission Analysis and Engineering - The purpose of this task is to perform the analysis necessary to evaluate the mission capabilities of the various spacecraft, and to perform a preliminary assessment of prelaunch, launch and flight operations, specifically with respect to aerospace nuclear safety.

In the first half of this one-year study a baseline design spacecraft and powerplant were developed. This baseline design is a 300 kWe system and assumes reasonable extension of component technology based on current test work. In the second half of the year the spacecraft and the powerplant design will be varied parametrically to evaluate the effects of changes

in output power level and operating parameters, and to evaluate the effects of improvements in the technology of key components. At the end of the year-long Phase I, a reference MHD spacecraft design will be selected. Phase I is then to be followed by a Phase II study, of about a year's length, in which this reference design will receive detailed design analysis including startup and control analysis.

The MHD spacecraft study is being performed concurrently with a design study of a thermionic reactor power system for nuclear-electric propelled unmanned spacecraft, (JPL Contract No. 952381). Wherever possible, design bases for the MHD spacecraft are being made the same as those for the thermionic spacecraft in order to provide a clear comparison of these two power systems. In particular, the MHD spacecraft baseline design is using the same payload thruster subsystem and mission profile as the Phase I thermionic reactor spacecraft.

The MHD spacecraft study is proceeding on schedule. The computer programs for MHD generator and cycle analysis have been received from JPL and converted to basic FORTRAN IV for use on the IBM 1130 computer. Preliminary startup and reactor characterization have been completed. Configuration tradeoffs were made to select the most efficient overall spacecraft configuration for development of the baseline spacecraft design. The computer programs were combined into a single MHD system program with added models to calculate key variable weights. The MHD System program was used to generate parametric data and the baseline design parametric were thereby selected. The baseline design has been drawn up and its weight calculated.

2. TECHNICAL DISCUSSION

2. TECHNICAL DISCUSSION

2.1 MHD SYSTEM REQUIREMENTS

2.1.1 BASELINE DESIGN GUIDELINES

The system requirements and design guidelines for the baseline design have been identified; they are:

a. Power Output - A nominal 300 kWe adjusted as necessary to match thruster system and other load requirements

b. Launch Vehicle - The Titan IIIC-7

c. Mission - Jupiter planetary orbiter. Starting from a 750 nm earth orbit, the spacecraft will use low, ion thrust to spiral away from earth, reach Jupiter and decelerate into Jovian orbit. The estimated time periods and power levels are as follows:

Mission Mode	Power Level (kWe)	Time (Days)
Spiral Escape from Earth	300	50
Accelerating Thrust	300	160
Coast	30	120
Decelerating Thrust	300	270
Jovian Orbit Operation	30	(one orbit, 17 days minimum)

d. MHD Cycle - One stage with two nozzles using impinging stream separation

e. Cycle Inlet Temperature - 1800°F (corresponds to reactor outlet temperature in a one-loop system)

f. MHD Loop Containment Material - Cb-1Zr

g. Radiator Type - Triform, stainless steel heat pipe

h. Permanent Shield Materials - Lithium hydride and tungsten

i. Radiation Dose Limits for Payload, Power Conditioning and Communications Equipment -

Neutron 10^{12} nvt > 1 mev

Gamma 10^{7} rad

j. Meteoroid Survival Criteria - The meteoroid model is based on the following:

1. Penetration Model

$$= 0.5\, m^{0.352} \qquad \rho_m^{1/6}\, v^{0.875}$$

2. Meteoroid Flux

$$\phi = \alpha\, m^{-\beta}$$

3. Non-Puncture Probability

$$P(0) - e^{-\phi AT}$$

4. Effective Thickness

$$t_{eff} = 0.432\ t(\text{Jupiter})$$

where

t	=	radiator armor thickness, cm
ρ_m	=	meteoroid density, gm/cm^3
m	=	meteoroid mass, gm
v	=	meteoroid velocity, km/sec
α	=	empirical coefficient
β	=	empirical exponent
$P_{(0)}$	=	non-puncture probability
ϕ	=	cumulative meteoroid flux, number particles/m^2 sec
A	=	projected vulnerable area of the spacecraft (radiator), m^2
T	=	exposure time, sec

Assumed Values

ρ_m	= 0.5g/cm^3	α	= 6.62×10^{-15}
V	= 20 km/sec	β	= 1.34
T	= 7.2×10^7 sec (20,000 hr)	$P_{(0)}$	= 0.95

2.1.2 ALTERNATE DESIGN GUIDELINES

The requirements and design guidelines for the alternate designs differ from those of the baseline design as follows:

a. Power Output - 100 kWe, 300 to 500 kWe, and 3 MWe

b. Launch Vehicle - Titan IIIC-7 and Saturn V

c. Missions

1. 100 kWe to escape on Titan IIIC-7
2. 300 to 500 kWe to low orbit on Titan IIIC-7
3. 300 to 500 kWe to escape on Saturn V
4. 3 MWe to low orbit on Saturn V

d. MHD Cycle - 1-6 stage

e. MHD Cycle Inlet Temperature - 1600 to 2200°F

f. MHD Containment Material - One advanced material

g. Radiator Type - Flatplate or triform, stainless steel or columbium heat pipe.

2.2 SPACECRAFT DESIGN GUIDELINES

2.2.1 PAYLOAD

The scientific payload and its communications system are assumed to weigh one metric ton, 2205 pounds, and to have a full power requirement of one kWe. Reference 1 has identified tentative payload details which have been adopted for the MHD spacecraft as well. The communications subsystem is assumed to require 800 of the 1000 W alloted; subsystem component characteristics are listed in Table 2-1. A payload equipment bay of approximately nine feet in diameter and at least 15 inches in height can contain the payload equipment excluding the deployable antenna, and provide adequate surface area for the payload thermal control radiator.

TABLE 2-1. COMMUNICATIONS SUBSYSTEM CHARACTERISTICS

Low Gain Antenna (Receiving)	
Diameter	6 inches
Weight (including cable)	2.5 pounds
Deployment Structure Weight	Negligible
High Gain Antenna (Transmitting)	
Diameter	9 feet
Weight (including cable)	31 pounds
Deployment Structure Weight	8 pounds
Power Input	800 watts
Power Transmitted	200 watts
Bit Rate (120 feet diameter receiving antenna)	10^4 bits/sec
Transmitter	
Weight	20 pounds
Size	6 x 6 x 20 inches

2.2.2 THRUSTER SUBSYSTEM

The thruster subsystem for the MHD spacecraft has been defined by Reference 2 and has the following general characteristics:

a. Spacecraft propulsion is provided by 31 equal size electron bombardment ion thruster engines using mercury as the propellant.

b. Six spare thrusters will be provided for a total of 37 units. Considering switching and power conditioning requirements, six spares provide one spare for each group of five operating thrusters.

c. Thrust vector control will be provided by a three axis attitude control system (two axis translation, one axis gimbal).

Guidelines for thruster subsystem design are given in Table 2-2. Thruster power supply requirements are listed in Table 2-3, and subsystem weights are given in Table 2-4.

TABLE 2-2. GUIDELINES FOR THRUSTER SUBSYSTEM DESIGN

1.	Total Conditioned Power to Thrusters	240 kW
2.	True Specific Impulse	5000 seconds
3.	Number of Thrusters	37
4.	Thruster Redundancy	20 percent
5.	Attitude Control	Electric Propulsion System
6.	Maximum Envelope Diameter	10 feet
7.	Thrust Duration	10,000 hours
8.	Technology	Estimated for 1980

2.2.3 LAUNCH VEHICLE INTERFACE

The Titan IIIC-7 launch vehicle will be used to boost the spacecraft into a 750 nm (design objective) circular earth orbit. This vehicle is similar to the Titan IIIF except that it uses a standard transtage. It is a nonmanrated vehicle and employs the stretched Stage I tanks and seven segment, 120 inch diameter solids characteristic of the Titan IIIM. The overall length of the vehicle to the payload separation plane is approximately 117 feet.

2.2.3.1 Physical Constraints on Shroud Size

The height of the 50-ton bridge crane above the launch vehicle is one identified constraint on the aerodynamic shroud (hence payload) overall length. At the Eastern Test Range (ETR) Titan vehicle in place on the Mobile Service Tower, the clearance between the bridge crane and the Titan IIIC/7 payload interface is only 75 feet while for the Titan IIIC, this clearance is 88 feet. The decrease in available clearance is due to: (1) a 5-1/2 foot increase in the length of the first stage, and (2) a 7-1/2 foot increase in launch stand height. The launch vehicle contractor suggests the possibility of using ETR launch pad 37B, which has been used for S-IB launches. There would be virtually no height limitations.

On the launch pad, a universal environmental shelter is used to provide temperature and humidity control, and RF protection. It also acts as a clean room for the transtage and payload envelope. At the present time the limit of this facility is 55 feet, which means that this is the maximum payload plus transtage length which can be accommodated. Longer lengths will require major construction revisions to the shelter.

TABLE 2-3. THRUSTER POWER SUPPLY REQUIREMENTS

Supply Number	Supply Name	Type	Output(1)	Nominal Rating					Max Rating			Control Range, A
				Volts	Amps	Watts	Reg (%)	Peak Ripple	Volts	Amps	Amps Limit(2)	
1	Screen	DC	V	3100	2.32	7200	1.0 (V)	5	3200	2.32	2.60	2.0 - 2.4
2	Accelerator	DC	F	2000	0.02	40	1.0 (V)	5@ 0.2A	2100	0.20(3)	0.21	----
3	Discharge	DC	V	35	8.3	290	1.0 (V)	2	150@ 50 mA	9@ 37V	10	7.5 - 9.0
4	Mag - Man.	DC	F	15	0.7	11	1.0 (I)	5	20	1.0	1.0	----
5	Cath Htr(4)	AC	F	10	4.0	40	5.0	5	11	4.4	4.1	----
6	Cath Keeper	DC	F	10	0.5	5	1.0 (I)	5	150@ 50 mA	1.0@ 20 V	1.0	----
7	Main Vapor.	AC	V	0.6	1.0	1	Loop	5	8(5)	2.0	2.2	0.5 - 1.5
8	Cath Vapor	AC	V	0.3	0.5	1	Loop	5	8(5)	1.0	1.1	0.2 - 0.8
9	Neut Cath Htr	AC	F	10	2.0	20	5.0	5	11	2.2	2.2	----
10	Neut Vapor.	AC	V	0.3	0.5	1	Loop	5	8 8(5)	1.0	1.1	0.2 - 0.8
11	Neut Keeper	DC	F	10	0.5	5	1.0 (I)	5	150@ 50 mA	1.0@ 20 V	1.0	----

(1) V = Variable, F = Fixed

(2) Current limit or overload trip level

(3) Current at this level for less than 5 min at low repetition rate

(4) Needed only during startup or unitl discharge reaches 3A

(5) Startup only

TABLE 2-4. THRUSTER SUBSYSTEM WEIGHTS

Component	Weight (pounds)
Thrusters (37)	585
Thrust Vector Control System	548
Miscellaneous (wiring, adapters, etc.)	100
	1,233

2.2.3.2 Flight Fairing Weight and Payload Penalty

During a "nominal" launch of the Titan IIIF vehicle, the flight fairing is normally jettisoned at 280 seconds, which is just after completion of the Stage I burn. In order to prevent freezing of the liquid metal coolant during launch, it may be desirable to retain the flight fairing as a radiation barrier until after reactor startup in earth orbit. However, this procedure imposes a severe payload weight penalty which depends on the shroud length (weight) and the terminal orbit altitude.

Figure 2-1 shows the flight fairing weight and the payload penalty as a function of shroud length, assuming shroud jettison at 280 seconds into the mission. If the shroud is retained past earth orbital insertion, then the payload weight penalty will be equal to the shroud weight. It should be noted that as the terminal orbital altitude increases, the payload penalty decreases for normal shroud ejection since a larger portion of the ΔV is added after shroud ejection. The curves are based on the data supplied by the Martin Marietta Corporation.

The effect of shroud retention on payload capability is shown in Figure 2-2. The upper lines define the Titan IIIC/7 payload capability for a 28.5 degree orbital inclination mission with shroud jettison occurring at 280 seconds into the mission. The lower curves show the effect of retaining the shroud through achievement of final Earth orbit.

Under nominal conditions, and with a 35-foot shroud, the vehicle can deliver 30,000 pounds into a 630 nm circular orbit. Employing longer shrouds, with jettison at 280 seconds, reduces the payload capability (initial mass in Earth orbit) as shown in Table 2-5.

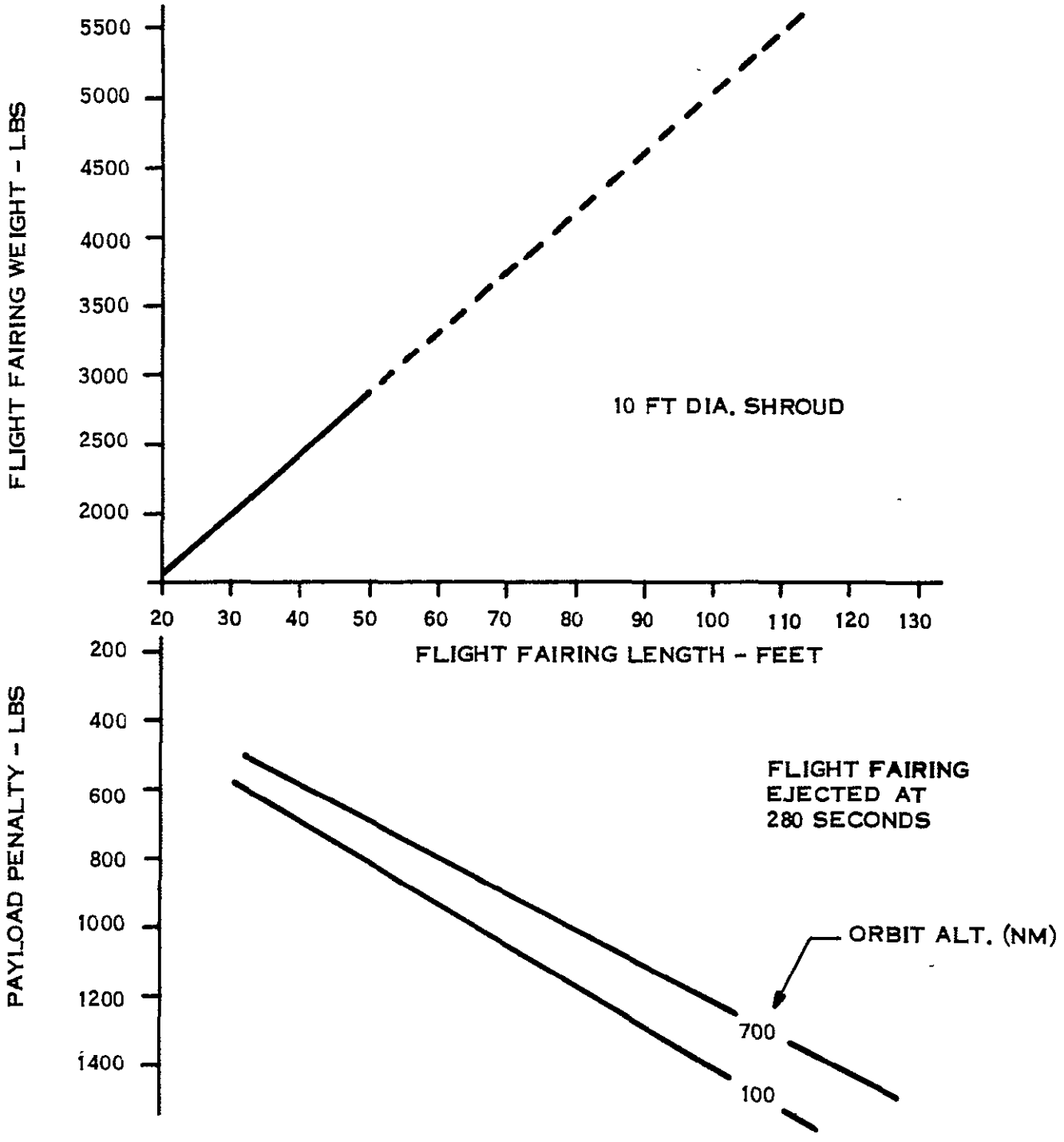

Flight 2-1. Flight Fairing Weight and Payload Penalty (Titan IIC/7)

21

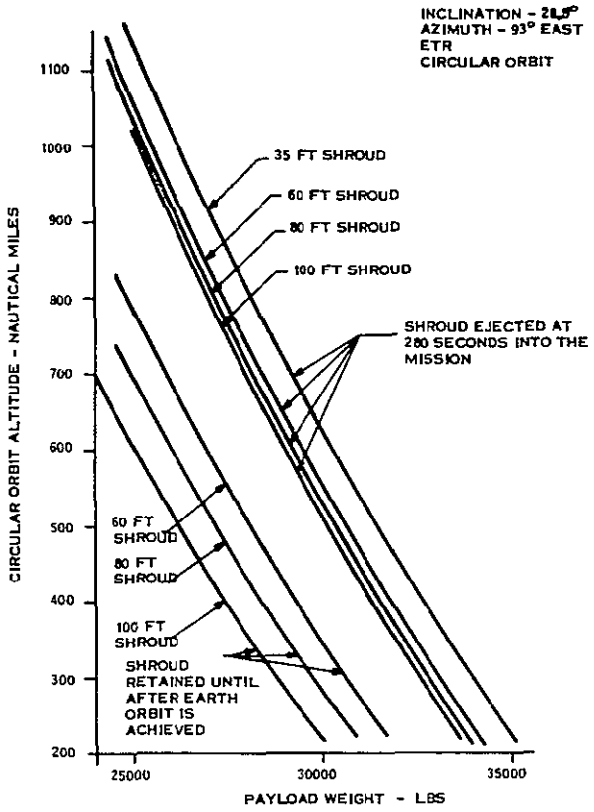

Figure 2-2. Effect of Shroud Retention on Payload Capability (Titan IIC/7)

TABLE 2-5. MAXIMUM PAYLOAD CAPABILITY WITH SHROUD EJECTION AT 280 SECONDS

Shroud Length (feet)	Shroud Penalty (pounds)	Maximum Payload Weight (pounds)
60	808	29,191
80	1021	28,978
100	1234	28,765

Alternatively, injecting 30,000 pounds of payload into circular orbit will decrease the maximum possible orbit altitude as shown in Table 2-6.

If the shroud is jettisoned after achieving Earth orbit (630 nm), the payload capability will be reduced as shown in Table 2-7.

TABLE 2-6. MAXIMUM EARTH ORBITAL ALTITUDE FOR A 30,000 POUND PAYLOAD, WITH SHROUD JETTISON AT 280 SECONDS

Shroud Length (feet)	Maximum Orbit Altitude (nm)
60	555
80	530
100	512

TABLE 2-7. MAXIMUM PAYLOAD CAPABILITY AT 630 NM WITH SHROUD EJECTION AFTER ACHIEVING EARTH ORBIT

Shroud Length (feet)	Shroud Penalty (pounds)	Maximum Payload Weight (pounds)
60	3300	26,700
80	4200	25,800
100	5000	25,000

2.3 MHD POWER SYSTEM OPERATION AND ANALYSIS

2.3.1 TWO-COMPONENT LIQUID METAL MHD POWER SYSTEM

2.3.1.1 Power System Fluid Flow

Figure 2-3 illustrates the flow arrangement by which a two component liquid metal MHD power system can generate useful amounts of electrical energy with no moving parts except the fluids themselves. As the illustration shows, lithium is heated in a heat source and injected into expansion nozzles with liquid cesium. Upon mixing in the nozzles, heat transfer from the lithium causes the cesium to boil. The lithium liquid does not boil but is dispersed in the stream by the boiling of the cesium. As the lithium breaks up into smaller and smaller drops its surface-to-volume ratio increases, enhancing heat transfer to the cesium vapor. The high specific heat of lithium along with a relatively high lithium mass flow to cesium mass flow ratio enables the cesium boiling and expansion in the nozzles to take place at almost isothermal conditions.

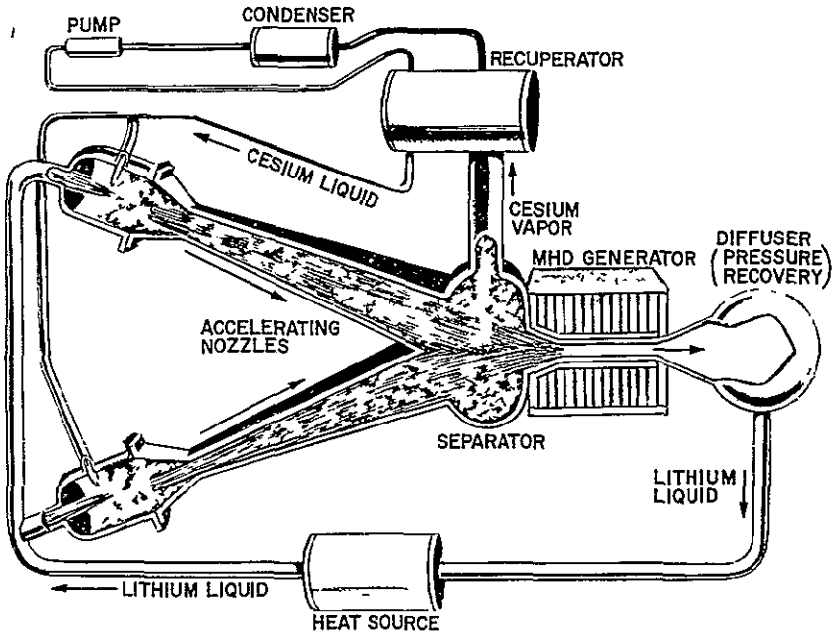

Figure 2-3. Lithium - Cesium MHD Cycle

The expansion of the cesium vapor as it travels down the nozzles accelerates the entrained lithium liquid droplets to high velocities. At the convergence of the two nozzles the impingement of the two streams requires each to undergo a change in direction. The resulting lateral acceleration imposed on the flow stream causes its components to separate into strata with the lithium collecting in the center of the combined stream and the cesium vapor moving out to the sides of the stream. The combined lithium streams enter a diffuser where the stream pressure is raised threefold to dissolve any remaining cesium bubbles and the lithium stream then passes through the MHD generator duct where much of the stream's kinetic energy is converted to electrical energy (see Paragraph 2.3.1.2 - Energy Conversion, following). At the MHD generator exit, the lithium stream passes into a diffuser where most of its remaining kinetic energy is converted to pressure head in order to pump the lithium through the heat source and back around to the nozzle entrance with more heat.

The cesium vapor, separated from the lithium streams at the nozzle exists, is passed out through a recuperator to a condenser. The condensed cesium is pumped electromagnetically back through the recuperator to the nozzle entrances where it can be vaporized again.

A simpler method of stream separation is used in the single nozzle MHD test system shown in Figures 2-4 and 2-5. This system, which is currently being used for development testing by Dr. D. G. Elliott at Jet Propulsion Laboratory, operates at about room temperature with NaK alloy in place of lithium and compressed nitrogen gas expanding to accelerate the liquid phase. In this arrangement, the vapor and liquid streams are separated by impingement on an inclined plate, see Figure 2-5. The single nozzle system, although simpler to construct, is less desirable because of the skin friction losses the liquid stream suffers in passing across the separator plate. In the dual nozzle system the opposing streams, moving at equal speeds, provide the flow diversion thus eliminating this friction loss and improving system overall efficiency from about six and one-half percent to almost eight percent. Although the dual nozzle system will require flow balancing, its improved efficiency makes it the more attractive design.

2.3.1.2 The Variable-Velocity MHD Induction Generator

The induction MHD generator is attractive because it allows:

a. A. C. power generation with a better capability of transformation and conditioning.

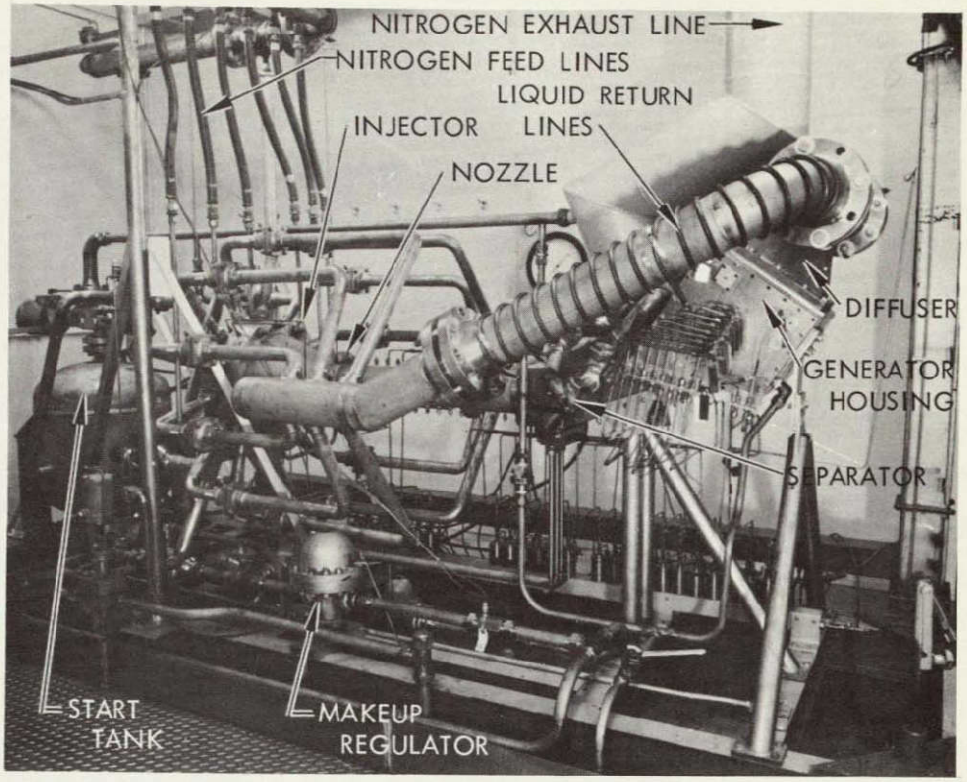

Figure 2-4. NaK/N_2 MHD Test System

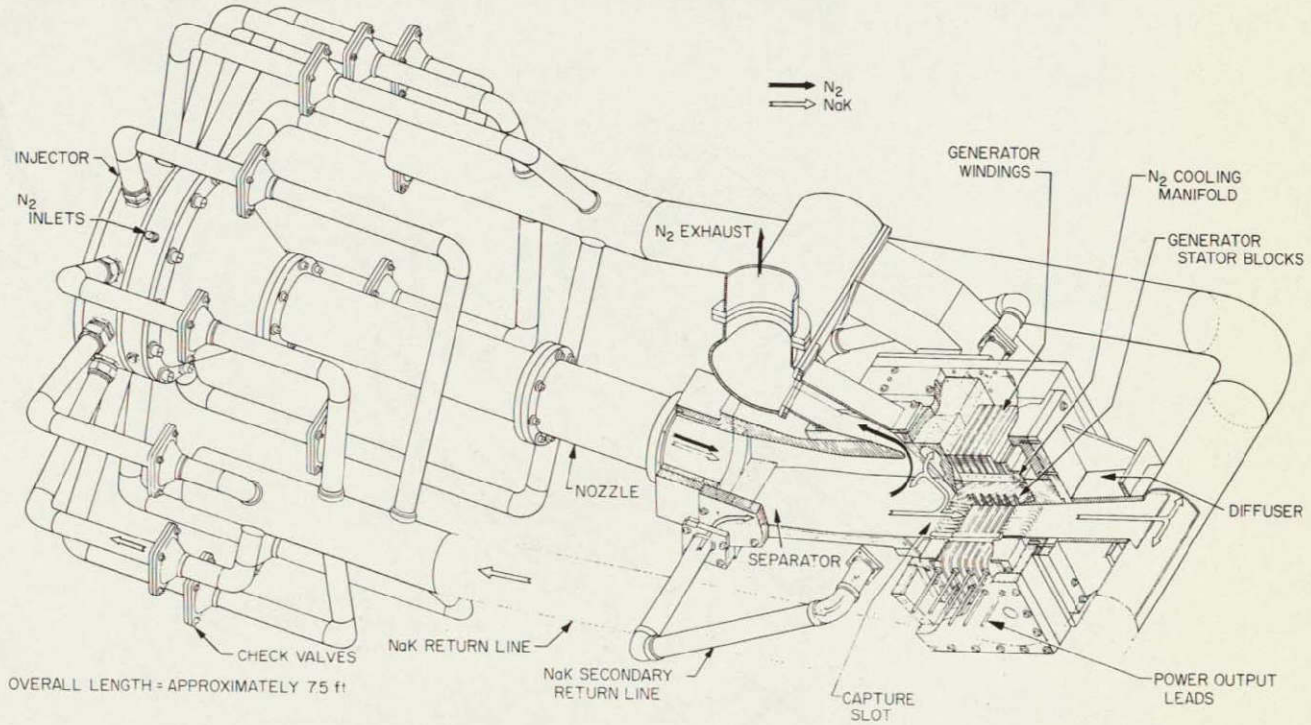

Figure 2-5. NaK/N_2 MHD Test System

b. Electrodeless operation in the presence of high temperature corrosive working fluids

c. Control over the output voltage by appropriate choice of winding turns.

One form of such a generator is essentially a flat development of the more familiar rotating, solid conduction generator, and consists of a pair of iron stators separated by conducting side plates to form a duct through which a liquid metal conductor is forced to flow (Figure 2-6). The stator blocks are slotted to carry windings which produce a travelling wave magnetic field in the direction of fluid flow. The liquid metal travels faster than the field, causing currents to be induced in the direction shown. The fluid retardation caused by the currents must be accommodated by progressive expansion of the channel. Completion of the current loop, and the resulting magnetic field induces an AC voltage in the windings with, typically, a resultant power output.

The simple, flat development briefly described above has the very serious drawback that the original, continuously rotating magnetic field has been interrupted between the cut, and separated, ends. There is an ohmic power loss in the windings when producing the travelling

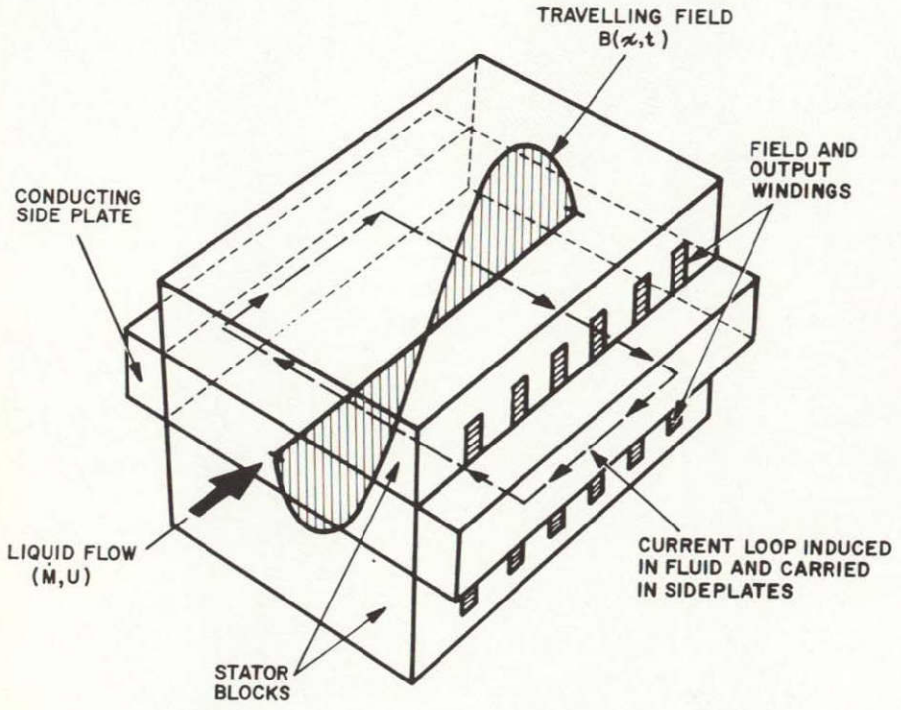

Figure 2-6. Variable Velocity MHD Induction Generator

wave, and for a fixed wave amplitude, the winding dissipation increases proportionately with the number of wavelengths imposed on the generator. The use of a single wavelength generator minimizes the winding loss, but maximizes the end losses due to the abrupt initiation and termination of the magnetic field. However, analysis (Reference 3) has shown that, the proper inclusion of a compensating pole in slots at each end of the generator together with the design constraint along the generator that cBU_s = constant (where c is the duct width, B the magnetic field rms value at x, and U_s is the velocity of the zero crossing of the magnetic field at x), will re-produce exactly the familiar rotating induction machine voltage.

$$s = \frac{U - U_s}{U_s}$$

is the slip between the fluid and wave velocities, and U is the fluid velocity at x, with θ the value of ωt when the zero field crossing is at x.

The fact that cBU_s = constant allows considerable design flexibility. However, it has been found (Reference 3), for simpler conditions, more beneficial to hold c constant rather than B constant, so that the design constraint becomes BU_s = constant. In the face of frictional effects, it turns out (the same as the rotating machine efficienty) that the maximum local internal generator efficiency is

$$\eta_x = \frac{1 - \text{sec}}{1 + s}$$

with the optimal slip being $s = (1 + H_a^2)$ where

$$\frac{\sigma b B^2}{\rho c U_f}$$

is the Hartmann number, with

σ = The fluid conductivity,

b = the channel height

ρ = the liquid density and

C_f = the skin friction coefficient.

This optimal s then sets the relation $U_s = U_s$ (U) to produce the maximum electric output, P_o, through the resulting maximum η_x. A first choice of inlet magnetic field B_1 then establishes B = B(U) since BU_s = constant, with the final value of B_1 resulting from optimization of the generator efficiency, η_g. This latter optimization results from the fact that, although P_o increases indefinitely with field, the winding losses start increasing rapidly at a certain field value.

With the generator width c fixed as indicated above, the duct height distribution is determined directly from the mass continuity requirement, while the duct length results from electrically (and frictionally) retarding the fluid at constant pressure and optimal slip to the desired exit velocity. This exit velocity is such that, with satisfactory diffusion, sufficient pressure is available to return the liquid to the energy source without pumping.

2.3.2 MHD SYSTEM ANALYSIS

As described in Reference 4, the analysis of the MHD Power System is based on the analytical approach developed by Dr. D. G. Elliott and others at Jet Propulsion Laboratory. During the first half of this study, the computer programs developed at JPL were converted from CAL to basic FORTRAN IV, combined into a single MHD System program and modified to calculate other parameters of interest to the spacecraft designer.

2.3.2.1 MHD Generator Analysis

2.3.2.1.1 Generator Analysis Assumption - The assumptions employed in analyzing the generator are as follows:

1. The slip and the field are varied to maintain rotating-machine internal electrical efficiency $\eta_0 = (1 + s)^{-1}$ at each point, where s is the slip $(U - U_S)/U_S$ between the fluid velocity U and the magnetic field wave velocity U_S.

2. The pressure is constant from inlet to exit of the traveling-wave region.

3. The losses in the generator consist only of (1) fluid ohmic losses from the fluid current necessary for the required retarding force, (2) shunt end currents and eddy currents in the compensating poles, (3) wall friction, (4) winding loss, and (5) the increase in those losses due to the limitations on field amplitude and slot area from iron saturation. There are no losses from: (1) variation of magnetic

field and current density across the height of the channel, (2) boundary layer currents, (3) increased friction due to MHD effects, (4) ohmic losses in the copper side-electrodes, (5) departure of the magnetic field from sinusoidal wave-form, and (6) eddy currents in the walls.

Assumption 1 requires the generator to operate with the product of field and wave velocity, BU_s, held constant from the inlet to the exit of the traveling-wave region. With this constraint, the current in the fluid is the same at every point as it would be in a constant-velocity generator and the efficiency of power generation in the fluid is $(1 + s)^{-1}$ at every point. The possible disadvantage of a constant-BU_s design is that the field in the upstream part of the generator must be lower than would be optimum at the same fluid velocity in a constant velocity generator, because of the reduced upstream field required to maintain BU_s = constant while not saturating the iron at the downstream end. The possibility of higher over-all efficiency with a departure from the constant-BU_s case assumed here has not been explored.

Assumption 2 constant pressure in the traveling-wave region, is adopted for simplicity. There is a possibility of higher cycle efficiency with a pressure rise in the generator, because of lower velocity and friction loss and because of reduced pressure recovery requirement in the downstream diffuser, but pressure-rise operation has not been explored.

Assumption 3 is the key one. Five loss mechanisms are adopted as being the only significant ones. All other losses, six of which are enumerated, are assumed to be negligible. The arguments for neglecting the six losses enumerated will be reviewed briefly.

1. Field and Current Density Variation Across the Channel Height - The efficiency of a constant-velocity generator using the exact field equations (both x and y variations accounted for) was calculated by Pierson (Reference 5) and the results compared with the "slit-channel case" ($B_x = 0$ and B_y = const) assumed here. Pierson found negligible efficiency decrease using the exact equations when $\pi b/L << 1$, where b is the channel height and L is the wavelength. In a typical lithium generator, the value of $\pi b/L$ is 0.2, and there was no more than 0.1 percent efficiency loss at this value in Pierson's analysis.

2. Boundary-Layer Currents - Boundary-layer currents of high density flow in the near-stationary part of the fluid near the wall. If the velocity profile is a fully-developed 1/7-power profile extending to the center of the channel, then the internal electrical efficiency cannot exceed 0.78 (Reference 6). But there is evidence (Reference 7) that the velocity profile is highly flattened in the generator, in which case the

boundary-layer shunt currents may cause only negligible losses. There is also the possibility of designing the generator with a wall that is retracted from the boundary of the flow, giving a "free-jet" effect which could further flatten the velocity profile.

3. Friction Increase - Friction increase due to MHD effects has been studied and found to exist, but only by about 10 percent at ratios of Reynolds number to Hartmann number of interest in this application. To account for this and other possible effects, a factor of increase in friction of 1.3 is employed in the program.

4. Side-electrode Losses - The ohmic losses in the canned copper side-electrodes can be reduced as much as desired by giving them a large cross section, but at some point they begin to interfere with the coils. Thus, this loss reduces to an optimization problem between coil loss and axial-conductor loss. Preliminary design studies have indicated that the side-electrodes can have sufficient area for negligible loss if skin effect is not too great, but further studies are required.

5. Non-sinusoidal Waveform - The loss due to the finite number and width of the winding slots was analyzed in Reference 8. An efficiency loss of 3 percentage points was calculated for a generator employing 24 slots. The calculations were pessimistic in that they did not consider the smoothing out of the waveform that occurs in practice due to fringing. Hence, a 15 degree spacing between slots can be expected to give negligible loss compared with a continuous current sheet. In the power system energy balance, account is taken of this inefficiency by deducting 3 percent from the generator output.

6. Wall Currents - Operation without wall currents requires achievement of a wall which is both thermally and electrically insulating. A slotted, cesium-purged refractory-metal wall with ceramic between it and the stator, and a vacuum interface with the stator, is one concept proposed; alternatives include bare ceramic walls and coated ceramic walls.

The net effect of excluding the six losses enumerated is to make the calculations optimistic by an amount which might only be a few percentage points but could be much larger. Pending further experiments, the present analysis will be considered to predict the generator performance ultimately achievable after careful development.

2.3.2.1.2 Generator Program Analysis - Input data for the lithium mass flow, lithium density, the inlet and outlet velocities and the chosen constant duct width immediately allow calculation of the duct entry and exit heights, using the mass continuity equation. This is followed by calculation of the inlet Reynolds member (based on the inlet hydraulic diameter) and allows determination of an average, corrected turbulent skin friction coefficient to account for the

changing duct height, side wall contributions and MHD effects on the velocity profile. A calculation of the fluid input kinetic power to the travelling wave region is followed by a determination of the assumed constant travelling wave iron gap (based on duct inert height and wall thickness input data), compensating pole iron gaps and copper coil conductivity based on a chosen operating temperature.

With a chosen value of inlet magnetic field B_1 the inlet Hartmann number can be calculated. This leads to a value of optimum inlet slip s_1 for maximum local efficiency and determination of the inlet wave velocity V_{s_1}, thus fixing the required constant value of $BU_s = B_1 U_{s_1}$. The exit slip s_2 can be calculated iteratively and will then allow determination of the generator frequency duct length and the gross power output. Calculation of the gap flux voltage induced per coil turn completes the set of quantities dependent on the chosen value of inlet magnetic field.

The next section of the program deals eith the coordinates and the value of slip s for each copper winding slot. The desired number of slots is an input parameter, but the actual number may be slightly less due to geometric constraints at the end of the duct. With s known at a slot, then calculations can be made for lithium velocity, duct height, wave velocity, magnetic field, and currents through the fluid and the windings.

The next calculations are related to the slot dimensions, the sector length over which each slot is assumed to be effective, and the electrical aspects of the windings. The slots in the travelling wave region are treated separately from the end slots which carry the current for the compensating poles. Advantage is also taken of the less restrictive iron and copper losses by appropriate shaping and positioning of the end slots in the last section of calculations.

The electrical performance of each winding slot is calculated by using the previously computed appropriate slip value. Results are obtained for the various contributions to the power balance (including friction and ohmic effects), together with the induced voltage per turn and the reactive power which dictates the corrective capacitance requirement.

2.3.2.1.3 Generator Variable Sensitivity - Before the generator and cycle programs were combined, the generator program was run with parameter variation to determine variable sensitivity. The rounded input data for the base case used for this determination are:

M1 FLOW RATE Kg/sec	U1 INLET VEL m/sec	U2 EXIT VEL m/sec	C CHANNEL WIDTH m	I8(1) UPSTREAM COMP POLE EDDY CURRENT AMP. TURNS Amp	I8(2) DWNSTRM COMP POLE EDDY CURRENT AMP TURNS Amp	L(1) UPSTR COMP POLE LENGTH cm	L(2) DWNSTRM COMP POLE LENGTH cm	H1 INLET CHANNEL HEIGHT cm	H2 EXIT CHANNEL HEIGHT cm	I(1) WALL THICKNESS mm	I(6) INLET FIELD (RMS) Tesla
90	116	61	0 23	175	140	5	5	1.7	1 7	2 5	0 46

The principal results for this case were:

$P_{induc} = 3.337.9$ kW,

$P_{coil} = 8.04$ kW,

$P_{net} = 329.8$ kW,

$P_{reac} = 1248.5$ kW, and

net efficiency $\eta_{net} = 0.730$.

The program was then run to determine the effect on the base case values of varying one input quantity at a time. This quantity X (=U1, M1, etc. in turn) was varied over a small range about the base case value, X_{ref}, to determine a sensitivity factor

$$\frac{dQ}{dX} \times \frac{X_{ref}}{Q_{ref}}$$

where Q was an output quantity such as P_{net}, η_{net}, P_{reac} and P_{coil}

The sensitivity actors for P_{net} in Figure 2-7 show that U1, M1 and U2 are by far the most influential on net power, while, from Figure 2-8, M1, U2 and C have the most effect on net efficiency. These sensitivity factors can be useful for interpolation when a particular operating point is required.

It should be noted that the variation of X about X_{ref} probably produces values of η_{net} less than the optimum value presumed associated with the reference base case by adjustment of B_1.

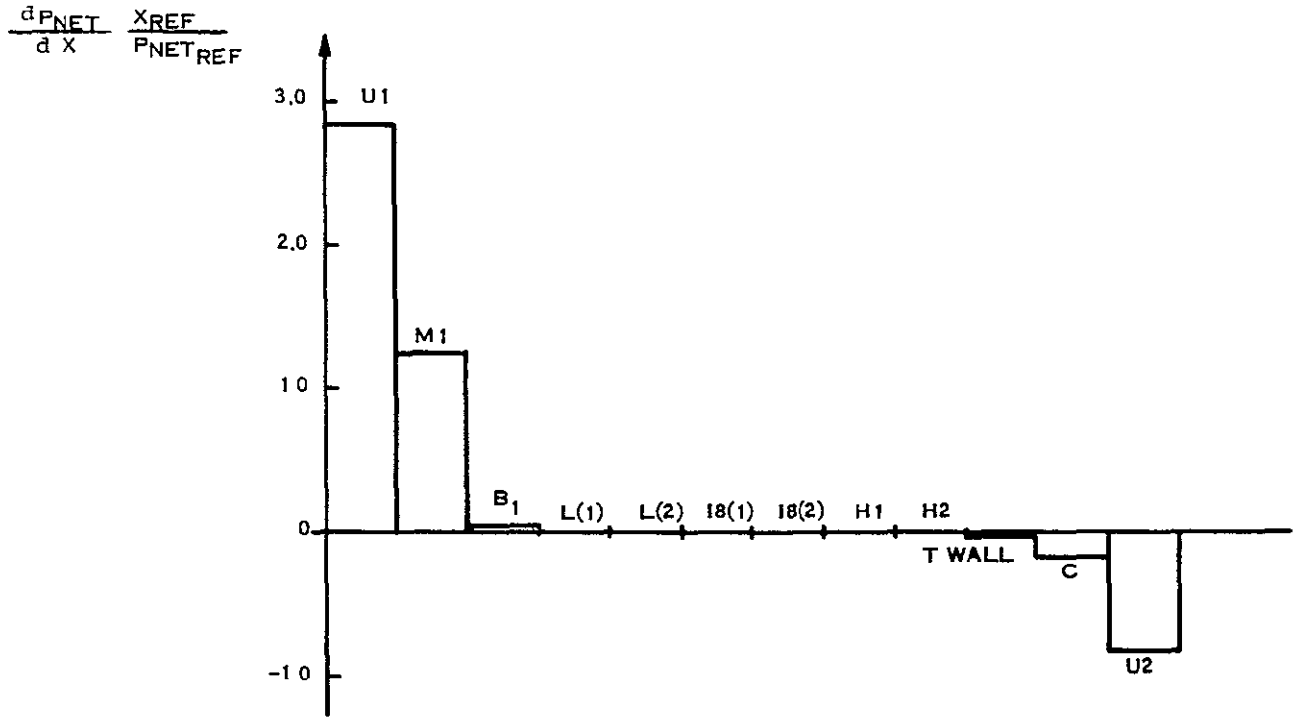

Figure 2-7. Sensitivity Factors for Net Power

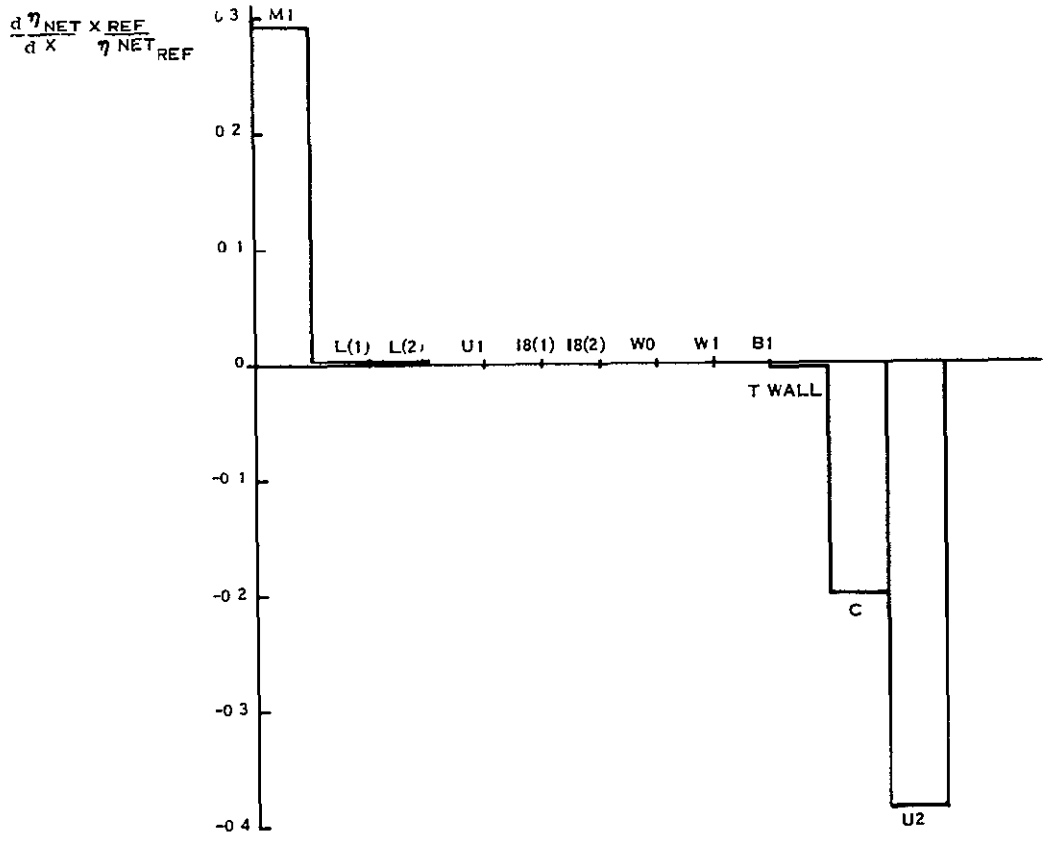

Figure 2-8. Sensitivity Factors for Net Efficiency

It was initially rather surprising that the wall thickness, t_{wall}, had almost no effect on P_{net} and η_{net}. Since wall thickness has a direct bearing on lithium duct heat transfer to the stator block, and incorporation of methods to suppress wall currents, its effects were investigated further. As seen in Figure 2-9 the principal effects of increasing t_{wall} from one to ten millimeters are to double the reactive power and produce a roughly proportionate increase in copper coil dissipation. These cause significant penalties in capacitor weight and low temperature radiator area.

The decrease in P_{net} and η_{net} are relatively modest, being, of course, directly coupled to P_{coil}.

2.3.2.2 MHD Cycle Analysis

A cesium-lithium MHD power system with an impinging-jet separator is shown schematically in Figure 2-10.

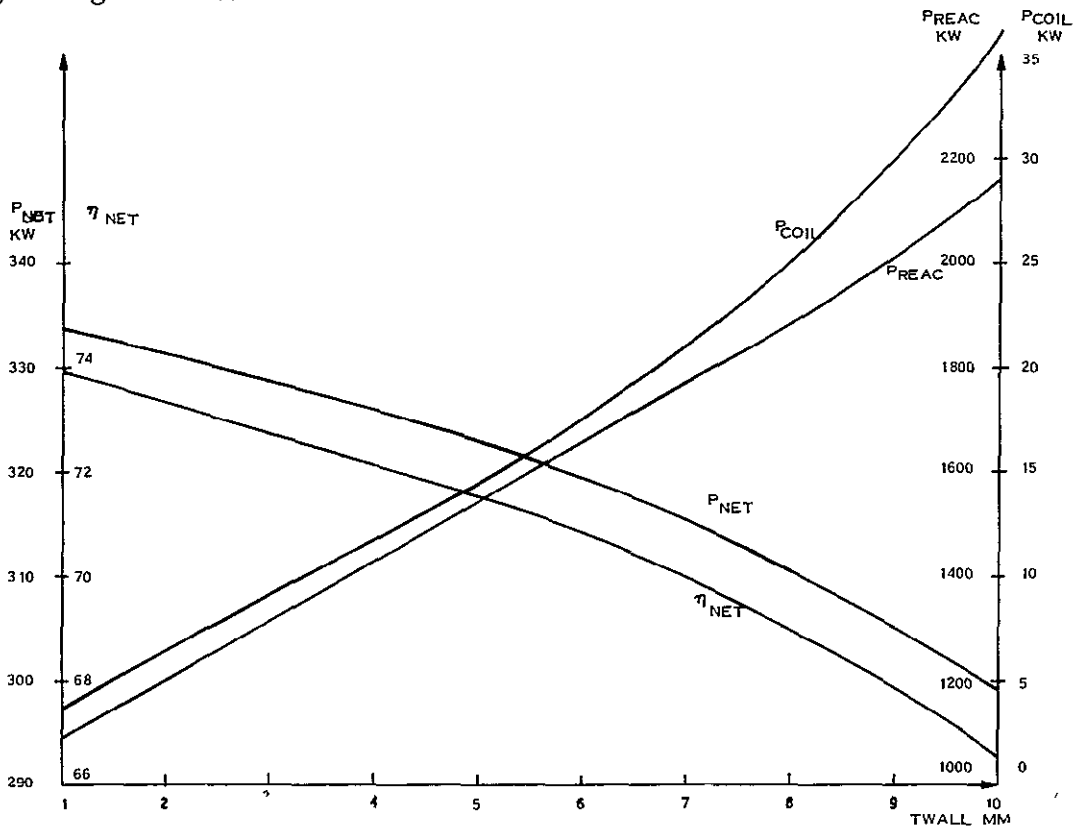

Figure 2-9. Effects of Varying T_{wall} From One to Ten Millimeters.

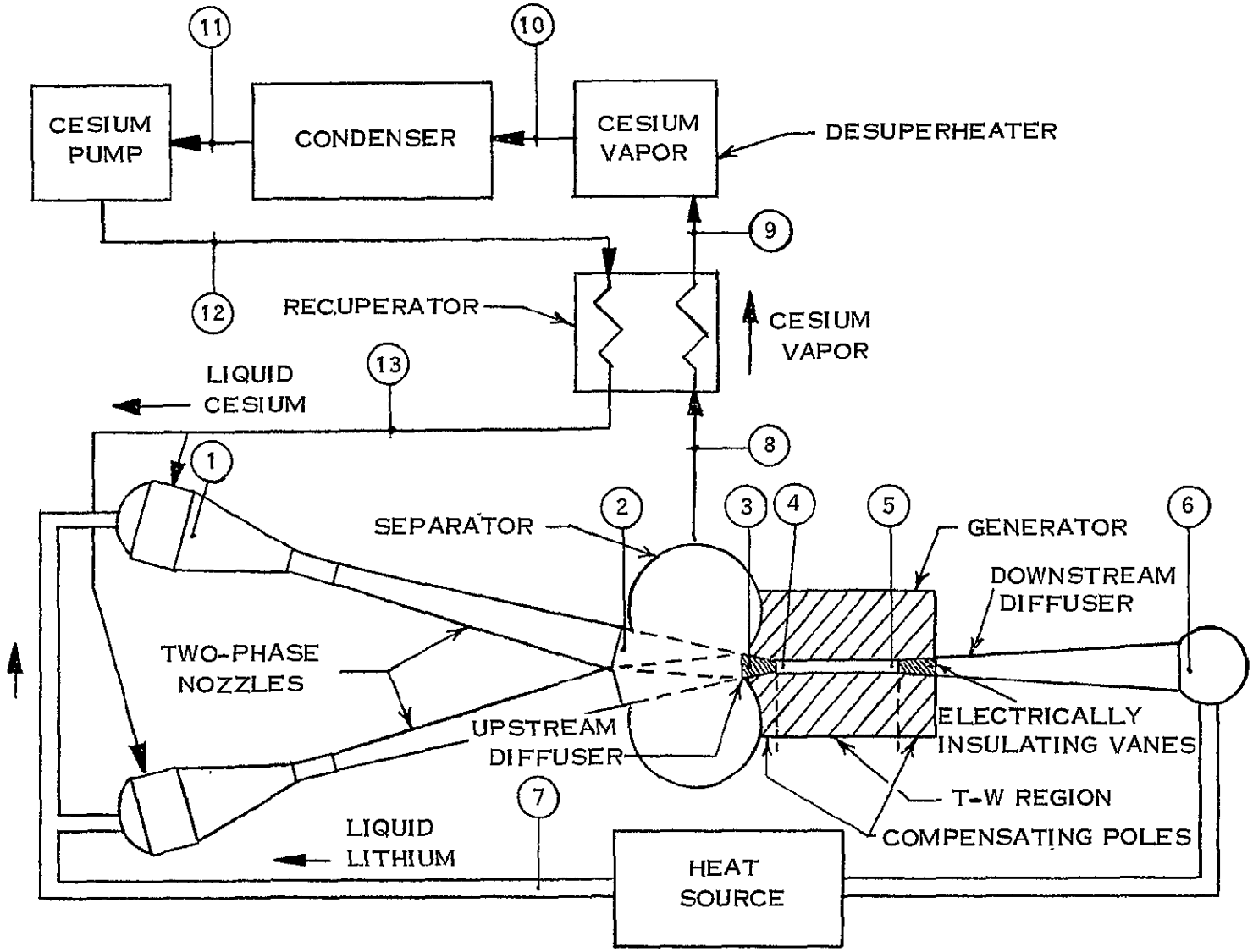

Figure 2-10. Cesium-Lithium MHD Power System with an Impinging-Jet Separator

Liquid lithium and liquid cesium enter a pair of two-phase nozzles and mix at low velocity and high pressure. Heat transfer from the lithium to the cesium vaparizes the cesium. The two-phase mixture expands to low pressure at the nozzle exits, accelerating the liquid lithium to high velocity.

The two-phase jets from the nozzles impinge on each other at an angle, and the inward momentum drives the lithium drops together to form a coalesced two-phase jet of substantially reduced vapor void fraction.

The jet enters the upstream diffuser where the pressure of the cesium-lithium mixture is increased until the cesium is dissolved in the lithium. The liquid stream then enters the generator.

In the generator the stream of lithium (containing a few percent of cesium) is decelerated by electromagnetic retarding force. The force is adjusted to leave sufficient velocity for the lithium to flow through the downstream diffuser to the pressure required at the inlet of the heat source. The lithium is reheated in the heat source and returned to the nozzles.

The cesium vapor leaving the impinging-jet separator flows to a recuperator where the cesium is desuperheated, and where the lithium vapor is condensed, to the extent permitted by the heat sink capacity of the liquid cesium leaving the cesium pump.

The remaining cesium superheat is removed in a desuperheater. The saturated cesium vapor is condensed in the condenser, and the condensate is pumped to the liquid side of the recuperator by the cesium pump. After being heated in the recuperator the cesium is returned to the nozzles.

2.3.2.2.1 Cycle-Analysis Assumptions - The assumptions employed in analyzing the cycle are as follows:

1. The concentration of cesium dissolved in the lithium is the equilibrium value for the prevailing temperature and pressure at each point in the system.
2. The nozzle exit conditions are those given by the two-phase, two-component nozzle program of Reference 9.

3. Any liquid lithium entrained with the cesium vapor leaving the separator is separated out and returned to the impinging jets or elsewhere in the lithium loop before the cesium vapor enters the recuperator.

4. A compensated AC generator is used, and the compensating poles coincide with the upstream diffuser and with the vaned portion of the downstream diffuser.

5. The losses in the upstream diffuser consist of: (1) friction on the walls and insulating vanes (used for electrical loss reduction) corresponding to 1.3 times flat-plate skin friction and (2) electrical losses due to the AC compensating field of the generator.

6. The efficiency of the downstream diffuser without vane-friction or electrical losses is 0.85.

7. The additional losses in the downstream diffuser are: (1) friction on the insulating vanes corresponding to 1.3 times flat-plate skin friction and (2) electrical losses due to the AC compensating field of the generator.

8. There are no electrical losses in the walls of the upstream or downstream diffusers, or in the generator channel, due to the AC generator.

9. The pressure in the generator is constant from inlet to exit.

10. The temperature difference between the cesium vapor entering the recuperator and the liquid cesium leaving the recuperator is $50^{\circ}K$.

11. The cesium pump is driven by electric power from the MHD generator, and all power dissipated is transferred to the cesium being pumped.

12. The heat rejected by the cycle is the heat required to cool and condense the cesium vapor from the recuperator exit condition to the saturated liquid state at the condenser exit pressure, including the heat required to cool the small amount of lithium mixed with the cesium.

13. The pressure drop across the nozzle injection orifices is 5 psi, and the injection velocity is 30 ft/sec.

Assumption 1, equilibrium cesium dissolving, implies transfers of several percent of cesium into and out of liquid solution in fractions of a millisecond. No information is available on cesium-lithium solution rate, and the validity of this assumption is not known.

If equilibrium concentration did not occur, the nozzle performance would be improved but the efficiency of the diffusers would be decreased. Calculations assuming non-dissolving cesium in a system with a surface-impingement separator showed that the two effects would be about equal and the cycle efficiency with non-dissolving cesium would be about the same as with equilibrium dissolving. With an impinging-jet separator however, the upstream diffuser losses with non-dissolving cesium would probably be unacceptable without some added mechanical removal of cesium vapor from the jet before entering the capture slot. Thus, the rate of cesium dissolving affects the design of the system, but it probably does not greatly affect overall cycle efficiency.

Assumption 2, the validity of nozzle exit conditions from Reference 9, is well verified by experiments with water-nitrogen mixtures. Uncertainties in cesium-lithium properties, including the dissolving rate, could change the nozzle exit velocity a few percent from the values given by the nozzle program.

An additional requirement for Assumption 2 to be valid is that the separator duct must have about 40 percent more area than the nozzle exit to allow radial expansion of the cesium jet as its velocity equalizes with that of the slower liquid jet.

Assumption 3 requires removal from the cesium exhaust of a liquid flow equal to 0.5 to 1.0 percent of the nozzle liquid flow rate, in the case of the best present surface-impingement separators. Several times as much lithium migh have to be removed with an impinging-jet separator where a curved target is not available for collecting the smaller drops. A satisfactory method of returning the collected liquid to the lithium stream with an impinging-jet separator has not yet been demonstrated; reinjection into the impinging jets causes increased dispersion. The penalty of liquid remaining with the cesium might be preferable, since the recuperator liquid-side sink capacity would increase almost as much as the added heat load, falling short only by the $50^{\circ}K$ minimum ΔT (Assumption 10). A velocity reduction factor is one of the inputs to the cycle analysis program, and with this factor the user can supply any penalty believed attributable to returning the lithium from the cesium exhaust. Supplying a factor of 1.0

implies that either there is no liquid loss or that all lithium is returned and remixed at full velocity with the impinging jets.

Assumption 4, the utilization of an AC induction generator, represents the best choice both for generator efficiency and ease of power conditioning. A DC generator might be thought to offer better efficiency, but the voltage across the channel in a DC generator causes shunt end currents extending farther upstream and downstream than can be suppressed by insulating vanes of reasonable length. An AC generator, on the other hand, operates at ground potential throughout the fluid, except locally in the compensating poles where relatively short insulating vanes can suppress the losses.

The second part of Assumption 4, overlapping of the compensating poles and diffusers, represents a logical combining of processes within a single region to reduce friction losses.

Assumption 5 restricts the upstream diffuser losses to 1.3 x flat-plate friction, plus electrical losses from the compensating flux. The friction losses observed in the limited tests conducted to date with vaned upstream diffusers could be correlated by applying a factor of between 2 and 3 to flat-plate friction, or they could be correlated by an impact loss in which all of the flow intercepted by the $\sim$ 0.02-inch thick vanes (5 percent of the total flow) was stagnated. Another source of loss, and perhaps the most likely, is two-phase slip or shock effects at the diffuser entrance. Whatever the loss source, Assumption 5 postulates a reduction in upstream diffuser loss from an observed 2.5 x, to an assumed 1.3 x, flat-plate friction.

The electrical losses included in Assumption 5 are calculated by a procedure which agreed roughly with some limited data on a small-scale generator, but accurate experiments on the fluid electrical losses in the compensating poles are lacking.

Assumption 6, an efficiency of 0.85 for the downstream diffuser before adding vanes and electrical losses, is well verified by liquid diffuser experiments (Reference 10).

Assumption 7 for the losses added to the downstream diffuser by the vanes and electrical effects has the same uncertainties as Assumption 5, but to a lesser extent because only liquid flow is involved.

Assumption 8, no electrical losses in the walls, is contingent on development of a thermally insulating, electrically insulating wall which exposes only metal to the lithium stream.

Assumption 9, constant pressure in the generator, is adopted for simplicity.

Assumption 10, 50°K minimum recuperator ΔT, should allow adequate heat flux at the hot end. The ΔT at the cold end is typically 200 to 300°K because of the lithium condensation on the vapor side.

Assumption 11 specifies a cesium pump design utilizing power from the AC generator either directly or after conditioning, with the electrical components at the cesium temperature. If lower electrical temperatures were employed there would be a requirement for radiation of some power at the lower temperature, but the cesium sink capacity would increase by an equal amount and there would be no change in cycle heat rejection.

Assumption 12 limits the heat rejection considered to that from the cesium vapor (and the lithium vapor mixed with it) only. Additional heat losses from cooling of the generator and other components and from stray losses are not considered in the heat balance or cycle efficiency.

Assumption 13, 5 psi injection pressure drop, is a value at which stable nozzle operation has been demonstrated. The assumed inlet velocity of 30 ft/sec required only in calculating the nozzle inlet area (the effect on exit velocity is negligible), corresponds to 2.0 psi dynamic pressure of the lithium, and should be attainable with 5 psi injector pressure drop.

2.3.2.2.2 Cycle Program Analysis - The MHD cycle program employs twenty independent variables, including η_g (efficiency of the travelling wave region of the generator), f (generator frequency) and ϕ_c (compensating pole flux) which are supplied by the generator program. These generator supplied terms are used in the cycle program's energy balance to calculate the raw generator output (η_g) and the compensating pole losses (f and ϕ_c). Reference 4 contains a detailed description of the cycle program analysis.

2.2.2.3 Additional Analyses

In addition to the parameters calculated in the generator and cycle programs as originally written (described in the reference 4), there is a need to calculate other parameters which are of significant concern to the spacecraft designer. Modifications to the computer programs were made to calculate these values on the bases described below.

2.3.2.3.1 MHD Stator Iron Weight - In the present generator analysis the stator slot height, D_o, is calculated but the total iron height is not. This total height can be identified as D_s and set equal to the sum of $D_o + D^*$ where D^* is the height of unslotted iron. D^* can be calculated explicitly since the net magnetic flux in this region is equal to the compensating pole flux (Reference 5). The iron cross-sectional area can therefore be calculated by setting

$$B_S \geqq \frac{\sqrt{2}\,\phi_c}{A} \tag{1}$$

where

B_S = saturation flux for iron, T

ϕ_c = compensating pole flux, W_b

A = iron area, m^2

B_S is an imput to the program; ϕ is calculated by the program; and A is the product of c (channel/stator width, a program input) and D^*, the dimension sought. Therefore, total stator iron height is

$$D_S = D_o + D^*$$

$$D_S = D_o + \frac{\sqrt{2}\,\phi_c}{c\,B_S} \tag{2}$$

The length of the stator block is

$$L_{Tot} = L_{TW} + L_{IN} + L_{OUT} \tag{3}$$

where

L_{TOT} = total length

L_{TW} = length of travelling wave section

L_{IN} = length of upstream compensating pole section

L_{OUT} = length of downstream compensating pole section

From the arguments developed in Reference 4 L_{IN} and L_{OUT} can be estimated quite closely as

$$L_{IN} = w\,t_1 - (x_1 - \frac{w\,2_1}{2}) + w\,2_0 + w\,6_1 \tag{4}$$

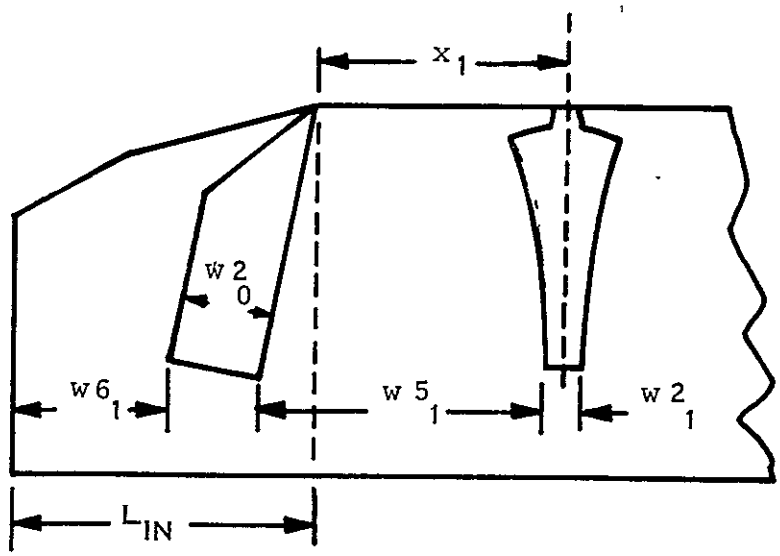

By the same technique

$$L_{OUT} = w\,5_2 - (L - x_{K-1} - \frac{w\,2_{K-1}}{2}) + w\,2_K + w\,6_2 \tag{5}$$

The total stator volume then can be estimated by multiplying

$$V_{St} = 2 \times D_S \times c \times L_{TOT} \tag{6}$$

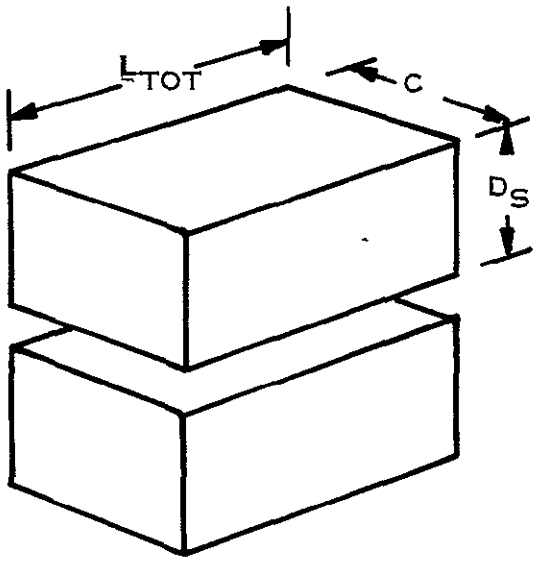

The generator program already calculates the slot area and the slot volume can be calculated by

$$V_{slot} = c \sum_{n=1}^{n=N-1} [w1_n D_n - w2_n (D_n - D_o)]/3 \tag{7}$$

for the travelling wave region and

$$V_{end\ slot} = c\ 4\ w_A\ D_o$$

for all four compensating pole slots (assuming a pair at each end of the generator) where

$$w_A = 1/2\ (w2_p + w2_N)$$

$$w^2_o = L_1, \text{ if } L_1 < D_o$$

$$w^2_o = D_o, \text{ if } L_1 > D_o$$

$$w^2_N = L_2, \text{ if } L_2 < D_o$$

and

L_1 = length of upstream compensating pole

L_2 = length of downstream compensating pole

The iron weight can then be calculated

$$\text{Weight } F_e = \rho F_e \left[V_{st} - V_{slot} - V_{end\ slot} \right]$$

2.2.2.3.2 MHD Generator Winding Weight - In the calculation of MHD generator performance, winding losses are calculated by the use of a winding loss factor, α, which is defined:

$$\alpha = \frac{\text{actual winding loss (including iron loss)}}{\text{solid fill DC loss of slot portion of coils}}$$

The numerical value of α has been assumed to be 3 as a typical value. Since the copper coil windings of the MHD generator are estimated to weigh more than 1000 pounds (Reference 3), and explicit relationship between copper weight and actual winding loss is needed in order that a tradeoff between copper weight and auxiliary cooling system weight can be made. In Reference 11 the coil loss factor, α, was broken down as follows:

a. slot filling factor: 0.8

b. ac/dc resistance ratio: 1.4

c. external conductor dc resistance is equal to slot dc resistance

d. The iron core loss is assumed to be negligible.

Thus,

$$\text{Reff} = \alpha R_i = 1.4 \frac{R_i}{0.8} + 1.0 \frac{R_i}{0.8} = 3 R_i$$

where R_i is the solid-fill slot dc resistance.

If the total current is I then the total winding loss is calculated as $\alpha I^2 R_i$. With α broken down it is possible to determine the external conductor resistance penalty when reducing the conductor weight as follows. Let resistance of external copper by γ times the above-assumed value so that $\gamma = 1$ corresponds to $\alpha = 3$ with the values assumed under items a and b above retained unchanged. Then:

$$\alpha = 1.75 + \frac{\gamma}{0.8}$$

which is plotted in Figure 2-11.

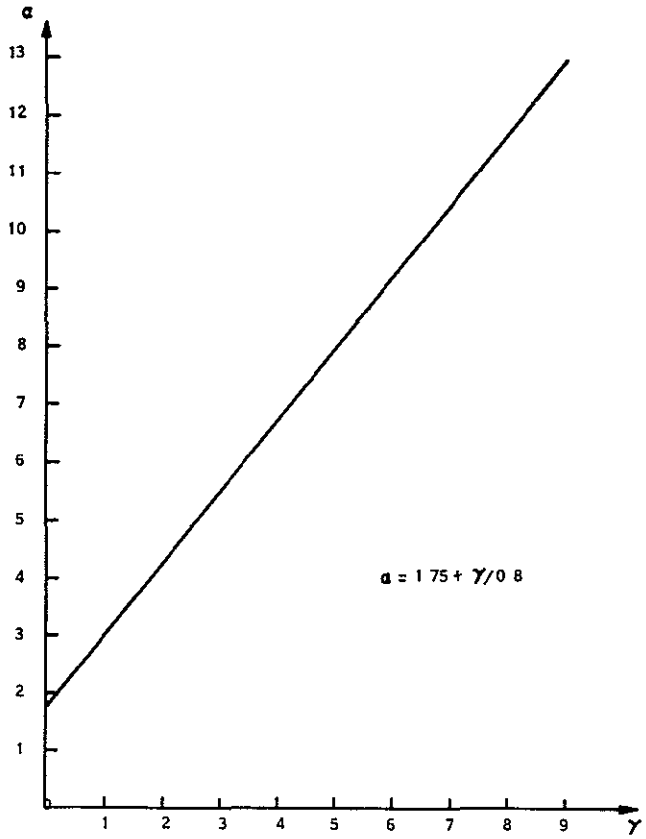

Figure 2-11. Relation Between Coil Loss Factor, α, and External Conductor Resistance Factor, γ

46

We now wish to express copper weight as a function of γ. Since resistance

$$R = \rho \frac{\ell}{A}$$

where

ρ is copper resistivity

ℓ is conductor length

A is conductor area

It will be necessary to determine ℓ and A for the slot conductor and for the slot conductor and for the external conductor. For the slot conductor the volume of the copper and hence the weight can be obtaine explicity in the program. The cross sectional area of a particular shot is given by

$$A = \left[W1 \cdot D - W2 \cdot (D-D_o)\right] /3 \qquad (8)$$

where

$$D_o = 0.75\, D_{k-1}$$

and

D_{k-1} is the sharp point depth of the last inboard slot (see Figure 2-12)

and since the length is c, the volume for the travelling wave region slots is given by

$$Vol_{cu} = \frac{.8c}{3} \sum_{n=1}^{n=N-1} W1_n \cdot D_n - W2_n (D_n - D_o) \qquad (9)$$

The copper volume for the compensating pole slots is calculated

$$V_{\text{end Cu}} = 0.8\, c \quad 4W_A \quad D_o$$

where

$$w_a = \frac{w2_o + w2_N}{2}$$

and

$$w2_o = L_1, \text{ if } L_1 < D_o$$

$$w2_o = D_o, \text{ if } L_1 < D_o$$

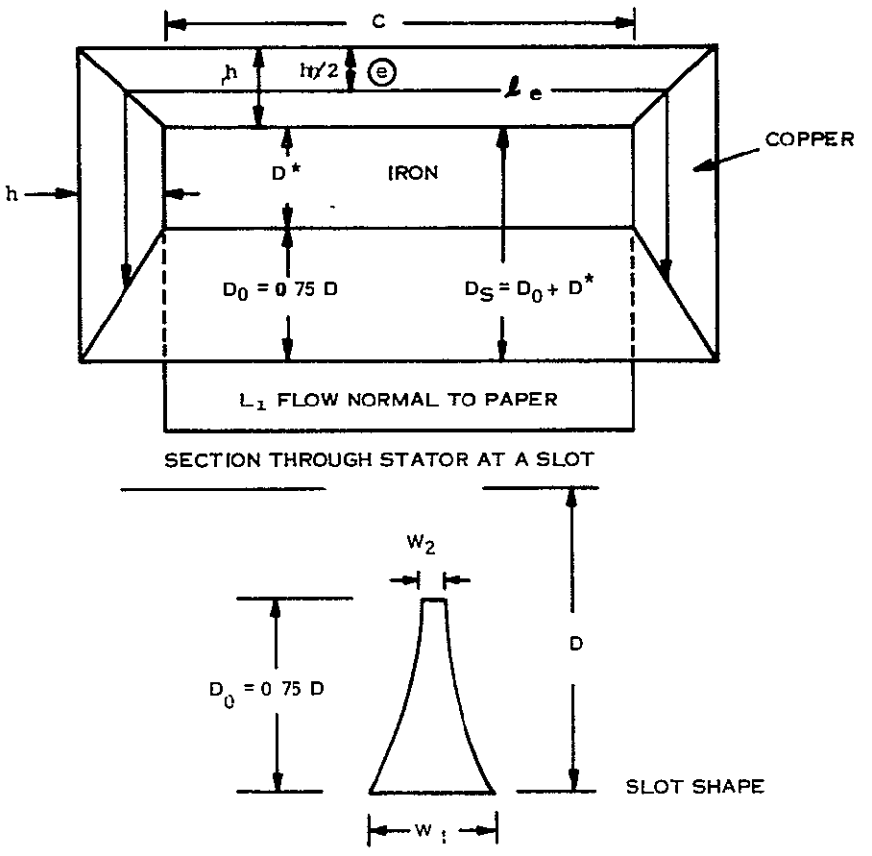

Figure 2-12. MHD Stator Winding Geometry

$$w2_N = L_1, \text{ if } L_2 < D_o$$

$$w2_N = D_o, \text{ if } L_2 < D_o$$

and

L_1 = length of upstream compensating pole

L_2 = length of downstream compensating pole

In both cases the sum is multiplied by 0.8 as this is the packing fraction of copper in a slot

We can express the volume of the copper external to a particular slot as

$$Vol_{cu} = W_e \ell_e h \tag{10}$$

where

W_e is the external width of the copper winding

ℓ_e is the external length of the copper winding

h is the height of the copper winding

By inspection of the generator program results, it appears reasonable to set

$$W_e = 5/3 \; W1 \tag{11}$$

(a better approach might be to set W_e equal to the corresponding sector width, but this requires more inspection). This will reasonably fill the outside face of the stator block with copper.

We can estimate the length of the copper as

$$\ell_e = c + 2\ (1/2\ D_o + D^* + h/2 + h/2$$

$$\ell_e = c + D_s + D^* + 2h \tag{12}$$

The first term $(1/2\ D_o)$ in the bracket is considered a reasonable estimate in the cross-section shape-changing region on leaving the slot.

We can now write the cross-sectional area as

$$A_e = 5/3\ \ W1 \cdot h$$

and since

$$\frac{\ell_e}{A_e} = \gamma \frac{\ell_s}{A_s} = \gamma\ \frac{c}{A_s}$$

We can now write

$$\gamma \frac{c}{A_s} = \frac{c + D_s + D^* + 2h}{5/3\ W1\ h}$$

solving for h yields

$$h = \frac{A_s\ [c + D_s + D^*]}{5/3\ W1 \cdot \gamma c - 2A_s} \tag{13}$$

Putting (11), (12) and (13) into (10) yields

$$Vol_{cu_n} = (c+D_s+D^*+2h_n)\ (5/3\ W1_n) \left[\frac{A_{s_n}\ (c+D_s+D^*)}{5/3\ W1_n\ \gamma c - 2A_{s_n}}\right] \tag{14}$$

This equation yields the volume of the copper external to the nth slot.

The total volume of copper is then

$$Vol_{cu} = Vol_{cu_o} + Vol_{cu_N} + \sum_{n=o}^{n=N} Vol_{cu_n} \qquad (14)$$

The first two terms are necessary to include all compensating pole slot copper for the case of two compensating pole slots at each end.

These equations will be used in programming the weight calculations into the generator code.

2.3.2.3.3 Coil Coolant Requirement - In the calculation of coil dissipation losses, an average coil temperature, T_C, is specified and used to evaluate the resistance which is temperature dependent. This temperature must be maintained by cooling the coil external to the generator. The coolant supply temperature i.e., auxiliary-radiator outlet temperature, T_{out}, required will be a function of T_C, coil dissipation and coil dimensions. The following technique has been used to evaluate T_{out}. The result is then used to size the auxiliary radiator.

Half of a coil is shown schematically in Figure 2-13 which also indicates some of the nomenclature. Volume 1 is inside the stator, Volumes 2 and 3 are outside with Volume 3 being in contact with the fin structure of Figure 2-14. Coil dissipation, P_{coil}, is divided on a volumetric basis. For example, the dissipation in 1 is

$$Q1 = \frac{P_{coil}\ Vol_1}{2\ (Vol_1 + Vol_2 + Vol_3)}$$

where

Vol_1 is the volume of 1.

Assuming uniform dissipation and a one dimensional temperature distribution in Volumes 1 and 2 the temperature drops are given by

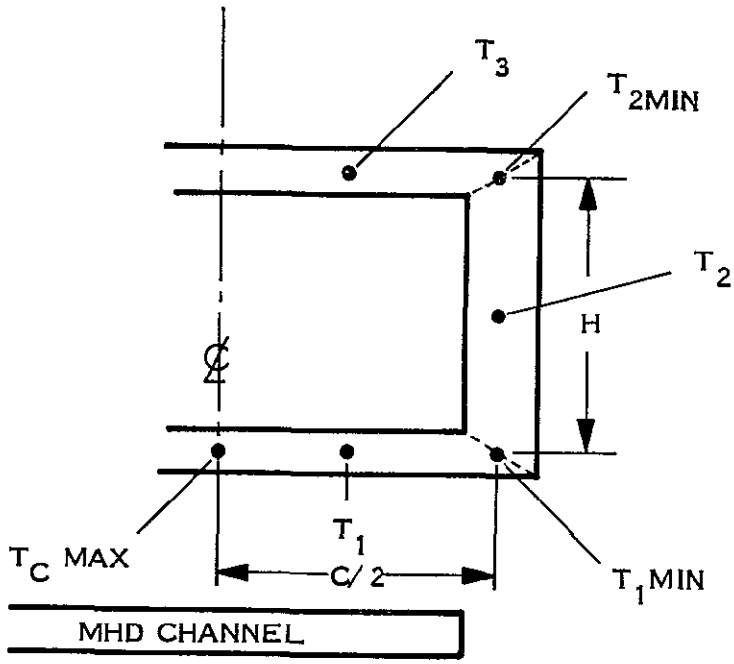

Figure 2-13. Coil Geometry and Temperatures

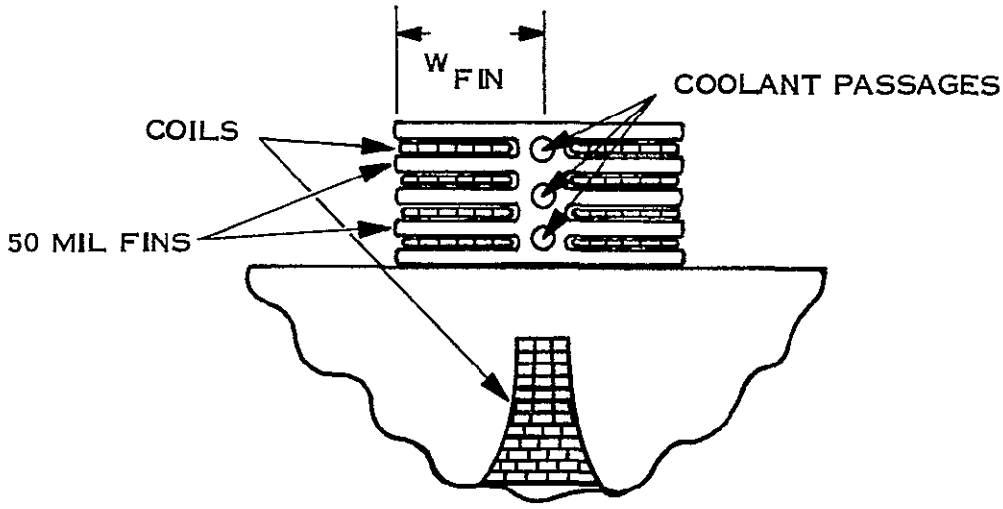

Figure 2-14. Coil Cooling Fins

$$\Delta T_1 = T_{c\,max} - T_{1\,min} = \frac{Q1}{Vol_1}\left[\frac{1}{2} \quad (c/2)^2\right] \tag{1}$$

$$\Delta T_2 = T_{1\,min} - T_{2\,min} = \frac{Q2}{Vol_2}\left[\frac{1}{2}\ h^2\right] + \frac{Q\,1\,h}{A_2\,K} \tag{2}$$

A_2 is the cross sectional area of volume 2. Copper thermal conductivity K is taken as constant with the value 9.4 watts/in. ^{o}C which is correct at 200^{o}C. The variation in K between 100^{o}C and 400^{o}C is from 9.7 to 8.95 watts in. ^{o}C. Temperature gradients in volume 3 are neglected since this volume is being cooled.

Since the coil average temperature, T_C, is used to calculate resistance from

$$R = \rho\, \ell/A,$$

T_C is calculated as a weighted average as follows:

$$T_C\left(\frac{C}{2A_1} + \frac{h}{A_2} + \frac{C}{2A_3}\right) = T_1\,\frac{C}{2A_1} + T_2\,\frac{h}{A_2} + T_3\,\frac{C}{2A_3} \tag{3}$$

where

$$T_1 = T_{c\,max} - \frac{1}{2}\,\Delta T_1$$

$$T_2 = T_{c\,max} - \Delta T_1 - \frac{1}{2}\,\Delta T_2$$

$$T_3 = T_{2\,min} = T_{c\,max} - \Delta T_1 - \Delta T_2$$

With ΔT_1 and ΔT_2 given by (1) and (2) and T_c specified, equation (3) can be solved for $T_{c\,max}$. The temperature drops are thus determined with the dissipation and geometry while the temperature level is determined by average coil temperature.

Fluid temperature T_{out} is given by

$$T_{out} = T_3 - \Delta T_{ins} - \Delta T_{fin}$$

ΔT_{ins} = gradient across insulation

ΔT_{fin} = gradient along length of fin

$$\Delta T_{ins} = \frac{P_{coil/24} \ \Delta L}{K_{ins} \quad A_{fin}}$$

$$\Delta T_{fin} = \frac{P_{coil/12}}{Vol_{fin}} \left(\frac{1}{2} W_{fin}^{2}\right)$$

The insulation gradient is based on heat transfer to 24 fin surfaces (Figure 2-14) of area $\Delta_{fin} = W_{fin} \times C$. The fin width W_{fin} is just 1/2 W_e = 5/6 W1. ΔL, the insulation thickness is assumed to be 6 mils and K_{ins} = 0.109 Btu/hr Ft^2 ^oF.

The fin gradient assumes one dimensional temperature and uniform heat addition over the surface.

In the computer program, this procedure is followed for only the last coil. Since this coil has the largest dissipation per unit volume, the ΔT_1, ΔT_2, and T_C values which are calculated are maximum. The T_{out} value is thus smaller than required for all coils except the last one and the resultant radiator area is conservative.

2.3.2.3.4 Conditions at Recuperator Exit - The energy exchange, Q_ℓ, in the recuperator is determined by an energy balance for the liquid cesium between points 12 and 13 of Figure 2-10. With given recuperator inlet conditions (at point 8), a given pressure drop and a calculated Q_ℓ, the conditions at the recuperator exit (point 9) can be determined.

This is done by an iterative process assuming for a starting point that all the lithium is consensed at point 9 i.e., $\beta_9^{(0)} = 0$. An energy balance between points 8 and 9 then yields a first value for $T_9^{(1)}$ which is larger than the correct value. With $T_9^{(1)}$ and P_9 an equilibrium value of β, $\beta_9^{(1)}$, is calculated. A new heat balance produces $T_9^{(2)} < T_9^{(1)}$, since not all of the lithium is condensed. This $T_9^{(2)}$ corresponds to an equilibium value $\beta_9^{(2)} > \beta_9^{(1)}$. The iteration is continued until T_9 doesn't change significantly.

2.3.2.3.5 Secondary Radiators - The secondary radiator is modeled using test data obtained with a NaK 78 radiator operating with T_{inlet} between 300 and 700°F, ΔT = 50 to 200°F and Q <10 kW. The geometry is shown in Figure 2-15.

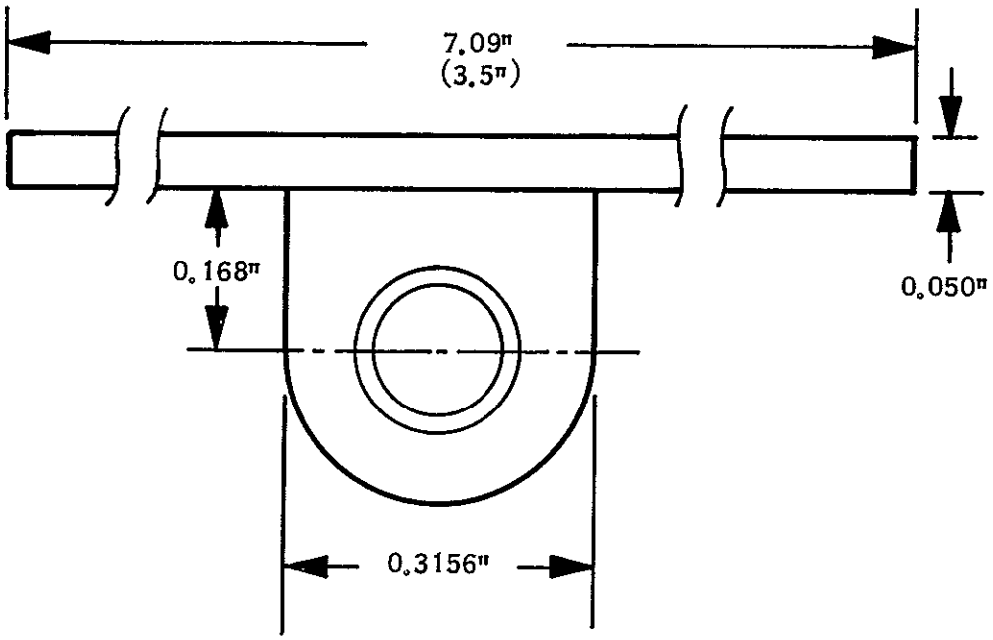

Figure 2-15. Auxiliary Radiator Geometry

An effective temperature is defined

$$T_{eff}^4 = T_s^4 + \frac{4\,T_s^3\,(T_{in} - T_{out})}{\ell n\left[\frac{(T_{in} - T_s)\,(T_{out} + T_s)}{(T_{in} + T_s)\,(T_{out} - T_s)}\right] + 2\left[\tan^{-1}\left(\frac{T_{out}}{T_s}\right) - \tan^{-1}\left(\frac{T_{in}}{T_s}\right)\right]}$$

T_{eff} = effective temperature ^{o}R

T_{s} = sink temperature = $460^{o}R$

T_{in} = radiator inlet temperature ^{o}R

T_{out} = radiator outlet temperature ^{o}R

A curve fit for fin efficiency is

$$\eta = 0.983 + 8.5 \times 10^{-5} T_{eff} - 2.56 \times 10^{-7} T_{eff}^{2}$$

The required radiator area for coil cooling is thus

$$A_{c} = \frac{P_{coil}}{\eta \epsilon \sigma (T_{eff}^{4} - T_{s}^{4})}$$

ϵ = emissivity of radiator = 0.85

Radiator weight for coil cooling is given by

$$WT\ (lb) = 0.968\ A_{c}\ (ft^{2})$$

For the coil radiator, a negligible radiator ΔT is assumed i.e., $T_{in} \approx T_{out} = T_{3}$. Cooling of the stator, valve motors and pump may be done at an $800^{o}F$ temperature level. The radiator model above is used with $T_{eff} = 800^{o}F$. The tube spacing is cut from 7.09 to 3.5 inch to raise η to 0.9 and a weight multiplier of 1.55 is applied to reflect a material change to Cu/SS for the higher temperature. The higher temperature secondary radiator weight is then given by

$$WT\ (lb) = 1.91A\ (ft^{2})$$

2.3.2.3.6 Capacitor Cooling - The large reactive power characteristic of the MHD generator means that dissipative losses in the excitation capacitors can be an appreciable heat rejection load. No off-the-shelf capacitor suitable for the MHD spacecraft has been

identified but conversation with manufacturers indicate that a mica/silicone oil type would offer the high temperature and high radiation resistance desired with relatively low dissipative losses. The size of a typical unit of 5 μfd capacitance was estimated to be 6 by 4 by 3-inch with dissipation loss perhaps as high as 1 percent if the capacitor operating temperature were $\sim 400^{\circ}$F. At lower temperatures the dissipative loss would be reduced. In order to provide adequate heat rejection by the capacitors, they were arranged broadside to space, over a panel area of 60 square feet. This area was chosen as being sufficient to reject 1 percent dissipative loss at 400°F, 0.61 percent at 300°F, or 0.35 percent at 200°F (see Figure 2-16). It is believed that the dissipation versus temperature curve for the capacitor will have a more shallow slope and that the 60 square foot panel area will assure stable operation at some temperature less than or equal to 400°F.

2.3.2.4 Selection of Baseline Design Parameters

The baseline design was selected by comparing results of several calculations made with the combined cycle and generator programs. An initial set of calculations was made with the parameters in Table 2-8.

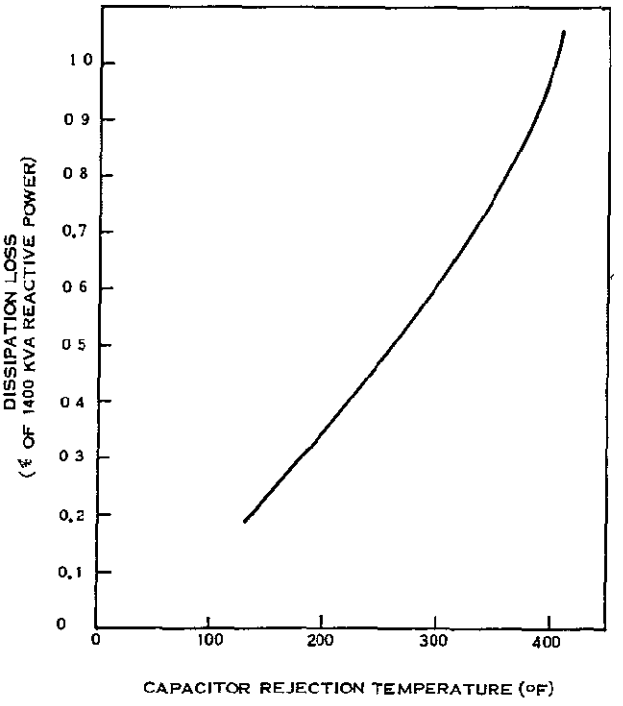

Figure 2-16. Capacitor Heat Rejection

TABLE 2-8. PARAMETERS VARIED IN DESIGN SELECTION
(RUNS 1 TO 11)

Run No.	Coil Ratio γ	Coil Temperature T_c (^oC)	Nozzle Exit/ Throat Area Ratio AR	Separator to Condenser ΔP $(N/M)^2$	Inlet Field B_o Wb/M^2
1 (Base)	1.0	200	3.0	2×10^4	0.48
2	1.0	200	3.0	1.5×10^4	0.48
3	1.0	200	3.0	2.5×10^4	0.48
4	1.0	250	3.0	2.0×10^4	0.48
5	1.0	300	3.0	2.0×10^4	0.48
6	1.0	200	2.75	2.0×10^4	0.48
7	1.0	200	3.25	2.0×10^4	0.48
8	0.8	200	3.0	2.0×10^4	0.48
9	1.2	200	3.0	2.0×10^4	0.48
10	1.0	200	3.0	2.0×10^4	0.46
11	1.0	200	3.0	2.0×10^4	0.50

Parameters held fixed were:

Wall thickness = 4 mm (fluid to stator gap)

Power output = 275 KW

Pump efficiency = 20%

Nozzle Case = 4 (Li/C_s mass flow ratio = 14:1)

Nozzle Exit W/H = 3.5

THETA = 0.262 Radians (impinging half-angle)

Velocity Factor = 1

Gas vol. flow rate ÷ Liq vol. flow rate = 3

Diffuser L/W = 0.2

Vane L/W = 0.2

No. of upstream vanes 18

No. of downstream vanes 28

Heat source $\Delta P = 7 \times 10^4$ N/M^2

Recuperator $\Delta P = 4 \times 10^3$ N/M^2

Condensor $\Delta P = 2 \times 10^4$ N/M^2

Results are presented in Table 2-9 and Figures 2-17, 2-18, and 2-19. Design parameters are sought which will minimize weight and radiator area. Preliminary radiator area is reflected in the weight calculation only on a pounds per square foot basis; there really should be a multiplier applied to reflect the increase in flight fairing and structure weight which accompanies increases in primary radiator area and length.

There is an incentive to limit the secondary radiator area. The spacecraft configuration provides about 200 square feet of surface on the outside of the MHD equipment bay. About 60 square feet of this surface is needed for mounting the excitation capacitors and the rest is available for secondary radiator area with no increase in spacecraft length. Thus, if the secondary radiator area is less than 140 square feet, the weight of one pound per square feet is realistic since the radiator panels can be hung on the MHD bay. However, if the area exceeds 140 square feet a structural extension of the MHD bay will be required, with attendant increases in structure and flight fairing weight.

The weight trends indicated in Figure 2-17 indicate choice of low Δp, B_o and γ but high area ratio and coil temperature. Figure 2-18 also indicates choice of low γ and B_o and high coil temperature and area ratio. The secondary radiator area is insensitive to variation in separator to condenser pressure drop. Figure 2-19 shows that to minimize primary radiator area, it is important to have low Δp and area ratio and that primary radiator area is much less sensitive to the other variables. Consequently, an area ratio of 3.25 and a Δp of 1.5×10^4 N/M^2 were selected and further investigation was made with the γ, B_o and T_c parameters. The parameter variations are given in Table 2-10 and the results are listed in Table 2-11. Inspection of the results shows that Run No. 19 gives a near minimum total weight and primary radiator area with a secondary radiator area of 129 square feet a bit less than the desired limit of $\sim$ 140 square feet. The parameters of Run No. 19 were therefor chosen for the baseline design.

TABLE 2-9. PARAMETRIC WEIGHTS AND AREAS (RUNS 1 TO 11)

Run No.	Weight - Pounds					Areas - ft^2	
	Generator	Capacitors	Primary Radiator	Secondary * Radiator	Total	Primary Radiator	Secondary** Radiator
1	618	1197	2818	653	5286	1395	665
2	618	1197	2718	653	5186	1346	665
3	618	1197	2930	653	5398	1450	665
4	621	1196	2833	428	5078	1402	436
5	623	1197	2848	308	4976	1410	314
6	626	1376	2760	798	5560	1368	814
7	616	1053	2942	560	5171	1458	530
8	794	1195	2807	324	5120	1390	320
9	528	1196	2829	2488	7044	1399	2530
10	916	1244	2811	162	5129	1390	166
11	430	1146	2848	***	-	1410	-

* Includes 48.5 pounds for stator cooling
** Includes 50 ft^2 for stator cooling
*** Required radiator temperature was less than sink temperature

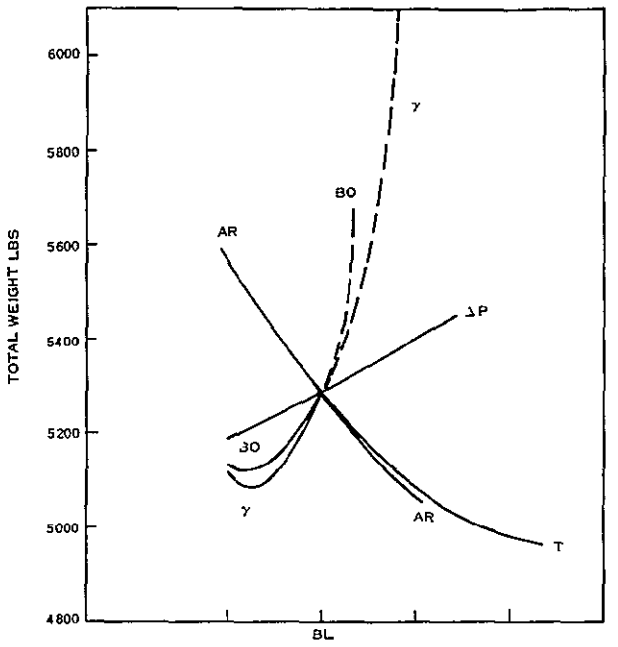

γ	0 8	1 0	1 2	
T		200	250	300
AR	2.75	3 00	3 25	
ΔP	$1.5X10^4$	$2.0X10^4$	$2.5X10^4$	
BO	0 46	0 48	0 50	

Figure 2-17. Total Weight Variation

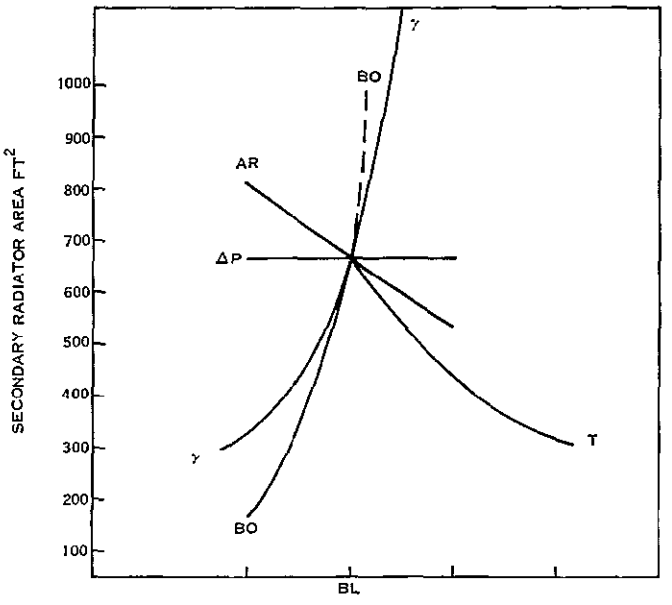

γ	0 8	1 0	1 2	300
T		200	250	
AR	2.75	3 00	3 25	
ΔP	$1.5X10^4$	$2.0X10^4$	$2.5X10^5$	
BO	0 46	0 48	0 50	

Figure 2-18. Secondary Radiator Area Variation

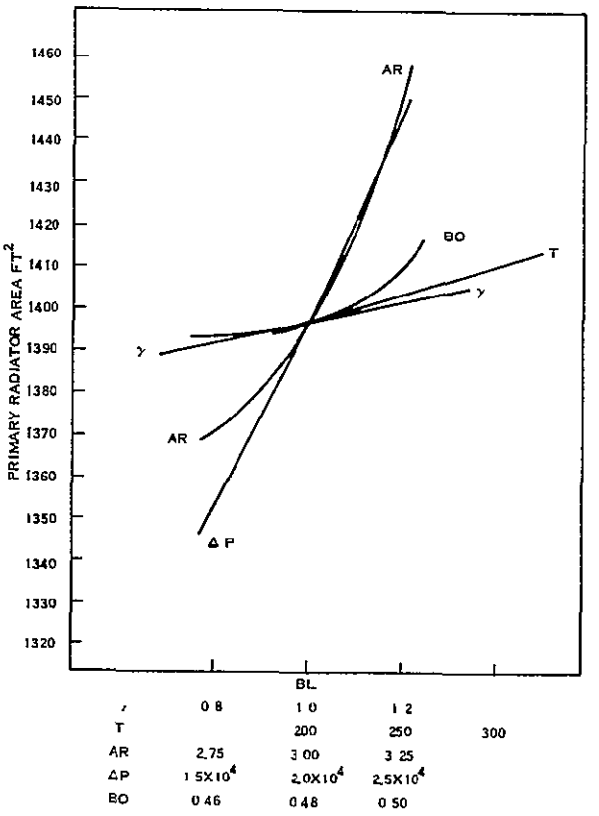

Figure 2-19. Primary Radiator Area Variation

TABLE 2-10. PARAMETERS VARIED IN DESIGN SELECTION (RUNS 12 TO 20)

Run No.	Coil Ratio γ	Coil Temperature T_c (°C)	Inlet Field B_o (Wb/M^2)
12	0.8	200	0.46
13	0.8	250	0.46
14	0.8	300	0.46
15	0.9	300	0.46
16	1.0	300	0.46
17	0.9	250	0.47
18	1.0	250	0.47
19	0.9	300	0.47
20	1.0	300	0.47

TABLE 2-11. PARAMETRIC WEIGHTS AND AREAS (RUNS 12 TO 20)

Run No.	Weight - Pounds					Areas - Ft^2	
	Generator	Capacitor	Primary Radiator	Secondary* Radiator	Total	Primary Radiator	Secondary** Radiator
12	1259	1097	2814	128	5298	1392	131
13	1261	1098	2823	107	5289	1398	109
14	1263	1098	2832	95	5288	1400	97
15	1052	1098	2837	100	5087	1405	103
16	915	1099	2841	109	4964	1406	111
17	841	1075	2828	156	4900	1399	160
18	744	1075	2833	189	4841	1400	193
19	843	1076	2840	126	4885	1406	129
20	747	1076	2845	154	8422	1410	158

* Includes 48.5 pounds for stator cooling
** Includes 50° ft^2 for stator cooling

2.4 POWER SYSTEM SYNTHESIS

Before attempting the design and analysis of the baseline MHD powerplant, two basic questions had to be considered in order to synthesize a rational MHD power system. These two questions are the method of system startup and whether a one-loop or two-loop system is used.

2.4.1 MHD POWER SYSTEM STARTUP

As indicated in Section 1 of this report, MHD power system startup and control techniques are to be analyzed in Phase II of this study. It has been recognized, however, that some preliminary evaluation of startup techniques must be made early in Phase I in order that the arrangements and design layouts may include all the components such as valves, lines, and reservoirs which will be needed for plant operation. Therefore, discussions of MHD system startup techniques were held with Dr. Elliott, the principal scientist developing this system, during the first quarter of this study and a startup technique was identified.

2.4.1.1 Startup Requirements

Operation of this MHD power system requires steady two-phase flow in the MHD nozzles with phase separation at the generator entrance. The cesium needs heat from the lithium to boil and expand down the nozzle; the lithium needs the mechanical force of the expanding cesium to be accelerated down the nozzle. Thus, neither fluid stream can pass through the nozzles alone. In addition, some of the kinetic energy imparted to the lithium by the cesium in the nozzles is needed to pump the lithium. The first conclusion is, therefore, that the two streams must start into the nozzles together.

The NaK/N_2 test system (see Subsection 2.3) has been started by simultaneous injection of the two fluids into the empty nozzle with stable flow being achieved in seconds. The NaK/N_2 system is a cold test system with the compressed energy of the nitrogen providing the kinetic energy rather than heat taken from the NaK stream. In the hot Li/Cs system the simultaneous injection startup can be expected to work only if there is enough thermal energy in the lithium stream to cause boiling and expansion of the cesium at once, sufficiently to establish self-sustaining flow conditions. Some reduced temperature level may suffice to start system flow; however, lacking any detailed analysis or test data to support that conjecture, the second

conclusion is drawn with regard to startup technique - namely, that the two fluids will be injected at or near normal operating temperatures.

If the two fluids are to be injected into the nozzles for startup and steady state is to be achieved in seconds, the nuclear reactor heat source must already have been taken critical and warmed up since the nuclear reactor can probably be designed to take a large power swing in a matter of tens of seconds but requires hours to be taken critical and warmed up. It is reasonable to assume that aerospace nuclear safety considerations will require that the reactor does not go critical until the spacecraft is in a high, long-life orbit. Thus, a third conclusion about startup techniques can be drawn, startup injection will not take place until the spacecraft has been in orbit for hours. A reasonable time limit of five hours can be estimated by allowing one hour for orbit ephemeris verification and four hours for achieving criticality and warmup.

The two fluids of the MHD system, lithium and cesium, have melting points of 357^{o}F and 84^{o}F, respectively. Since the spacecraft will be in orbit at least onehour before the lithium begins to receive heat from the reactor, the lithium must be preheated before launch to prevent fluid freezing. The cesium, with a much lower freezing point, poses far less a problem. In order to fill the lithium system on the launch stand it will have to be preheated and then filled with hot molten lithium to assure complete fill. Thus, a fourth conclusion about startup is drawn, the lithium systems will be preheated and launched hot. The results of previous studies such as SNAP-50/SPUR indicate that preheat to 500^{o}F should be adequate. The cesium system should receive enought heat from the lithium system to preclude freezing in it, although some way to warm up the radiator is needed.

The general requirements for the startup techniques can then be summarized:

a. Startup will be by simultaneous injection of lithium and cesium into empty nozzles

b. The two fluids will be injected at their normal operating temperatures

c. Startup will take place only after about five hours in orbit

d. The lithium system will be preheated to 500^{o}F at launch.

2.4.1.2 System Arrangement for Startup

Figure 2-20 is a schematic diagram of the MHD fluid system with the necessary valves and other equipment added so that the system can be started. The entire system can be evacuated through the four evacuation and fill connections with the following valve lineup:

LV-1	open
LV-2	open
LV-4	open to reactor bypass line
CV-1	open
CV-2	open

After the system is evacuated, LV-1, LV-2, CV-1 and CV-2 are closed and the cesium and lithium sections are filled through their respective fill connections. Preheating of the lithium piping and the reactor can be accomplished by circulating hot inert gas through their insulating jackets.

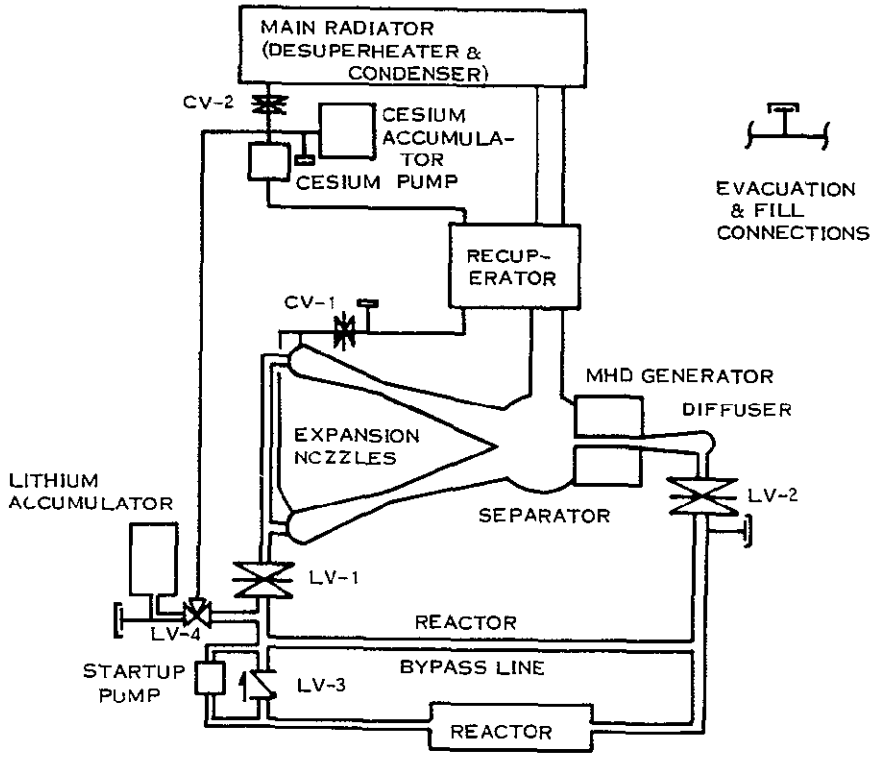

Figure 2-20. MHD Fluid System Startup Schematic

After reaching a safe orbit, the reactor is taken critical and warmed up, circulating the lithium at a low flow rate with the battery-powered startup pump located in parallel with check valve LV-3. The lithium flow path is normal through the reactor section but is reverse throught the reactor by-pass line. The cesium system is stagnant but shares the same insulated enclosure with all of the lithium system except the reactor and is, therefore, warmed up by radiated and conducted heat. System pressures are maintained by controlling the gas pressure acting on the two bellows type accumulators; the two accumulators absorb the fluid expansion volume during warmup. Battery power is also provided to operate the auxiliary cooling pumps during warmup.

When operating temperatures are reached, accumulator gas pressures are increased and valves LV-1 and CV-1 open, injecting the two fluids into the nozzles. After appropriate intervals, valves LV-2 and CV-2 are opened to complete the normal flow paths. The startup pump is secured and valve LV-4 switches the lithium reservoir connection over to the cesium pump suction to minimize the containment pressure requirements during long term operation. Cesium and lithium makeup to the system for leakage or volume expansion due to creep enter the system at the cesium pump suction controlled by accumulator gas pressure.

2.4.2 SHUTDOWN AND RESTART

The reference mission has a coast period halfway to Jupiter and the Jupiter orbit operation, both of which have a nominal ten percent power demand (See Paragraph 2.1.1). There is no estimate of the overall operating efficiency of the MHD power system when operating at ten percent output. If operation at ten percent rated output is achievable only at extremely low system efficiency, it might be worthwhile to shut down the MHD loop and operate the reactor at low power using an alternate conversion system, e.g., thermoelectrics, to generate power.

For the reference mission the low power demand time is 120 + 17 = 137 days out of 50 + 160 + 120 + 270 + 17 = 637 days or $\sim$ 22 percent of the mission (more with longer time in Jovian orbit). If an alternate conversion system with equivalent efficiency ($\sim$ 7 to 8 percent) is available and the MHD loop can be shut down, the reactor core life required can be reduced to

$$\frac{500 + 0.08(137)}{637} \times 100 = 80\%$$

of the life required for continuous operation at rated power. Even without examining the possible difficulties of MHD loop shutdown and incorporation of a second power conversion system, the $\sim$ 20 percent saving in core design life does not seem a strong incentive for design change.

To restart the MHD system after an in-space shutdown, it is assumed that the original startup conditions must be restored in shutting down the system. Two shutdown approaches were considered. In the first, an exhaust connection would be added to the diffuser downstream of the MHD generator. The system would be shutdown by closing valves, LV-1, LV-2, CV-1, and CV-2 and opening the exhaust port simultaneously. The hot fluids in the nozzles and vapor spaces would boil off into space and, with the exhaust port reclosed, the system would again be ready for startup if the accumulators contained sufficient fluid inventory. This method was rejected for many reasons, namely:

a. The spacecraft would receive a large impulse from fluid exhaust just after its attitude control system (the thrusters) was shut down.

b. The exhausted liquid metal may contaminate spacecraft surfaces

c. The lithium and cesium reservoirs would require additional inventory for restart capability.

The second shutdown technique considered was to first close valves LV-1 and CV-1 and simultaneously lower the gas control pressures on the accumulators (the lithium accumulator is assumed to be valved back to the reactor by-pass line). The generator electrical circuits are then opened to minimize flow resistance and fluid momentum is relied upon to drive as much fluid as possible back into the accumulators. When sufficient fluid has been drawn out of the nozzle, generator and vapor spaces, valves LV-2 and CV-2 are closed to complete the shutdown. Successful execution of this type shutdown would require careful control and judgement of its feasibility would require extensive analysis. In the scope and context of this study and in view of the modest core life reduction to be attained, this analysis was not considered worthwhile.

If the MHD system cannot be shutdown but cannot operate stably at the low power levels required by the mission, it may be necessary to include a means of dissipating excess power. If this had to be taken out as electrical power, it would require a power flattening radiator of $\sim$ 100 ft^2 (assuming radiator operation at 1000 to 1200^{o}F). A radiator of this size would add less than four feet to the length of the spacecraft. As an alternate the power flattening resistor could be located in the lithium flow path so that it would be liquid cooled. This second approach would probably be the lighter and would not add to the spacecraft length. Since neither power flattening design would impose serious design penalties on the spacecraft, it is considered safe to assume stable part power operation pending detailed analysis.

2.4.3 ONE OR TWO-LOOP SYSTEM

2.4.3.1 Reactor Loop Arrangement

In order to provide the MHD loop with 1600 to 2200^{o}F lithium, a fast spectrum, lithium-cooled reactor such as SNAP-50 is a logical choice. With such a reactor, the reactor coolant may be used directly in the MHD loop or an intermediate heat exchanger may be used to separate the reactor and MHD loops. Figure 2-21 shows the basic MHD cycle diagram with the reactor piped directly into the MHD loop. The movement of fluids in the MHD loop depends on the cesium stream receiving thermal energy from the lithium when the two streams are mixed in the nozzles. The boiling and expanding cesium then imparts kinetic energy to the lithium stream, part of which is converted to electrical energy in the MHD generator and part of which is converted to pumping pressure in the diffuser to circulate lithium back through the reactor and to the nozzles. The optional bypass shown in Figure 2-21 can be used to divert some of the lithium flow around the reactor in order to obtain a lower reactor pressure drop or a more compact reactor.

If the reactor loop is separated from the MHD loop by a heat source heat exchanger as shown in Figure 2-22, an additional pump is needed to circulate the lithium through the reactor loop.

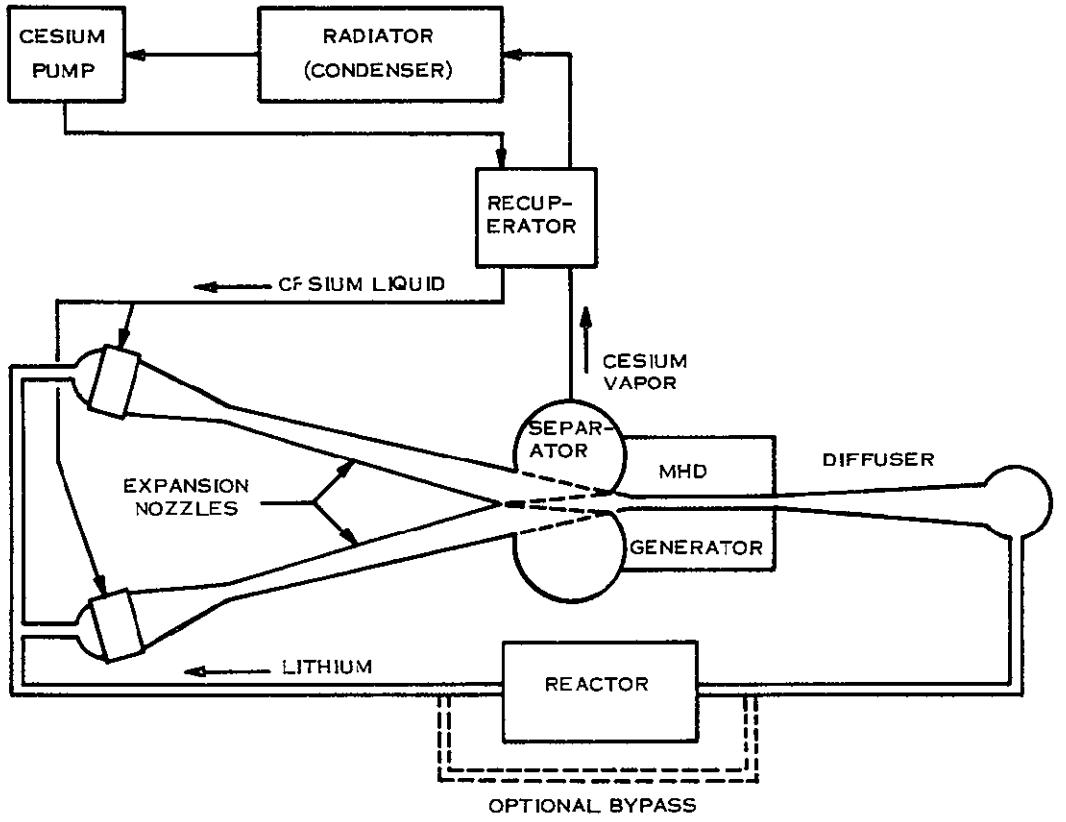

Figure 2-21. MHD Loop Without Separate Reactor Look

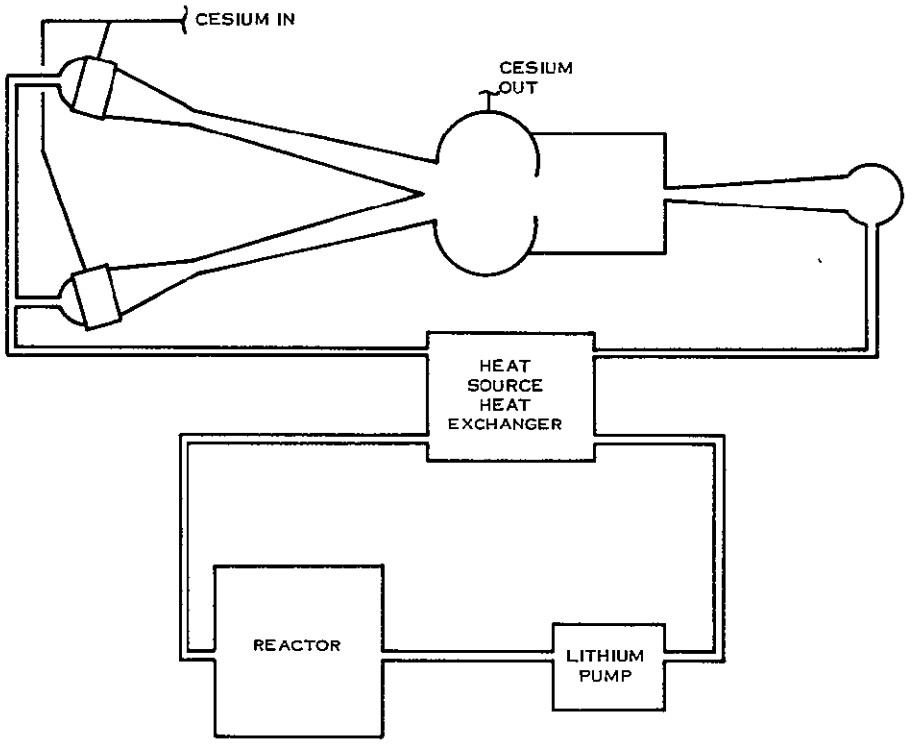

Figure 2-22. MHD Loop With Separate Reactor Look

The incentives for use of a separate reactor loop are:

a. The reactor pressure vessel may be designed for a containment pressure lower than the 150 psia typical of the MHD loop

b. Ingestion of cesium by the reactor, with subsequent bubble formation, is precluded

c. Activated coolant is kept away from the payload

The incentives for a one-loop system are:

a. The system is simpler and lighter

b. Lithium can be circulated for prestart warmup (see startup discussion in Paragraph 2.4.1) using just one pump. A two-loop system could also use just one pump if all lithium in the MHD circuit is left stagnant and warmed by conducted heat.

c. Only one lithium accumulator is needed

d. No reactor coolant pumping is needed once the system is started.

2.4.3.1.1 Containment Pressure - The weight penalty associated with designing the reactor for MHD pressure may be approximated as follows:

a. Assume a domed cylindrical pressure vessel of 12-inch diameter and 40-inch length made of Cb-1Zr. This size and material are typical of the MHD type reactor

b. Assume that the reactor pressure vessel would have a minimum design pressure of 50 psia

c. Assume that the reactor pressure vessel design stress for 20,000 hour operation is 1000 psi. This low design stress is quite conservative for temperatures below $\sim 2000^{\circ}F$. More advanced alloys of Cb can provide much greater creep strength.

Calculating a minimum vessel wall thickness:

$$t = \frac{Pr}{\sigma} = \frac{50 \text{ psi} \times 6 \text{ in.}}{1000 \text{ psi}} = 0.3 \text{ in.}$$

Design for 150 psia would revise this to:

$$t = \frac{150 \text{ psi} \times 6 \text{ in.}}{1000 \text{ psi}} = 0.9 \text{ in.}$$

An increase of 0.6 inch in wall thickness.

The surface area of the vessel is about 1500 square inches and the wall material density is 0.32 pounds per cubic inch, so the weight increase would be:

$$1500 \text{ in}^2 \times 0.6 \times 0.32 \text{ lb/in}^3 \approx 300 \text{ lb.}$$

Since the weight penalty is only about 300 pounds even with the conservative material and design stress selection, the additional complexity and weight of a separate reactor loop, pump and heat source heat exchanger would constitute a greater penalty. In weight comparison, the heat source heat exhanger alone, with one side designed for 150 psi, would weigh almost as much.

2.4.3.1.2 Cesium Bubbles - The second-listed incentive for a two-loop system is to keep cesium bubbles out of the reactor. The fluid conditions at the MHD generator inlet behind the upstream diffuser are such that all remaining cesium should be dissolved. If any bubbles do still exist at the generator exit they may still dissolve when static pressure is increased from $\sim$ 40 psia to $\sim$ 150 psia in the downstream diffuser. If still not dissolved, any cesium bubbles would more likely follow the bypass line ($\sim$ 80 to 85 percent of the flow) rather than enter the reactor line ($\sim$ 15 to 20 percent of the flow). Lastly, if the reactor core is of one-pass design, as is most likely, cesium bubbles would collect in the inlet or outlet plenum rather than in core fluid passages where they would be swept through. Collection of cesium vapor bubbles in one of the reactor fluid plena is not expected to have a significant effect on reactor performance.

2.4.3.1.3 Coolant Activation - Radioactivity in the reactor coolant may reach areas near the payload in a one-loop system which may cause radiation damage. In the lithium-cooled MHD reactor two basic sources of coolant radioactivity can be identified - leakage of fission products from reactor core fuel elements into the coolant and irradiation of the coolant itself during its passage through the reactor. Considering coolant irradiation first, three nuclear reactions are of interest:

$$Li^6 + n \longrightarrow H^3 + \alpha$$

$$Li^7 + n \longrightarrow Li^8 + \gamma$$

$$Cs^{133} + n \longrightarrow Cs^{134} + \gamma$$

The first of these reactions poses no high radiation threat to equipment since tritium is a weak β emitter. However, the Li^6 reaction does produce non-reactive, non-condensible helium, which can buildup in the system. The tritium will react with lithium to form LiH. The Li^6 reaction can be suppressed by using lithium coolant which is at least 99.9 percent the Li^7 isotope. Such Li^7 enriched lithium is available; natural lithium is already ~ 93 percent Li^7. The Li^7 reaction is of interest because of the Li^8 isotope formed emits a very high energy β (~ 13 Mev). However, its half-life of 0.85 seconds is so short that most should decay before coming past the shield; this delay time can be extended by including an enlarged section in the reactor outlet line. In addition, the MHD loop itself keeps the lithium from approaching the payload.

2.4.3.1.4 Cs^{134} Activity - The Cs^{133} (n, γ) Cs^{134} reaction produces two isomers, the 2.9 hour half-life Cs^{134m} and the 2.3 year Cs^{134}. These nuclides can be formed by irradiation in the reactor of the cesium dissolved in the lithium stream (natural cesium is 100 percent Cs^{133}). In order to evaluate this activity, one must have good knowledge of:

a. Cesium flow distribution (residence time in reactor, residence time near the payload, mass flow rates, and total inventory)

b. Definition of the reactor neutron flux by neutron energy level for each reactor region of interest (annulus, inlet plenum, core, and outlet plenum)

c. Cs^{133} cross section data for each energy level of interest

d. Location of sensitive components with respect to the activated cesium.

Since the system, and especially the reactor, designs are both conceptual at this time the cesium activation was analyzed by using the best available information, making estimates, where necessary, and trying to keep the analysis conservative.

Figure 2-23 depicts the mass/flow/time model which was set up to represent the cesium distribution in the system. The flow distributions and cesium inventory are based on initial baseline values. The radiation source is identified as the lowest of five radiator sections and it was assumed that 10 pounds of the calculated 31 pound cesium inventory of that radiator section would be two feet away from the payload on the average (see the arrangement in Figure 2-24 in the discussion of fission product leakage which follows). The cesium flow through the reactor will vary with system operating temperature and pressure (varying cesium solubility in lithium); the calculated baseline design value was used.

The Cs^{133} (n, γ) cross sections which were used are listed in Table 2-12. The 29-hour Cs^{134m} was assumed to undergo 100 percent decay to 2.3 year Cs^{134} with the emission of a 0.13 Mev γ. The decay of Cs^{134} was assumed to be:

a. 30 percent 0.3 Mev $\beta-$ decay to Ba^{134} followed by Ba decay with the emission of a single 1.75 Mev γ.

b. 70 percent 0.68 Mev $\beta-$ decay to Ba^{134} followed by Ba decay with the emission of a pair of γ of energies 0.8 and 0.6 Mev.

The activation rate in the reactor

$$A = \int_E \int_V \Sigma(E) \quad \phi (E, r) \; d \; V \; d \; E$$

requires a knowledge of the reactor neutron fluxes in various regions of the reactor. Since the MHD reactor design is still conceptual the following values were used:

TABLE 2-12. CESIUM - 133 (n, γ) CROSS SECTIONS

Thermal Neutrons

Production of 2.9 hour Cs^{134m}		σ = 2.6 barns
Production of 2.3 year Cs^{134m}		σ = 29 barns

0.215 ev $\leq$ En $\leq$ 10 kev

$\bar{\sigma}(n\ \gamma) \approx 5$ barns	Cs^{134m}	σ = 0.5 barns
	Cs^{134}	σ = 5 barns

En = 20 kev

	Cs^{134m}	σ = 0.09 barns
	Cs^{134}	σ = 1 barn

Estimates for High E_n Range

E_n	σ 134m (barns)	σ 134 (barns)
10 to 100 kev	0.04	0.4
0.1 to 0.4 Mev	0.007	0.07
0.4 to 1.4 Mev	0.001	0.01
1.4 to 10 Mev	0.0004	0.004

DESIGN LIFE = 14,000 HRS

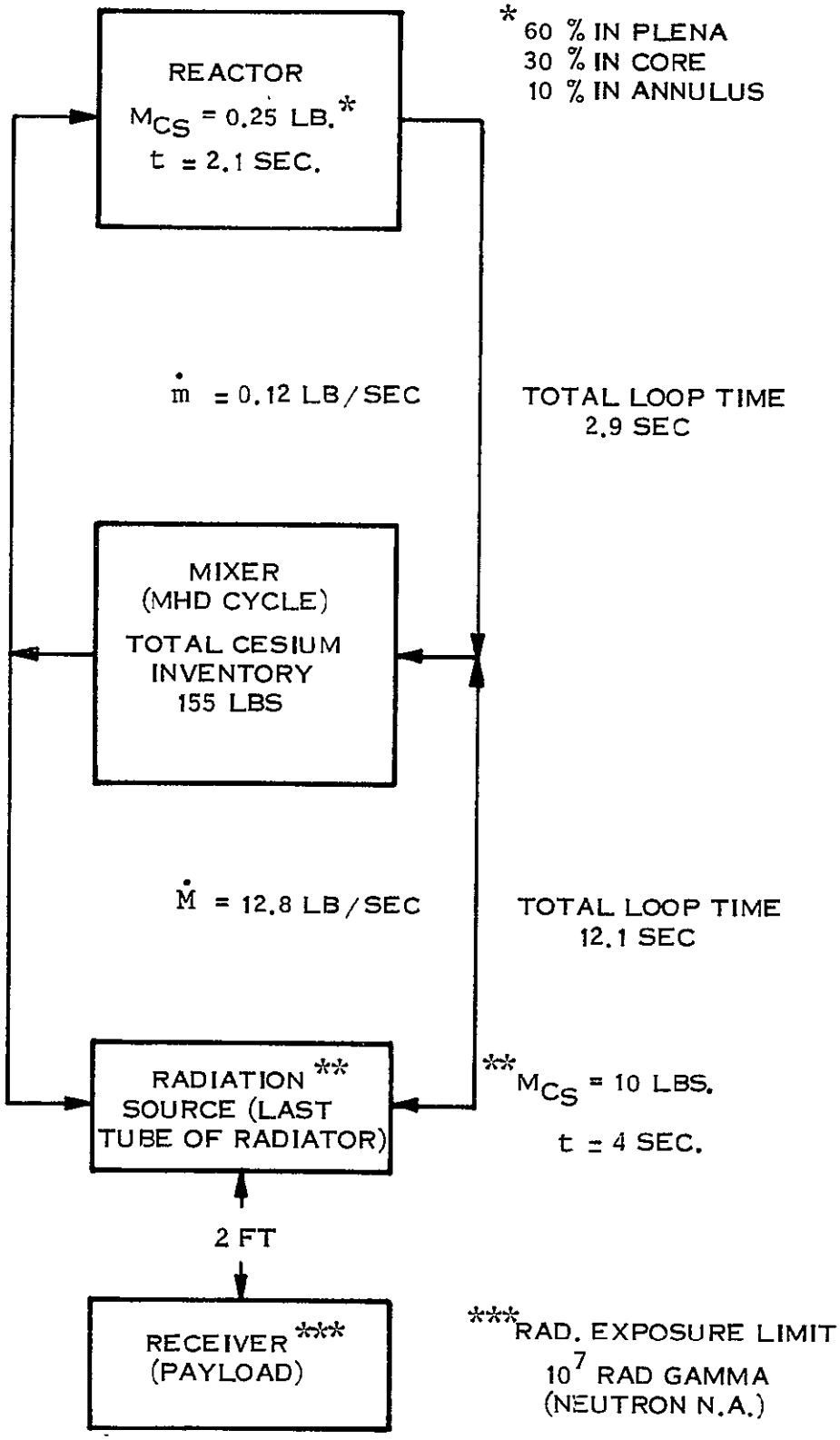

Figure 2-23. MHD Cesium Mass/Flow/Time Model

FLUX (nv)

Group	Core	Annulus	Plena
1	7×10^{13}	10^{13}	4×10^{12}
2	1.4×10^{14}	2×10^{13}	10^{13}
3	1.4×10^{14}	3×10^{13}	10^{13}
4	10^{14}	5×10^{13}	3×10^{13}
5	1.5×10^{13}	4×10^{13}	8×10^{13}
Thermal	10^{10}	5×10^{11}	2×10^{13}

These flux values are expected to be somewhat conservative for the MHD reactor since they are more closely related to reactor designs with a softer neutron energy spectrum.

The reactor average group fluxes were weighted for the time spent in the various reactor regions (see model in Figure 2-23), and the average group fluxes ϕ_g were used to calculate activated nuclei per second

$$A = V_{Cs} \sum_{g=1}^{6} \Sigma_g \phi_g$$

where

$$\Sigma_g = \sigma_g \frac{\rho_{Cs} N}{A_{Cs}}$$

A_{Cs} = molecular weight of cesium

$$\rho_{Cs} = \frac{M_{Cs}}{V_{Cs}}$$

M_{Cs} = mass of cesium

For Cs^{134m} this results in

$$A^{m} = 3.5 \times 10^{13} \text{ nuclei per sec.}$$

For Cs^{134} this, and Cs^{134m} decay, gives

$$A^{134} = 3.8 \times 10^{14} \text{ nuclei per sec.}$$

Since Cs^{134} has a half-life of 2.3 years its decay is not negligible, so correcting for decay and the 10/155 fraction which is close to the payload, the number of activated nuclei contributing dose to the payload is calculated.

$$N = 2.6 \times 10^{20} \left(1 - e^{-\lambda t}\right)$$

where

N = nuclei contributing dose

λ = Cs^{134} effective decay constant

t = time

The following dose-to-flux conversion factors were used for the emissions of interest:

0.6 Mev	$C = 8.4 \times 10^{5}$ photons/cm^2sec per R/hr
0.8 Mev	$C = 6.5 \times 10^{5}$ photons/cm^2sec per R/hr
1.75 Mev	$C = 3.5 \times 10^{5}$ photons/cm^2sec per R/hr

Assuming a point source geometry with no attenuation by the pipe walls or structure the dose as a function of time was calculated:

$$D(t) = \frac{1}{C} \int_{0}^{t} \frac{(3.6 \times 10^{3})\, N\lambda}{4 \pi r^{2}} \, dt$$

to get the following results:

Time (Hrs)	Total Integrated Dose (R)
5,000	6×10^4
10,000	2.6×10^4
15,000	4.8×10^5
20,000	8.2×10^5

The highest dose rate resulting from these calculations, 8.2×10^5, is less than 10 percent of the allowable payload dose. The dose rate at nominal design life, 14,000 hours, is about 5 percent of allowable. In view of the conservatisms of the calculation, Cs^{134} activation and consequent irradiation of the payload is not considered a severe enough problem to warrant changing to a two-loop system. It should be noted that Cs^{134} activation should be reappraised in the future, when more specific information is available, to verify this conclusion.

2.4.3.1.5 Fission Product Leakage - An analytical model was developed to represent the case of fission products leaking from the fuel elements of the reactor core into the reactor coolant stream. The model was designed to give a rough estimate of the gamma dose due to the presence of fission products in the cooling system.

a. Analytical Model - In general, the dose rate at any given point in space due to fission product leakage will depend upon:

1. Fission product leakage rate
2. Reactor operating history
3. Distribution of the fission products throughout the cooling system

When incorporating these factors into an analytical model, use will be made of a few simplifying assumptions, i.e.,

1. The reactor power level is constant in time
2. The fission product distribution is constant in time except for an arbitrary delay time between the instant of leaking and the instant of appearing distributed throughout the cooling system (this will be explained further below).
3. Once a particle of fuel leaks from the reactor core, the fission process within that particle ceases altogether. No account is taken for possible fission due to

neutrons outside of the core nor is any account taken of the possibility of the fuel particle circulating through the core with the coolant stream.

Consider the following terms,

$\ell(t) \equiv$ the fraction of the fission products in the core at time t leaking into the coolant stream per unit time

$f(r) \equiv$ the fraction of the fission products that have leaked found per unit volume at the position r.

$P(t, T, E)\, dE =$ total photon energy emission rate from a mass of fissionable fuel at a time T after the fission process had ceased. The photon energies lie in the range E to E + dE. The fuel is taken to have been undergoing the fission process at a power level of one watt for a time period t.

$W \equiv$ actual reactor operating power level

Now consider an element of volume in the cooling system at the time t', located at position r. The photon energy source can now be written as

$$S(\vec{r}, t', E)\, dE = WP(t, T, E)\, dE\, \ell(t)\, dt\, f(\vec{r})$$

where

$$t' = t + T$$

and t, which is the time at which a particle of fuel leaked, is also taken as the time for which the reactor has been operating. $S(\vec{r}, t', E)\, dE$ is the photon energy emission per unit time at time t', per unit volume at position $\vec{r}$, for photons with energies between E and E + dE, due to fuel which leaked in the time interval from t to t + dt.

The total source strength at time t', due to fuel which leaked from time t_o to time t, is

$$S(\vec{r}, t') = Wf(\vec{r}) \int_E \int_{t_o}^{t'} P(t, t'-t, E)\, \ell(t)\, dt\, dE$$

where now $T = t'-t$, since t' is being held constant. The time t_o at which leaking begins can have any value in the range

$$0 \leq t_o \leq t'$$

If one wishes to introduce a delay time between the time of leakage and the time the fission products arrive at the point $\vec{r}$, then the above expression becomes,

$$S(\vec{r}, t') = Wf(\vec{r}) \int_E \int_{t_o}^{t'-\delta} P(t, t'-t, E)\, \ell(t)\, dt\, dE$$

where δ is the delay time.

This source strength can now be used to calculate the dose rate and integrated dose at any desired receiver point. Assume that there is no appreciable attenuation of the photons as they pass from the source to the receiver point. Furthermore, let the fission products that significantly contribute to the dose be contained in space region R. If $\vec{x}$ is the distance between an element of volume of the source region and the receiver point, then the dose rate at the receiver point is

$$D(t') = WC \int_R \frac{S(\vec{r}, t')\, dV}{4\pi x^2}$$

where it has been assumed that the source emits isotropically. The term dV is a volume element in the source region and C is a suitable averaged energy flux-to-dose conversion factor. The averaging of the conversion factor is complicated by the fact that the photon spectrum is time dependent. It should be kept in mind that the distance x in the above equation is a function of $\vec{r}$, the position vector of dV.

The time integrated dose at the receiver point up to time t_m is

$$D(t_m) = \int_{t_o + \delta}^{t_m} D(t')\, dt'$$

Numerical values for the quantity P(t, T, E) dE can be found in the literature (see "Reactor Handbook", second edition, vol. II, part B, or "Reactor Physics Constants", ANL-5800, second edition). The data is given in the form of curves for the photon energy emission rate as a function of reactor operating time and time since reactor shutdown. A family of curves is given, each one representing the energy emission rate for photons with energies in a given energy range.

The total photon energy emission rate can be expressed analytically through the use of the so-called Way and Wigner formula for the emission of photon energy as a function of time after a fission event. The formula is:

$$\Gamma(\tau) = 1.26\, \tau^{-1.2} \text{ mev/sec per fission}$$

where τ is the time since fission. This is a good approximation for τ greater than about 100 seconds. Using this equation to derive an expression for P (t, T) results in

$$P(t, T) = 1.95 \times 10^{11} \left[T^{-0.2} - (T + t)^{-0.2} \right] \text{ mev/sec-watt}$$

where

$$P(t, T) = \int P(t, T, E)\, dE$$

b. Application of the Model - Consider the case of a reactor whose fuel elements leak fission products at a constant rate into the reactor coolant system. The leakage rate will be assumed to be small enough such that control adjustments to compensate for the loss do not perturb the neutron flux appreciably. Under this condition, the fission rate will be essen-

tially constant with time as long as the reactor power level remains constant. Also assume that the power density is constant throughout the reactor core.

Let there be a total loss of fuel due to leaking of p% of the total fuel mass, and let this mass loss occur over the time period $(t_m - t_o)$. Then, the leakage rate from time t_o to time t_m will be

$$\frac{(p \times 10^{-2})\, M}{(t_m - t_o)} \quad \text{mass per unit time}$$

where M is the total fuel mass. At the time t, the fuel within the reactor core would have a fission history such that if the fission process ceased at time t, then at item t+T, the total photon energy emission rate would be $W \cdot P(t, T)$, where W is the reactor operating power level. Now, the element of mass, dm, of fuel that leaks in the time interval t to t + dt will have the fraction dm/M of this photon power, and, since the model assumes that no more fissions occur within dm after leaking, one can write for the photon power to be contained within dm

$$\frac{dm}{M} \quad W\ P(t, T) \text{ mev/sec}$$

The element of mass dm can be written

$$dm = \frac{(px10^{-2})M}{(t_m - t_o)}\, dt$$

Hence, the photon power in dm is

$$\frac{(px10^{-2})}{(t_m - t_o)} \quad W\ P(t, T)\, dt \text{ mev/sec}$$

This is the photon energy emission rate, at a time T after leaking, from the mass of fuel that leaked during the time t to t + dt. It should also be kept in mind that the reactor started operating at t = 0.

The distribution of the fission products after leaking is here assumed to be a uniform distribution over the volume of the cooling system. If this volume is V, then the fraction of

the fission products found per unit volume in the cooling system is simply

$$f(r) = 1/V$$

The source strength can now be written as

$$S(r, t') = \frac{W}{V} \frac{(p \times 10^{-2})}{(t_m - t_o)} \int_{t_o}^{t'-\delta} P(t, T)\, dt$$

If the analytical expression is used for P (t, T), then

$$S(\vec{r}, t') = (1.95 \times 10^{11}) \frac{W}{V} \frac{(p \times 10^{-2})}{(t_m - t_o)} \left[\frac{(t'-t_o)^{0.8}}{0.8} + \frac{t_o}{(t')^{0.2}} - (t')^{0.8} \right]$$

The integrated dose at some receiver point is, if it is assumed that there is no attenuation of the photons,

$$D(t_m) = C \int_{t_o}^{t_m} \int_R \frac{S(\vec{r}, t')}{4 \pi x^2} \, dV \, dt'$$

When the above expression for S(r, t') is inserted in the expression for $D(t_m)$, then

$$D(t_m) = \frac{(1.95 \times 10^{11})\, W\, (p \times 10^{-2})}{4 \pi V (t_m - t_o)} C \left[\frac{(t_m - t_o)^{1.8}}{1.44} + \frac{t_o t_m^{0.8}}{0.8} \right.$$

$$\left. - \frac{t_m^{1.8}}{1.8} - 0.694\, t_o^{1.8} \right] \int_R \frac{dV}{x^2}$$

This last equation will now be used to calculate the integrated dose to the payload for the MHD-powered unmanned space vehicle. The coolant system includes both the Li and Cs

loops and, given their geometry and the receiver point of interest, the region R which significantly contributes to the dose includes only about 1 percent of the entire coolant system. As a further simplifying assumption, take the region R to be small enough so that x can be considered constant. Then,

$$\frac{1}{V}\int_R \frac{dV}{x^2} \approx \frac{1}{Vx^2}\int_R dV = \frac{V_R}{V}\frac{1}{x^2}$$

where V_R = volume of region R. Since V_R is assumed to be 1% of V, then

$$\frac{1}{V}\int_R \frac{dV}{x^2} = \frac{0.01}{x^2}$$

Now let

$x = 2$ feet

$W = 3.64 \times 10^6$ watts

$p = 0.05$ percent

$c = 1.4 \times 10^{-6}$ n/hr per mev/cm^2-sec

$t_m = 580$ days

$t_o = 0$

$\delta = 0$

The resulting integrated dose becomes

$$D(t_m) = 2 \times 10^7 \text{ r}$$

which is twice the allowable dose.

Figure 2-24 shows the arrangement of the payload bay region; the "region R" of interest is the cesium return pipe system at the bottom of the last radiator bay. Inspection of the arrangement indicates that x = 2 feet is a conservative assumption for the effective distance between a payload component and all the cesium-borne fission products in these pipes.

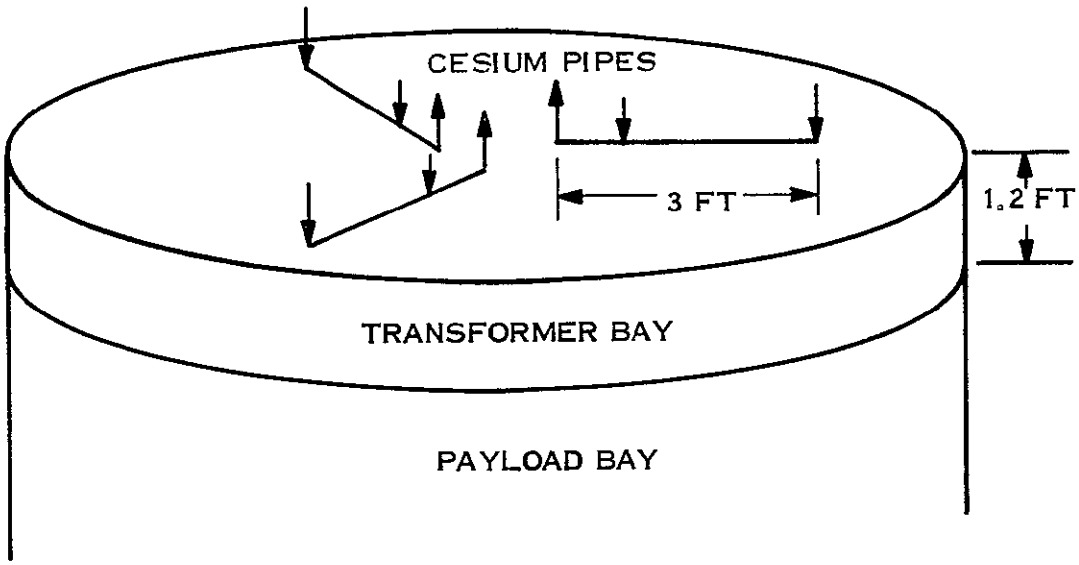

Figure 2-24. Arrangement of Cesium Pipes Near Payload

The fission product leakage of 0.05 percent is based on the assumption of 5 percent reactor fuel element failures with 100 percent fission gas release and 1 percent other fission product release from the failed elements. A gas trap was included in the cesium system to collect noncondensables which might hinder proper heat transfer in the recuperator and condensing radiator. Thus, the fluid-borne fission products are 5 percent x 0.01 = 0.05 percent. This assumption, of course, is quite arbitrary since no reactor of this type has been developed. A fast reactor of the type required may have from 100 to 1000 individual fuel pins in its core. For a flight qualified reactor, the assumption of 5 percent failures immediately after starting the flight seems conservative.

As far as the release fraction from the failed elements is concerned, 100 percent release of gaseous products is, of course, the maximum, and the assumption of 1 percent release of non-gaseous fission products is based on the element failure being local rather than total and the use of a fuel form such as UN or UC which is relatively resistant to attack by the coolant.

There is one other assumption that deserves discussion; it has been assumed that any fission products which escape the core will immediately distribute themselves around the system in the liquid phase. Clearly, the gaseous fission products will not behave in this manner, being gases they will be stripped from the lithium stream in the nozzles and passed out to the radiator. In small quantities, the fission gases may be entrained in the cesium stream leaving the radiator. With this in mind, a centrifugal gas trap was placed in the cesium line at the pump discharge; here the fission gases can be collected and held in the MHD equipment bay, far from the payload. The nongaseous fission products, on the other hand, are not so predictable. Many of these fission products such as the iodines will react with the lithium reactor coolant immediately. The reactants or the fission products may remain in stable solution in the lithium. Or they may be volatile at system conditions and move out into the radiator.

The proceeding model and assumptions calculated a dose to the payload of twice the allowable. If such an overdose were considered highly probable, other design alternatives would have to be considered. The possibilities are:

1. Include a separate reactor coolant loop
2. Rearrange the spacecraft to obtain greater separation between the radioactive fluids and the payload
3. Shield the cesium pipe

The inclusion of a separate reactor coolant loop is estimated to incur a weight penalty of 500 pounds consisting of 300 pounds for a lithium pump and power conditioner and 200 pounds for a lithium-lithium heat exchanger, additional lithium, structure, etc. The pump weight is based on a polyphase ac helical induction pump moving 30 lb/sec of 1800^{o}F lithium with a developed pressure head of 10 psi. The gross power required for the pump including power conditioning losses is estimated to be 11 kWe, assuming 20 percent pump efficiency and 97 percent power conditioning efficiency (a cycloconverter). This additional power demand would require about a 4 percent increase in system rating.

Rearranging the spacecraft by adding fixed length between the radiator and the payload is not attractive because, at 82 feet, the spacecraft is already very long. If the central structure

of the radiator had the ability to telescope the payload section away by ~50 feet once in earth orbit, the dose rate could be reduced by a factor of three. A more attractive rearrangement would be to reverse the inlet and outlet of the last radiator bay so that the more dense liquid stream would be ~15 feet from the payload instead of ~2 feet. If the fission products would be dissolved in the cesium and not plating out on system surfaces, this would reduce the dose rate by a factor of about 50.

The weight penalty associated with shielding the cesium pipes was estimated assuming half-round tungsten shielding for 9 feet of cesium pipe. As Figure 2-25 shows, about 300 pounds of shielding would reduce the dose rate from the pipes by a factor of ten.

Thus, it appears that the dose rate to the payload could be reduced significantly by rearrangement or shielding without resorting to a separate reactor loop. In view of this, and the uncertainties of the fission product leakage and transport models, the separate reactor loop was not considered a necessity at this time. Again, as was said for Cs-134 activity, the problem of fission product leakage should be reappraised in the future when better knowledge of the reactor and other factors is available.

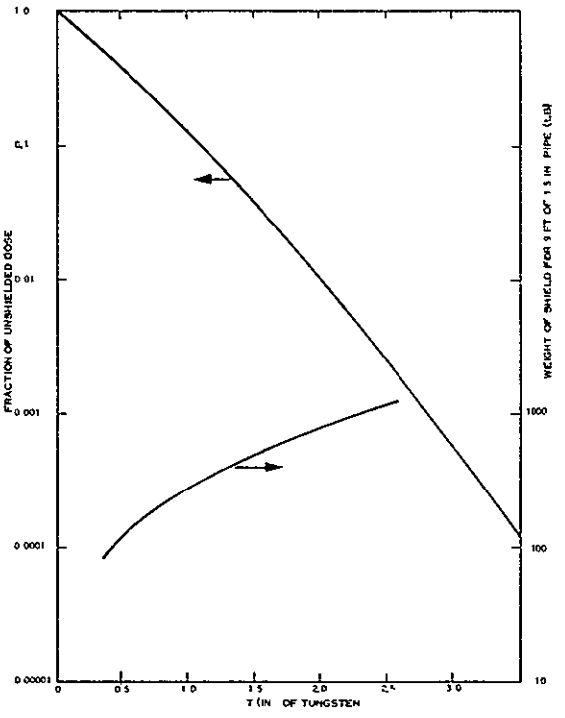

Figure 2-25. Cesium Pipe Shielding

2.5 CONFIGURATION TRADEOFFS

Since the MHD spacecraft was expected to be rather long with many heavy pieces of equipment, configuration tradeoffs were conducted to determine the most attractive design arrangement. As reported in Reference 4, a set of initial design parameters were drawn up and key component weights and areas were estimated for use in these tradeoffs.

2.5.1 GENERAL ARRANGEMENT GUIDELINES

To begin, some general conclusions were drawn about spacecraft arrangement:

a. The ion thruster subsystem includes a significant amount of electronic control and power conditioning equipment. Since this equipment will have radiation exposure limits equivalent to the payload, the payload and thruster subsystem should be located together at one end of the spacecraft with the nuclear reactor at the opposite end.

b. The ion thruster subsystem has a characteristic diameter of about ten feet in order to provide adequate mounting area for the thrusters. A nuclear reactor of the type needed here is of small diameter, no more than about three feet. Since a radiation shadow shield will be needed between the reactor and the payload/thruster area, the minimum shield diameter and weight will be obtained by locating the shield next to the reactor.

c. Working in a ten foot diameter envelope, the MHD power system requires a total radiator section some 60 to 70 feet long. Since separation of the reactor and payload/thruster area minimizes shielding thickness requirements, the radiators shall be located in a continuous section between the reactor and the payload/thruster area.

d. The MHD power generating equipment is linked to the nuclear reactor by at least two lithium coolant pipes and is connected to the payload/thruster area by the main power output cables. In addition, the MHD power generating equipment apparently does not include any items which are especially sensitive to radiation. Since the power output cables can be kept small (MHD raw output is $\sim$300 Hz, $\sim$600 Vac), the preferred location for the MHD equipment is just behind the radiation shield, near the reactor.

With these guidelines as the starting point, the preliminary arrangement studies and configuration tradeoffs were conducted.

2.5.2 MHD EQUIPMENT BAY

The MHD nozzle assembly, the MHD generator, the excitation capacitors, the recuperator, and other closely related equipment are to be located in one section or bay. Some

of these items, such as the MHD generator and nozzle assembly, must be located next to one another in order to function. Others should be close together for efficient design; for example, the excitation capacitors should be close to the MHD generator to minimize the length and, consequently, the I^2R losses of the connecting cables which carry the large exciting currents which run from the capacitors to the generator and back. (The MHD generator exciting current is about four times greater than its output power current).

Arrangement of the MHD bay was studied to determine the minimum diameter envelope which could contain this equipment so that if it is located just behind the radiation shield, the shield subtended angle (and weight and volume) would be minimized. The MHD nozzle assembly was first laid out using dimensions taken from the computer analysis of the base-line system. A 40-inch nozzle length was assumed since the JPL investigators indicated that extension beyond this length was not worthwhile. The downstream diffuser half-angle can vary from three degrees to five degrees; a three degree half-angle was assumed in order to calculate the longest difuser.

Using the nozzle assembly as the basis, the key piping and component items were arranged to establish the MHD equipment envelope size. Figure 2-26 shows an arrangement which uses a single recuperator; Figure 2-27 shows an arrangement which uses two re-cuperators, one for each side of the nozzle. In both cases, the cylindrical segments flanking the diffuser are available for capacitor location providing more than the estimated three cubic feet required, an exposed surface which can reject ~1500W of heat, and a simple interface to insulate the capacitors from the hot MHD equipment. Aside from the capacitors, the MHD stators and pump windings are the only items in the MHD bay which do not operate at $\sim 1800^{\circ}F$. It was therefore assumed that the MHD bay would be insulated on the outside surface of the envelope with the insulation envelope also providing micro-meteoroid protection. The internal components (MHD stators, etc.) which do not run at high temperature would be internally insulated and provided with a piped cooling system. The insulated exterior surface of the MHD bay can then be used as the mounting surface for this auxiliary cooling system.

The arrangements shown in Figures 2-26 and 2-27 show that the MHD equipment can be encased in a cone frustum about ten feet long with upper and lower diameters of 44

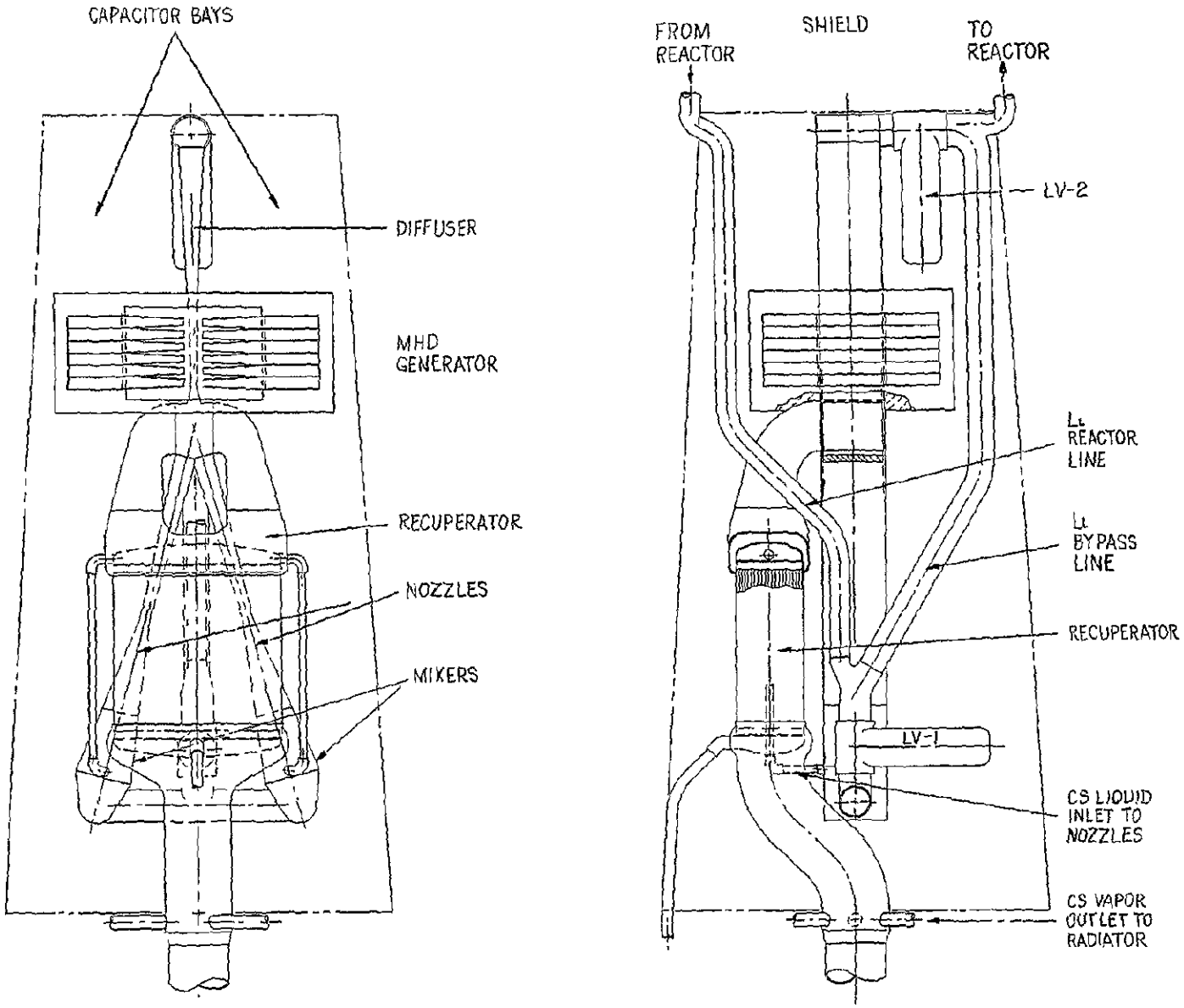

Figure 2-26. MHD Equipment Arrangement with One Recuperator

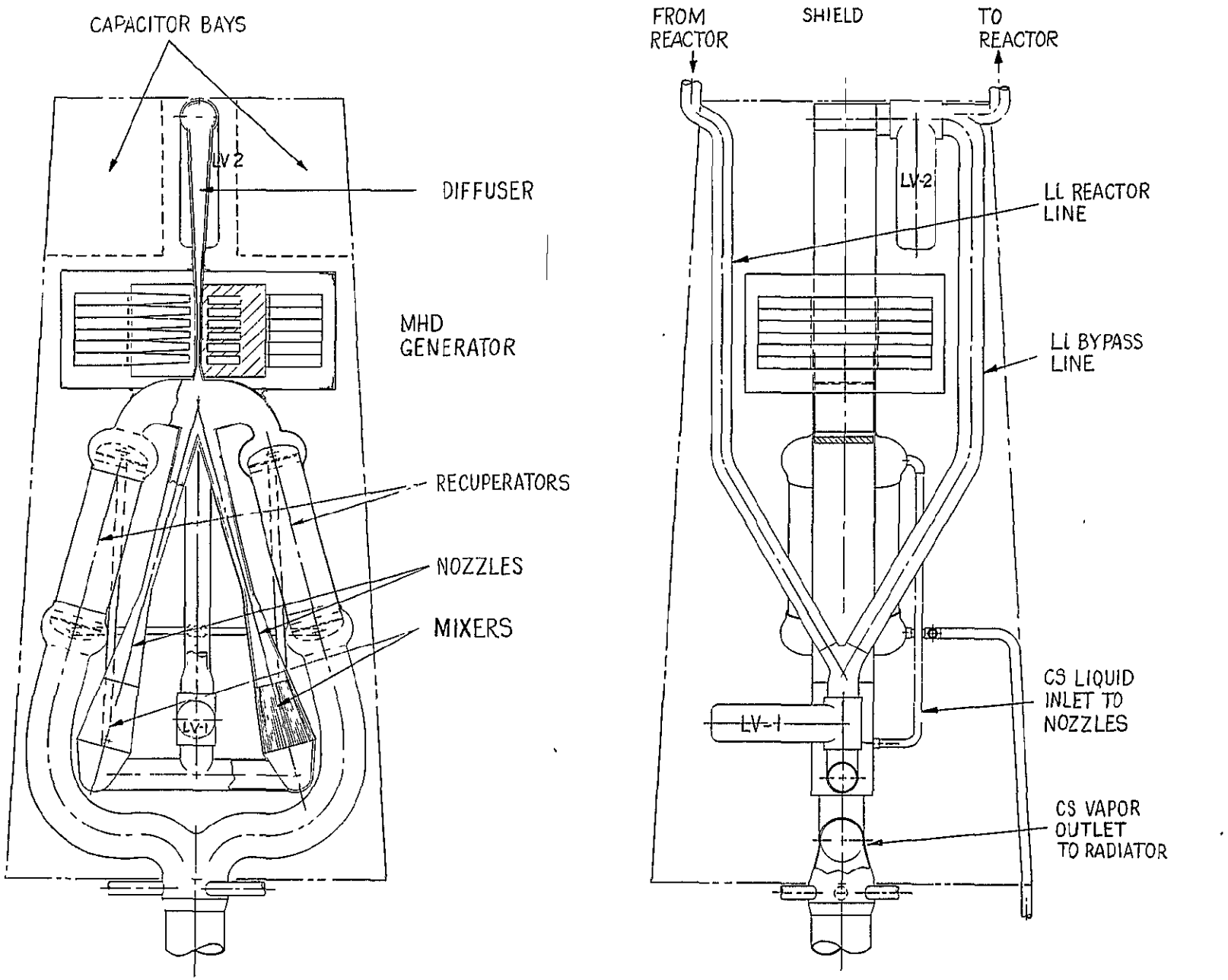

Figure 2-27. MHD Equipment Arrangement with Two Recuperators

inches and 58 inches. These diameters can be reduced somewhat by canting the MHD nozzle assembly and using a single recuperator or relocating the dual recuperators.

2.5.3 SPACECRAFT STRUCTURE

2.5.3.1 Candidate Configurations

Based on the MHD equipment arrangement possibilities which were available, five general configurations for the MHD spacecraft were drawn up. Since the Thermionic Spacecraft Study found that a cylindrical or conical radiator was lighter than a triform radiator (Reference 11), configurations with conical radiators were considered here even though the study guidelines specify a triform radiator.

Configuration No. 1 (Figure 2-28) uses a conical radiator with the radiation shield shadow projected to full diameter (ten foot nominal, nine and one-half foot actual) at the top of the payload bay. In this configuration, as in the other four, a 190 square foot secondary radiator is assigned and the MHD equipment is assumed to be located inside this radiator. In Configuration No. 1, the MHD bay is a bit slender with upper and lower diameters of 36 inches and 53 inches, but has extra length at 16.4 feet so it is reasonable to assume that all MHD equipment could be arranged in this bay.

Configuration No. 2 (Figure 2-29) differs from No. 1 only in that the MHD equipment bay is relocated down near the payload instead of just behind the radiation shield. This relocation might be made to reduce launch loads imposed on the main radiator or to move MHD equipment to a lower radiation region if the use of radiation sensitive components is found necessary.

Configuration No. 3 (Figure 2-30), using a conical/cylindrical radiator, projects the radiation shield shadow to full diameter about halfway down the spacecraft. This shield angle covers an envelope behind it which accommodates the MHD by configurations discussed in the preceding sections.

Configuration No. 4 (Figure 2-31) projects the same shield angle but with a triform radiator and a triangular shield and MHD equipment bay. This size and shape MHD bay should accommodate all the equipment.

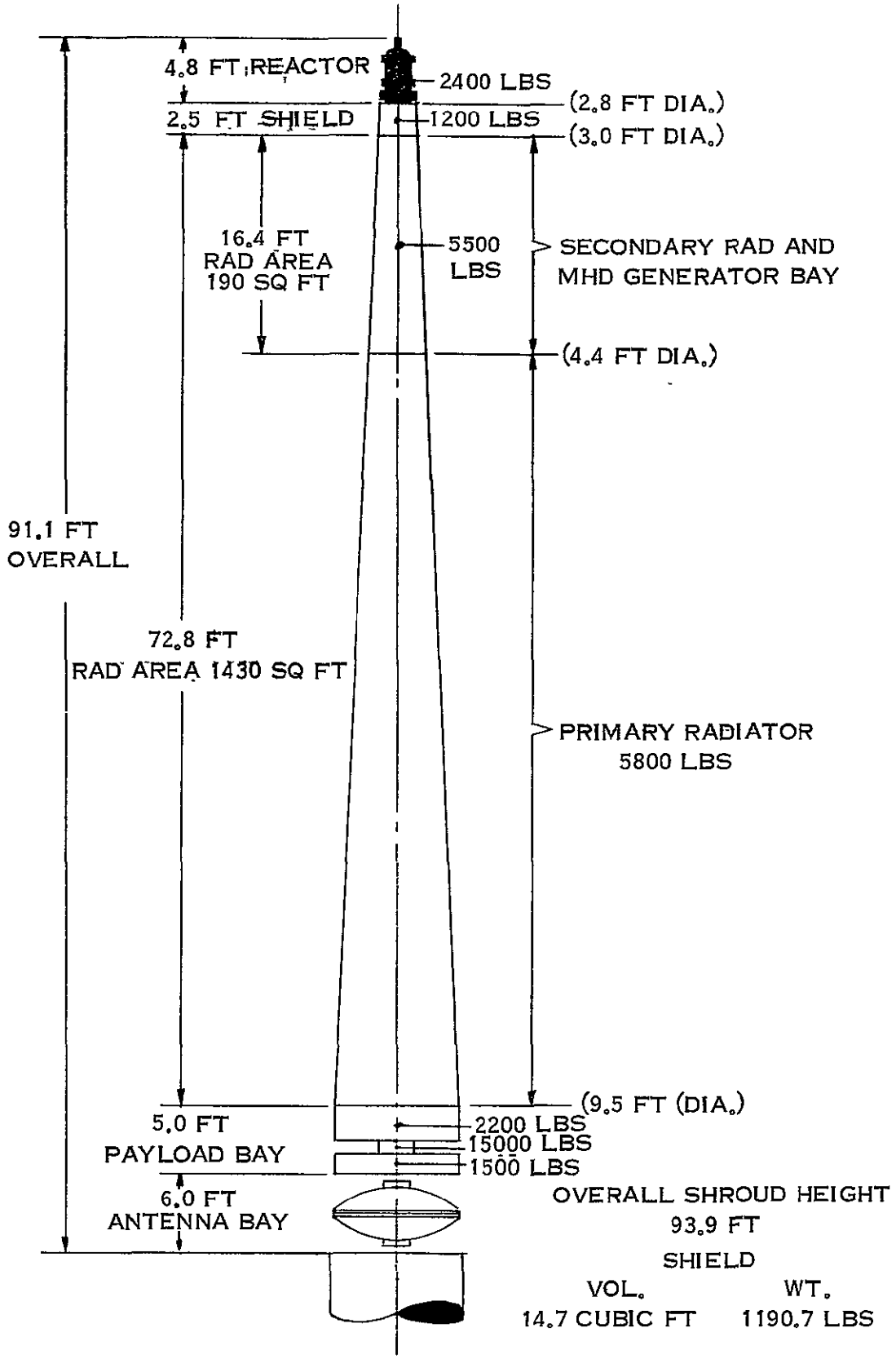

Figure 2-28. MHD Spacecraft Configuration No. 1, Conical Radiator

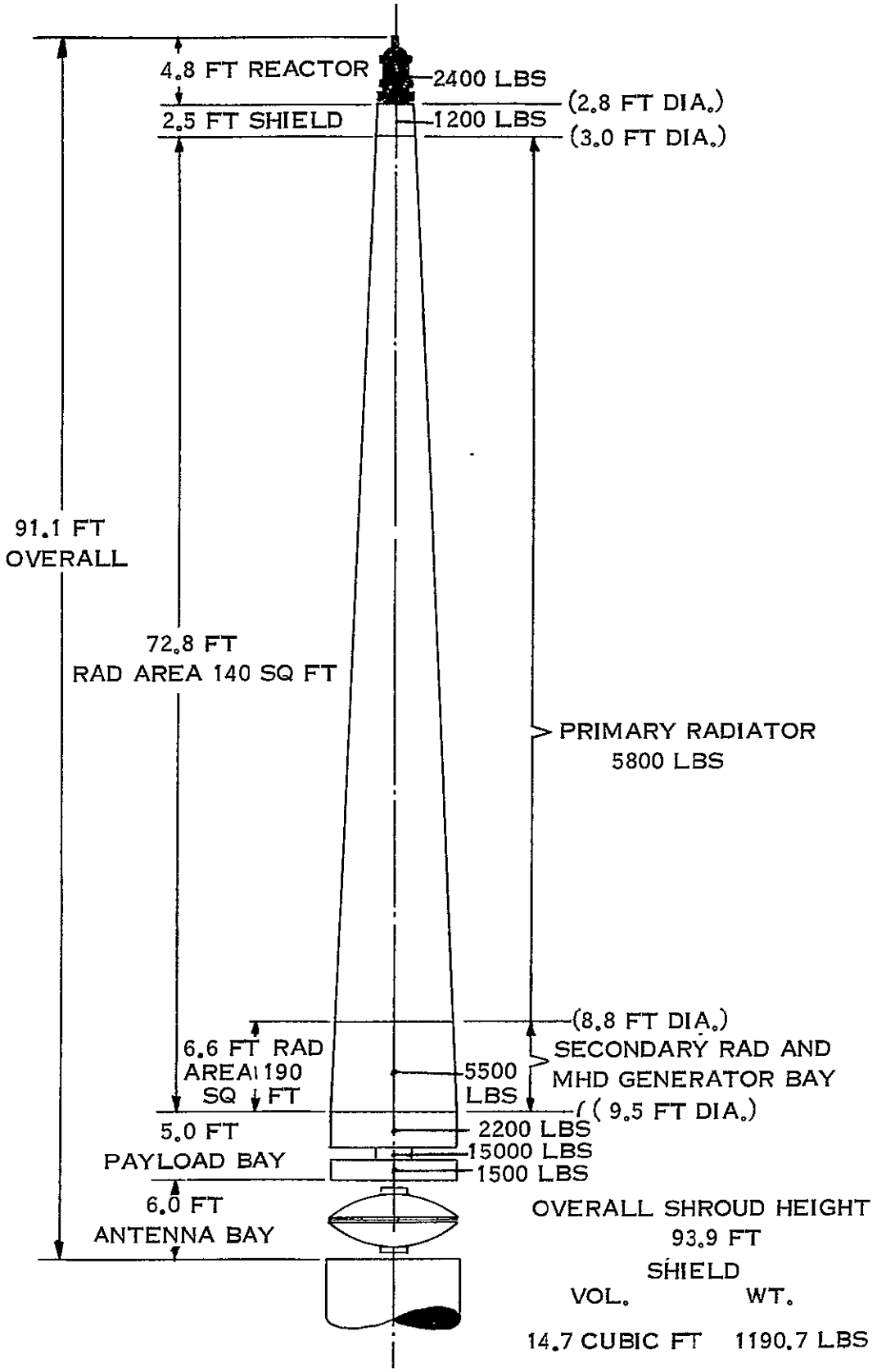

Figure 2-29. MHD Spacecraft Configuration No. 2, Conical Radiator

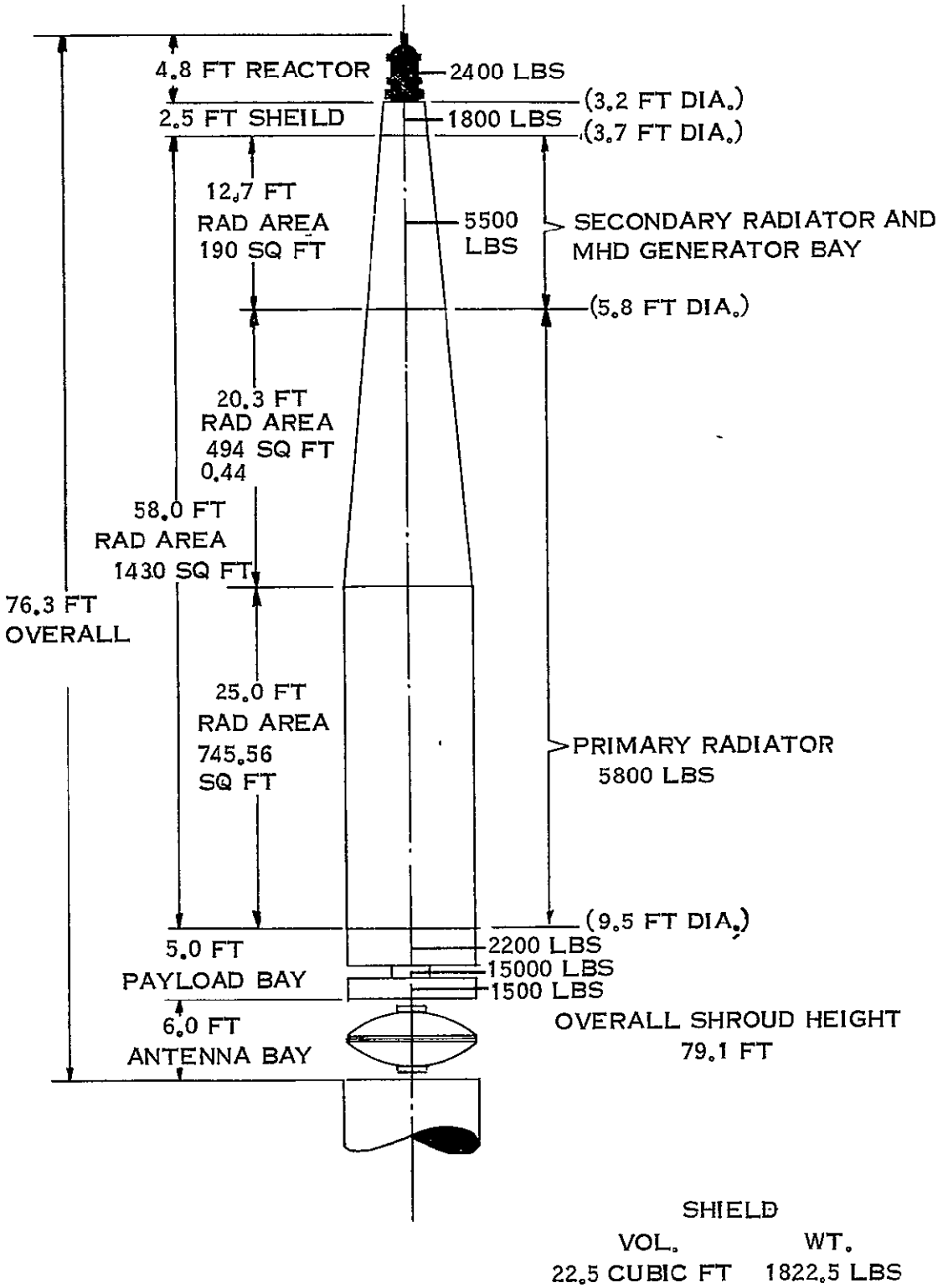

Figure 2-30. MHD Spacecraft Configuration No. 3, Conical and Cylindrical Radiator

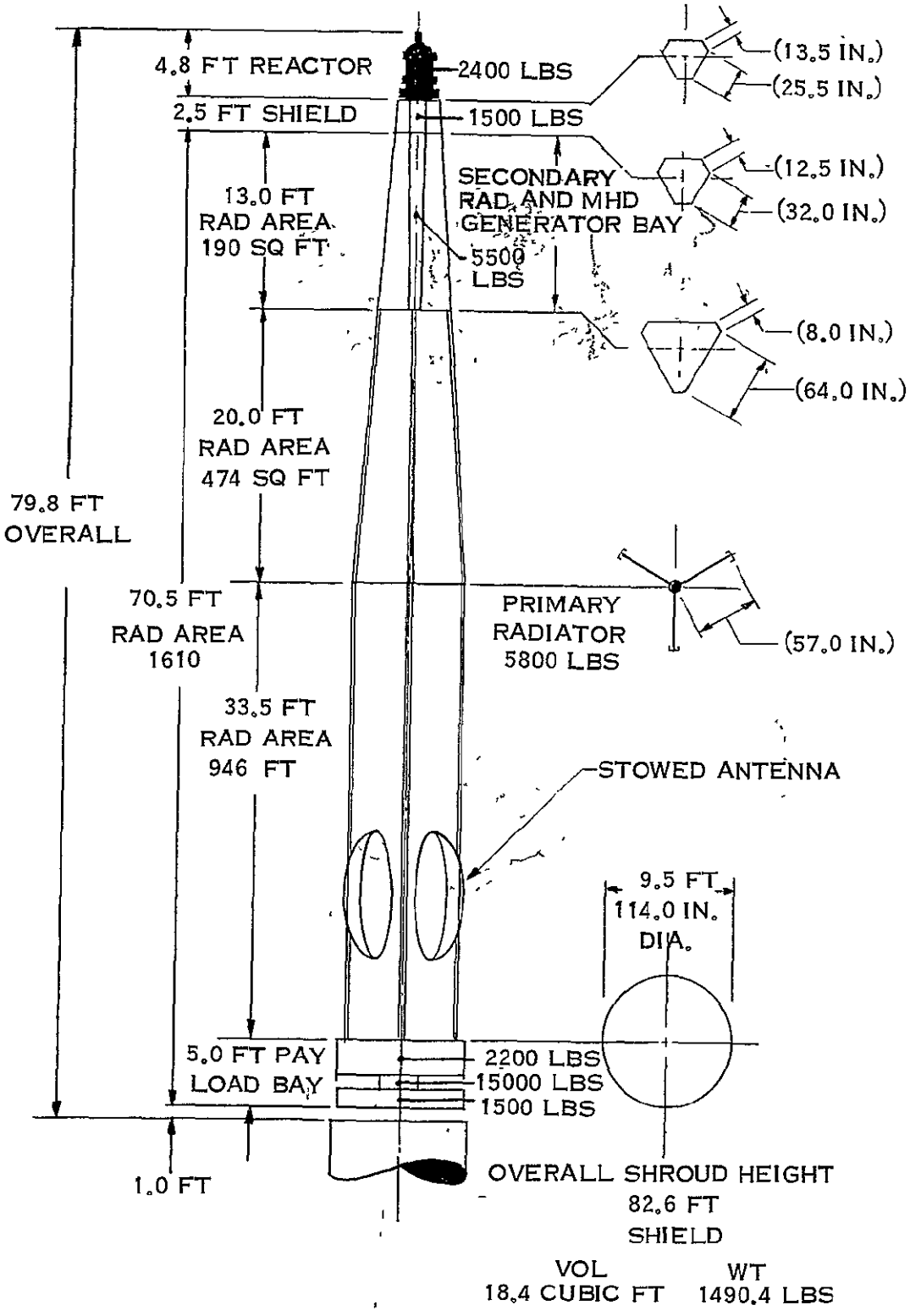

Figure 2-31. MHD Spacecraft Configuration No. 4, Triform Radiator

Configuration No. 5 (Figure 2-32) uses the triform radiator and projects the shield shadow to full diameter at the aft end of the MHD bay. This arrangement provides the shortest spacecraft and a roomy MHD equipment bay, but at the expense of increased shield weight.

In order to provide weights to be used in structural evaluation, the weights listed in Table 2-13 were assumed; these weights are based on the initial design parameters with the shield weights calculated on the basis of 80 pounds per cubic foot, assuming lithium hydride with three and one-half percent stainless steel density for structure and containment and approximately 10 pounds per cubic foot allowance for shield cooling equipment.

2.5.3.2 Structural Analysis

The purpose of this analysis is to define the structural requirements for the five candidate spacecraft configurations to enable them to survive the static and dynamic load environments. The results of this study will be factored into the selection of a basic configuration.

The candidate configurations consist of two conical configurations, one cylindrical-conical configuration and two triform configurations. In each case, the spacecraft is cantilevered from the booster interface and no structure ties exist between the shroud and the spacecraft.

Two load conditions were considered in the analysis, representing the combined static and dynamic loadings at Stage I burnout and at Stage II burnout. These are shown below:

Stage I Burnout - 3 g's lateral and 6 g's axial.

Stage II Burnout - 0.67 g's lateral and 4 g's axial.

These load conditions constitute the limiting design cases according to the booster manufacturer (Reference 12).

This analysis was limited to the primary radiator section of the spacecraft. Maximum use was made of the structural material configured for thermal requirements. The additional structure required to meet the combined static and dynamic load conditions was then identified and sized.

A summary of the additional structural weight requirements along with the maximum lateral tip deflections for each configuration is presented in Table 2-14. It should be noted that

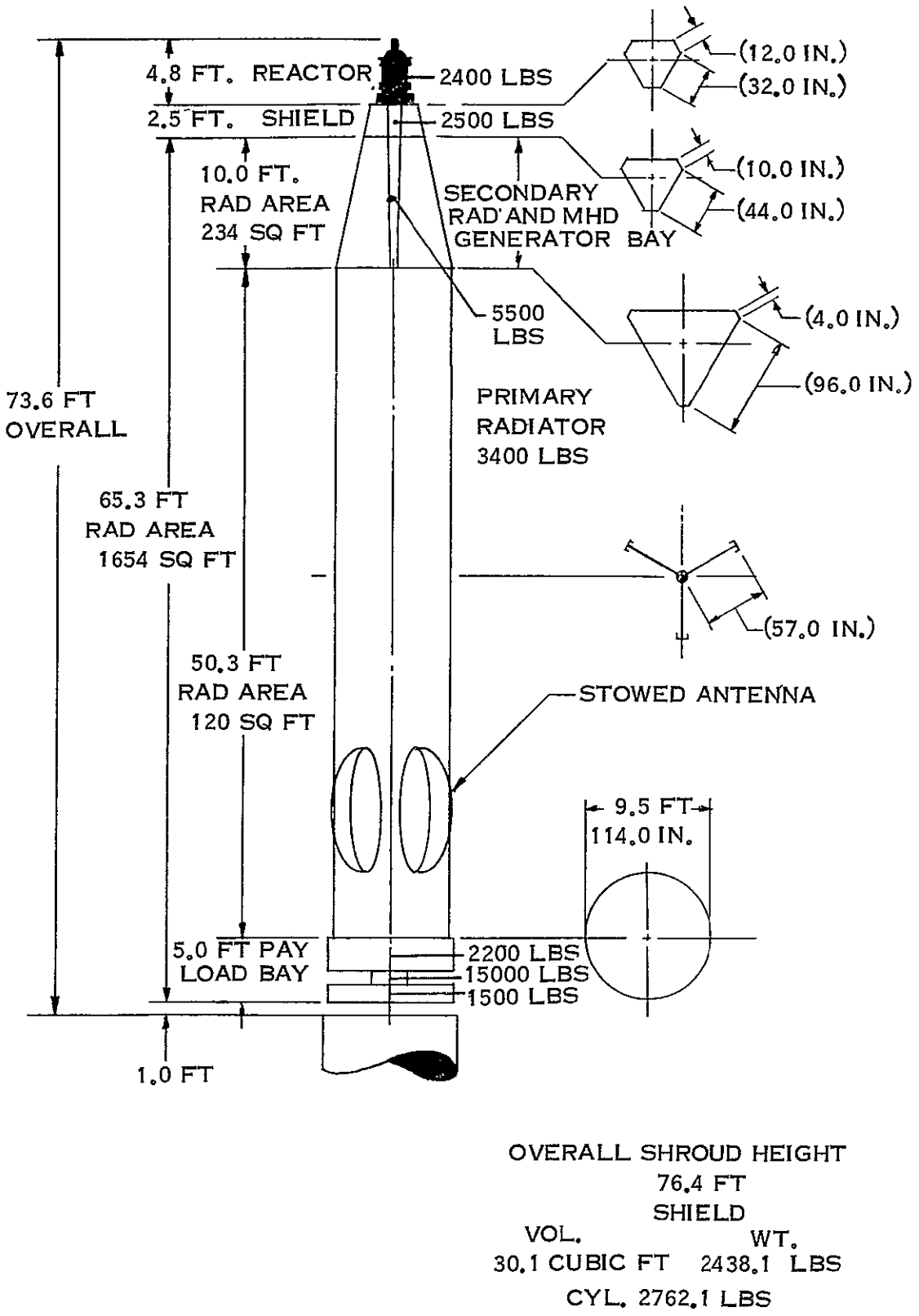

Figure 2-32. MHD Spacecraft Configuration No. 5, Triform Radiator

TABLE 2-13. MHD SPACECRAFT - WEIGHT ESTIMATES FOR CONFIGURATION TRADEOFF

ITEM		WEIGHT, POUNDS
Reactor		2400
Radiation Shield		1200 to 2500 *
Primary Radiator		3400 to 5800 **
MHD Bay		5500
Lithium Loop	400	
Cs loop	1570	
Auxiliary Cooling Loop	780	
MHD Nozzle Assembly	250	
MHD Generator	1500	
Capacitors	500	
Cables, Insulation, Etc.	500	
Payload		2200
Thruster System		1500
Propellant		15,000

* Varies with included angle; assumes 30 inch LiH with no gamma shield needed.

** 3400 pounds if triform geometry; 5800 pounds if cylindrical.

TABLE 2-14. SPACECRAFT WEIGHT AND TIP DEFLECTION SUMMARY

Configuration No.	ΔW_T	ΔW_L	ΔW_D	W_L	W_0	S_{TIP}
1	3920	3920	0	37,500	37,500	22.8
2	980	980	0	34,580	34,580	22.0
3	1030	1030	0	35,140	35,140	12.5
4	2450	250	2200	33,950	31,750	12.0
5	2370	224	2146	34,870	32,724	12.3

NOTES

All weights in pounds

ΔW_T - Total additional structural weight required

ΔW_L - Non-disposable additional structural weight required

ΔW_D - Disposable additional structural weight required

W_L - Total spacecraft weight at lift-off

W_0 - Total spacecraft weight in orbit

S_{TIP} - Maximum lateral tip deflection - inches

Configurations 1, 3, 4 and 5 each have the 5500 pound MHD generator and secondary radiator bay located near the tip of the spacecraft in contrast to Configuration No. 2 which has the MHD generator and secondary radiator bay located near the booster interface. Therefore, the loading in the secondary radiator is considerably lower for Configuration No. 2 resulting in lower structural weight. Configuration No. 3 has a comparably low structural weight because of its shorter overall length, larger bending moment of inertia, and the same number of load paths in each bay (18 vapor ducts in each bay).

The primary radiators of Configurations 1 and 2 consist of six longitudinal elements and having the shape of truncated cones with each conical element made up of a number of flat radiator panels as shown in Figure 2-33. Configurations 1 and 2 have two elements of 24 panels, two of 12 panels and two of 6 panels. Configuration No. 3 has two cylindrical elements and two conical elements containing 18 panels each.

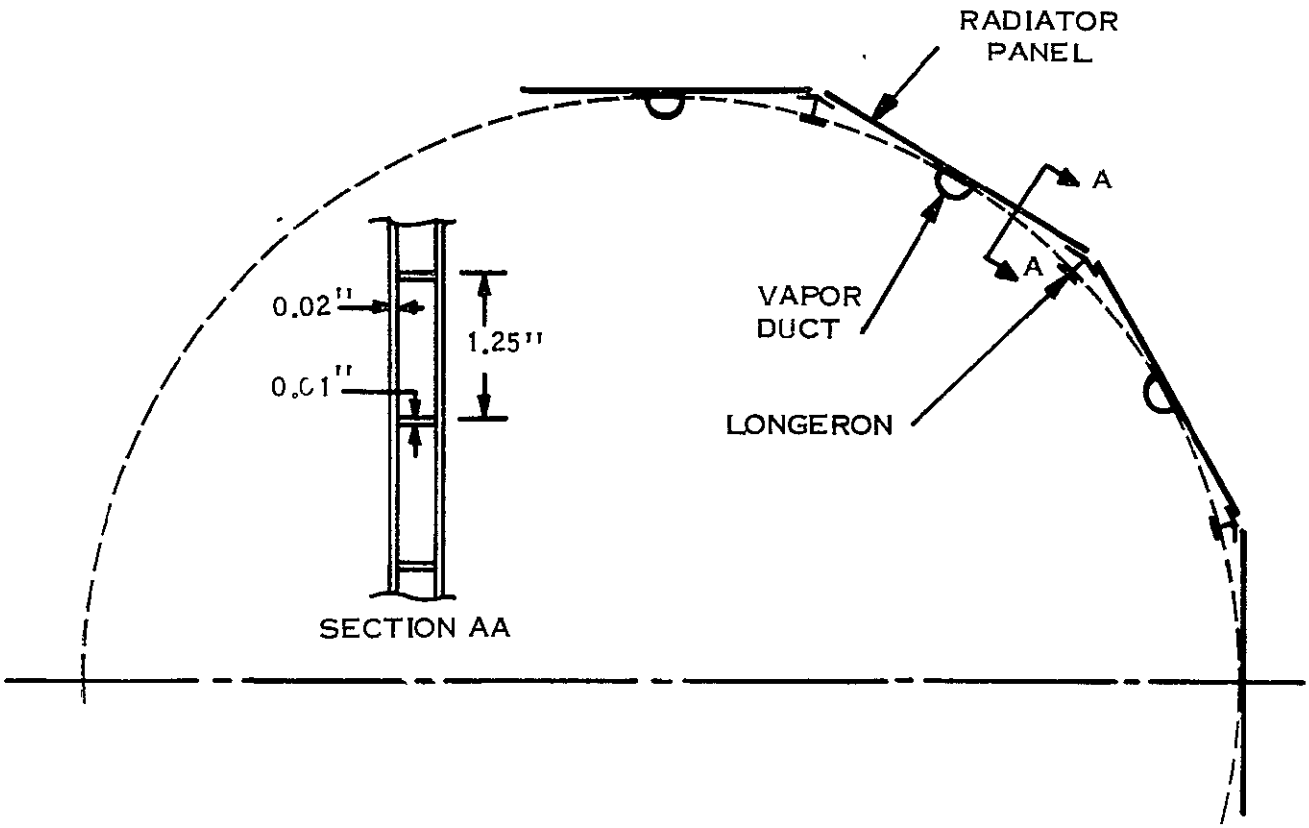

Figure 2-33. Cylindrical/Conical Radiator, Typical Cross-Section

102

A stability analysis of the 0.02-inch thick radiator panel skins employed in Configurations 1, 2 and 3 has shown that buckling will occur at about 8,000 psi, far below the 46,500 psi working stress of the 301-1/2 hard stainless steel structural material. Therefore, the panel skins were neglected as load carrying elements except in shear. The longitudinal loads are carried by the vapor ducts and the longerons located at the junctions of adjacent radiator panels. Four horizontal frames per conical or cylindrical element prevent buckling of the vapor duct and longerons. Because of the varying number of radiator panels in the conical elements of Configurations 1 and 2, load path discontinuities for the ducts and longerons exist at the junction of the conical elements. Therefore, shear panels have been provided at these junctions to redistribute the loads.

The conical-cylindrical configurations were assumed to have no disposable structure since the between-panel longerons and between-bay shear panels are expected to be impractical to jettison. Therefore, the structure sized for the maximum launch load must be carried throughout the complete mission.

The primary radiators of the triform configurations consist of flat panel elements maintained in a Y configuration by semibulkheads located at the junction of each longitudinal element. The length of a typical element is ten feet to twelve feet. Configuration No. 4 contains three 33.5-foot rectangular sections at the lower end and three 20-foot tapered sections at the upper end. Configuration No. 5 contains three 50.3-foot rectangular sections. The triform configurations have been designed using disposable structure to support the maximum Stage I burnout loads, leaving only that structure required to support the Stage II burnout loads to remain with the spacecraft throughout the mission.

To support the maximum Stage I burnout loads, 6.0 g's axial and 3.0 g's lateral, three disposable heavy channel sections are placed at the edge of the radiator and are joined to the launch vehicle at the base by a Marman clamp arrangement. Shear pins on 12-inch centers transmit the loads from the radiator structure to the support channels. Stabilizing bracing of 1-1/4 inch diameter tubes provide lateral torsional stability. A typical section of this disposable structure is shown in Figures 2-34 and 2-35.

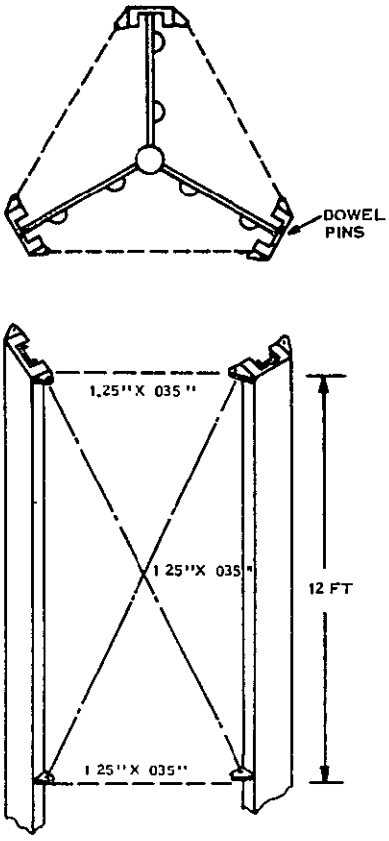

Figure 2-34. Triform Configuration, Typical Section with Stabilizing Bracing

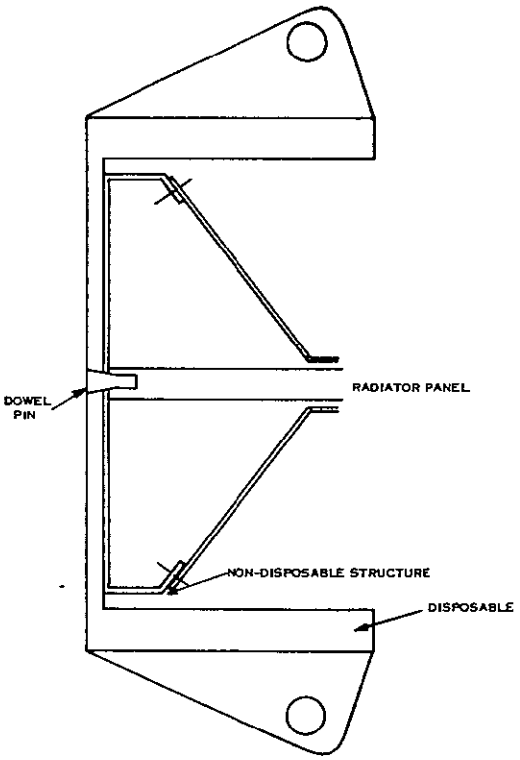

Figure 2-35. Triform Support Structure

The remaining structure, required to support the Stage II burnout loads, 4.0 g's axial and 0.67 g's lateral, consists of light channels permanently attached to the edges of the radiator.

In this appraisal, no methods of taking structural loads through a suitable reinforced flight fairing were considered. The flight fairing, at full diameter, offers the optimum bending moment of inertia per pound of material. However, reaching the load path would require that the payload and fairing diameters coincide or that load spreader members are included at suitably frequent intervals. It is not expected that a significantly lighter structural weight can be obtained by doubling up on the fairing; by using the separate structure, the analysis is simplified. An additional benefit of separate structure is that the payload is then acoustically isolated from the fairing; this is expected to be of significant advantage in the final design of small, poorly supported loads such as hoses and electrical leads.

Conclusions from this Structural Analysis include:

a. The fundamental frequency of the selected configuration should be calculated and compared with the booster requirements. It is anticipated that the resulting frequency will be on the order of one Hz which is below the current booster requirement of $\sim$ six Hz. The lower frequency can probably be accommodated by design changes in the booster autopilot

b. The effects of using aluminum in place of stainless steel for the disposable support structure of the triform designs should be analyzed. Stainless steel was chosen to eliminate differential thermal expansion. Since the MHD radiator is launched at low temperature, it may be possible to achieve attractive weight savings by using aluminum

c. The effects of locating the MHD generator and secondary radiator bay near the booster interface should be investigated.

2.5.4 CONFIGURATION CHOICE

The structural analysis preceding indicates that the triform radiator offers lower net weight than the conical radiator, so it will be used in the baseline design. The apparent success of the triform configuration here and its failure for the thermionic reactor spacecraft can be ascribed to the fact that the MHD radiator derives significant strength from the cesium vapor ducts. The conduction fin radiator in the thermionic reactor spacecraft uses many small tubes.

The configuration with the MHD bay located at the bottom of the radiator (No. 2) seems to offer significant structural weight savings, suggesting synthesis of a new configuration using a triform radiator with the MHD bay at the aft end. The attraction of this idea dims when one considers some of the problems and weights that were omitted from Configuration No. 2 in order to simplify its analysis. An estimate was made of the increase in lithium inventory, piping, and pumping that would accompany relocation of the MHD bay. If the reactor line size calculated for the baseline design were retained the pipe and coolant alone would increase in weight by approximately 1,000 pounds and the reactor line pressure drop would increase by approximately 30 psi. In addition, the lithium accumulator, the startup pump, etc. would have to increase in size. One can conclude, then, that relocation of the MHD bay to the aft end is possible but not attractive.

Configuration No. 4, therefore, was used as the basis for the baseline design arrangement.

2.6 BASELINE SYSTEM DESIGN

From the preceeding, the baseline MHD spacecraft design was developed. The baseline design cycle conditions are given in Figure 2-36, the fluid system schematic diagram is shown in Figure 2-37, and the spacecraft inboard profile is shown in Figure 2-38. Table 2-15 gives the weight summary and breakdown for the baseline design spacecraft. This section of the report discusses the baseline design first in general and then by individual equipment catagory.

2.6.1 ARRANGEMENT

The arrangement of the baseline design spacecraft is based on Configuration No. 4 discussed in Paragraph 2.5.3. The reactor and the payload are situated at opposite ends of the spacecraft to minimize shielding, the narrow angle radiation shield is located immediately beneath the reactor.

2.6.1.1 MHD Bay

The MHD power system equipment is located in a three-sided tapered bay (Figure 2-39) which extends from the bottom edges of the radiation shield; the surface panels of this bay and the surface panels of the radiation shield form continuous planes and provide sufficient area to reject the following heat loads to space:

a. Neutron and gamma heating of the shield

b. Dissipation losses from the excitation capacitors

c. Winding losses from the MHD generator

d. Heat transferred to the MHD generator stators from the MHD duct

e. Miscellaneous heat loads from MHD equipment such as pumps and valves.

The shield surfaces are used only for passive cooling of the shield itself. The MHD bay surface is divided into three major sections; the uppermost section is used for mounting the excitation capacitors. The middle section is devoted to the auxiliary radiator which rejects MHD generator winding losses; the average temperature of this radiator is about 340^{o}F. The lowest section of the bay surface is devoted to the auxiliary radiator which rejects heat from the MHD stators pumps and valve motors; the average temperature of

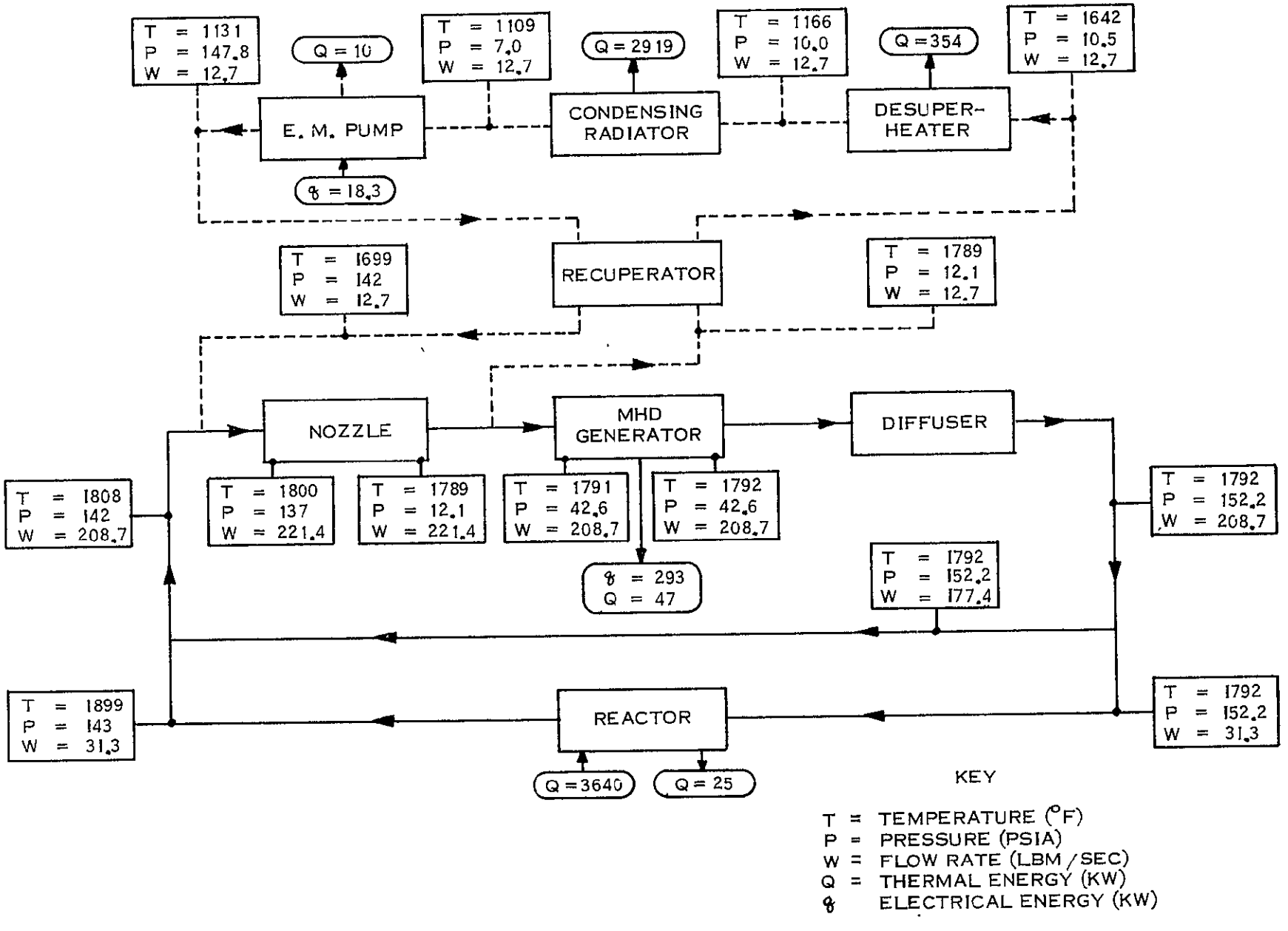

Figure 2-36. Cycle Conditions, MHD Power System Baseline Design

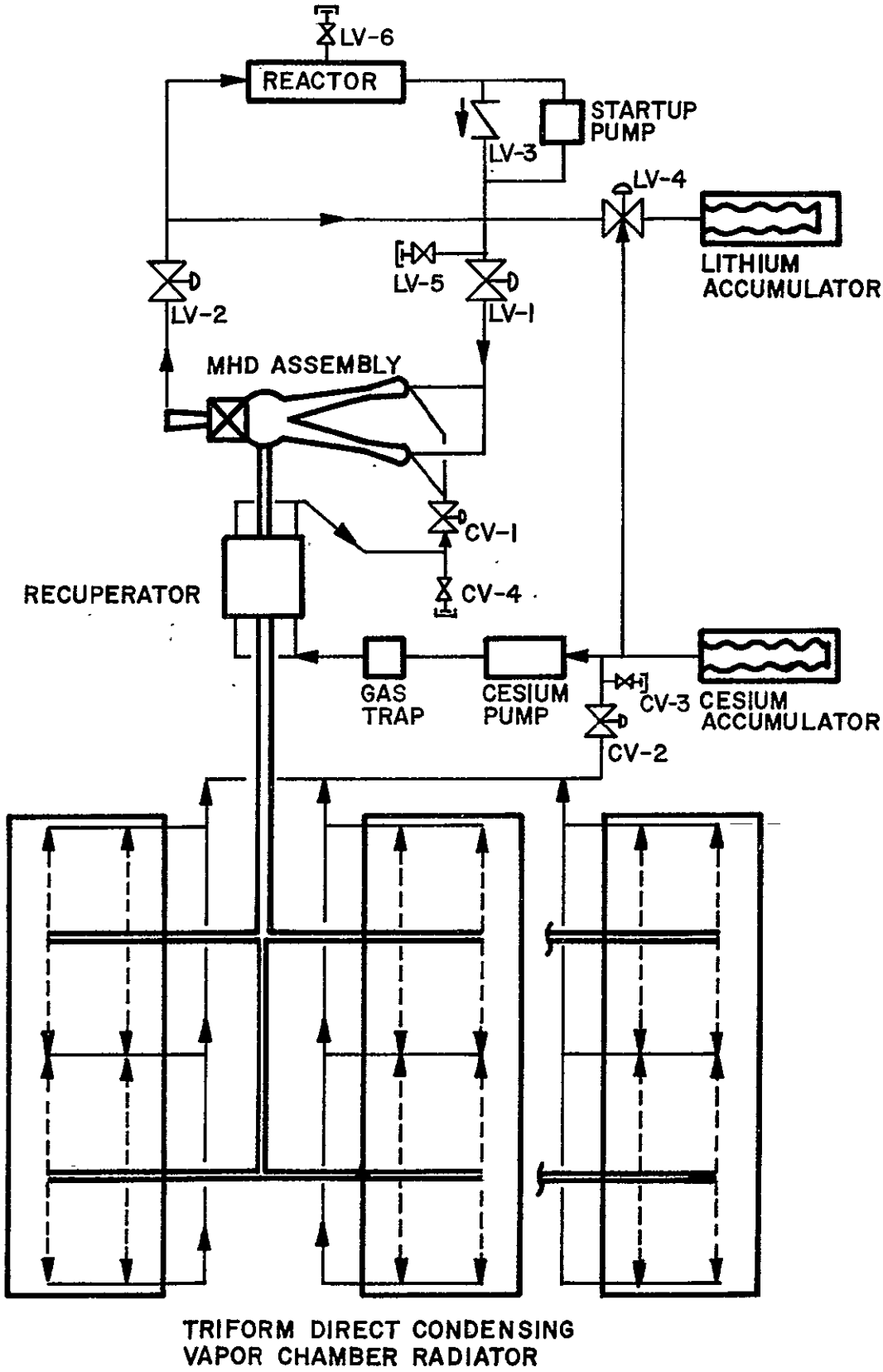

Figure 2-37. Fluid Schematic Diagram, MHD Power System

TABLE 2-15. MHD BASELINE SPACECRAFT WEIGHT SUMMARY

Component	Weight - Pounds				
Propulsion System					18,500
Power Plant Subsystem				15,810	
Reactor Subsystem			2190		
Reactor Dry		2070			
Actuators		120			
Shield			1470		
Neutron		1470			
Permanent Gamma		None			
Power Conversion			7510		
Lithium Loop		550			
Piping	210				
Accumulator	130				
Valves (5)	50				
Startup E. M. Pump (1)	10				
Fluid	150				
MHD Flow Assembly		850			
Inlet Headers (2)	70				
Mixers (2)	20				
Nozzles (2)	470				
Separator	90				
MHD Duct	50				
Diffuser	150				
MHD Generator		840			
Stator Fe (2)	180				
Windings	660				
Cesium Loop		2190			
Piping	720				
Accumulator	60				
Valves (4)	20				
EM Pump	840				
Gas Trap	10				
Recuperator	400				
Fluid	280				
Main Radiator		2940			
Vapor Panels	1790				
Ducts and Piping	960				
Insul. Bulkheads	170				
Auxiliary Radiator		200			
Piping	80				
Pumps	20				
Fin Panels	110				
Coolant	10				
Electrical Power & Control System			3350		
Excitation System		1390			
Capacitors	1240				
Cabling	150				
Main Power Cond.		1480			
Transformers	740				
Rectifiers	10				
Filters	220				
Distr. Cabling	160				
Ass'y Hardware, Control Logic, Etc,	410				
Hotel Load		170			
Power Condit.	100				
Radiator	20				
Distr. Cabling	50				
Power Plant Control		70			
Startup Batteries		240			
Structure			1300		
Reactor Support		60			
Neutron Shield (ext)		120			
MHD Bay Structure		660			
Shell	230				
Internal	30				
Insulation	410				
Radiator Structure		460			
Internal Truss	160				
Bay Bulkheads	80				
Permanent External	230				
Thruster Subsystem				2790	
Ion Engine Subsystem			1335		
Ion Engine Units		585			
TVC Unit		650			
Miscellaneous		100			
Power Cond. Electron.			580		
Special Ion Eng. PC		270			
Thruster Isolation		310			
Power Cond. Radiators			880		
HV Power Supply		770			
Special Ion Engine Units		70			
Thruster Isolation		50			
High Voltage Power Cables			30		
3100 Volt Cables		5			
250 Volt Cables		15			
Structure			85		
Special PC Bay		65			
Propellant System					14,730
Propellant				14600	
Tanks & Distr.				220	
Structure				10	
Net Spacecraft					2340
Guidance & Control				50	
Communications				60	
Science				2,065	
Radiator				25	
Structure				35	

Gross Spacecraft in Earth Orbit	35,670
Launch Vehicle Adapter	350
Launch Shroud Payload Weight Penalty (4400 lb fairing)	1,060
Disposable Structure Weight Penalty (2250 lb structure)	550
Launch Vehicle Payload Requirement	37,530

FOLDOUT FRAME 1

FOLDOUT FRAME 2

ITEM	DESCRIPTION
22	THERMAL BULKHEAD — FORWARD
23	CESIUM ACCUMULATOR
24	GAS TRAP
25	CONTROL GAS STORAGE TANK
26	LITHIUM ACCUMULATOR
27	HIGH TEMP. AUXILIARY RADIATOR
28	CESIUM PUMP
29	VALVE LV — 1
30	VALVE CV — 1
31	NOZZLE ASSEMBLY
32	RECUPERATOR
33	VALVE LV — 4
34	LOW TEMP. AUXILIARY RADIATOR
35	SEPARATOR
36	MHD GENERATOR
37	EXCITATION CAPACITOR BAY
38	VALVE LV — 2
39	BATTERIES
40	START UP PUMP
41	SHIELD ASSEMBLY
42	REACTOR OUTLET LINES
43	REACTOR INLET LINES
44	ACTUATORS
45	REACTOR
46	HEATING JACKET INLET
47	VALVE LV — 6

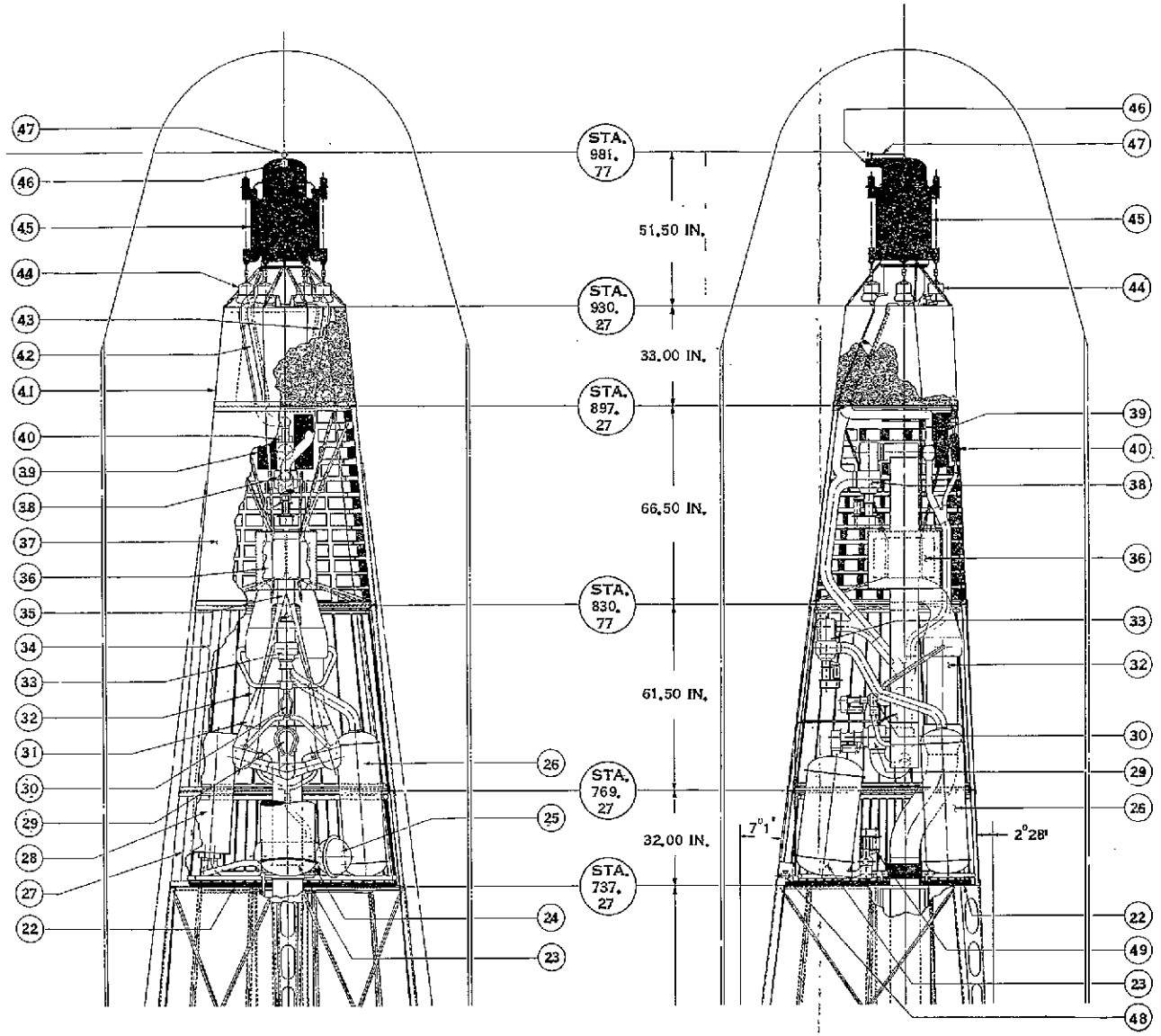

Figure 2-39. MHD Bay Arrangement

FOLDOUT FRAME 1

FOLDOUT FRAME 2

this radiator is about 800°F. In addition, the surfaces of the MHD bay provide mounting, heat rejection, or access area from the following auxiliary equipment:

a. Two startup battery sets (one for the lithium startup flow and one for auxiliary cooling startup flow)

b. Storage tank and regulators for control gas used to pressurize lithium and cesium accumulators

c. Valves for evacuating, filling and draining the lithium and cesium systems

To prevent excessive backheating of the excitation capacitors, batteries, gas tank, and auxiliary radiators, the ~1800°F nozzle assembly and fluid equipment in the MHD bay is enveloped in a teepee-shaped envelope of multifoil insulation sized to hold heat leakage to approximately 20 watts per square foot at normal operating temperatures. The use of this overall insulation wrap eliminates the need for insulation on any of the individual pipes and equipment except the reactor and its feed and return lines connecting it to the MHD bay. The MHD bay insulation also runs across the bottom face of the MHD bay to prevent thermal interference with radiator operation. The multifoil insulation and skin of the MHD bay provides micrometeoroid impact protection for equipment in the bay.

The MHD nozzle assembly is arranged vertically in the bay and attached to the MHD stator blocks which are suspended on tubular trusses from the outside structure of the MHD bay at the shield interface. In this way, by making the basic structural attachments of both ends of the nozzle assembly to the stator blocks, the delicate MHD duct between the stator blocks is isolated from loads and given maximum support. Lateral supports at the stator blocks and at the nozzle inlets restrain the entire assembly. The structural supports for the MHD generator and nozzle assembly are assumed to be simple tubular trusses; no attempt was made to isolate vibrations induced by the high velocity two-phase flow in the nozzles.

The pressure recovery or lithium-pumping diffuser is mounted in the upper center of the MHD bay with its outlet line feeding through an isolation valve (LV-2) and branching into the reactor inlet line leaving the bay and the bypass line which swings down toward the inlet end of the nozzle assembly. The reactor return line enters high in the MHD bay and, feeding through a check valve (LV-3), combines with the bypass line to supply the lithium flow to the nozzles. A small dc electromagnetic pump is connected in bypass around the check valve,

mounted at the surface of the MHD bay adjacent to the batteries which power it. This pump is used to circulate lithium through the reactor and the bypass line for system warmup.

The cesium condensate enters the MHD bay near the center of the bottom panel, three return pipes feeding a ring header. Flow from the header goes to the cesium pump, through the gas trap, and branches to feed cesium through the recuperator to the nozzle inlets. The two cesium lines between the recuperator and the nozzles are recombined briefly in order to use only one isolation valve in that location (CV-1). The other cesium isolation valve (CV-2) is located between the ring header and the pump suction.

The accumulators and the cesium pump are mounted to the outer shell of the MHD bay. The insulation envelope includes the accumulators, permitting them to be warmed up by the startup flow in the lithium bypass line. One arrangement fault which is still carried in the MHD bay design is that the lithium accumulator is mounted upside down, with its outlet pipe pointed toward the reactor. This means that the accumulator, once filled, cannot be drained. The most that could be done would be to maintain the lithium molten by circulating hot gas around the accumulator bellows. In a final spacecraft design, this accumulator should be inverted and the piping rerouted.

2.6.1.2 Radiator Assembly

The main radiator assembly is shown in Figure 2-38 and in section in Figure 2-40. The radiator is divided into four bays of equal area three of which are made up with rectangular panels a little less than 13 feet tall. The fourth and uppermost bay is somewhat taller, its greater height needed to compensate for the diagonal breakback of the panel's outer edge which is necessary to stay within the shield shadow. This shield angle was chosen as the one which resulted in minimum shield weight.

If the radiator bays are numbered 1 to 4 from top to bottom, the vapor inlets are located at the bottom of bays 1 and 3 and the tops of bays 2 and 4. Conversely, the condensate outlets are at the tops of bays 1 and 3 and the bottom of bays 2 and 4. In this way, during warmup or at operating temperature, the material in any plane normal to the spacecraft axis will be essentially isothermal and thermal stresses will be minimized. The vapor feed duct runs down inside the central truss, 10-inch diameter to the bottom of bay 1, and 8.5-inch diameter from there to the bottom of bay 3. There are three condensate return lines, one running inside each corner of the central truss.

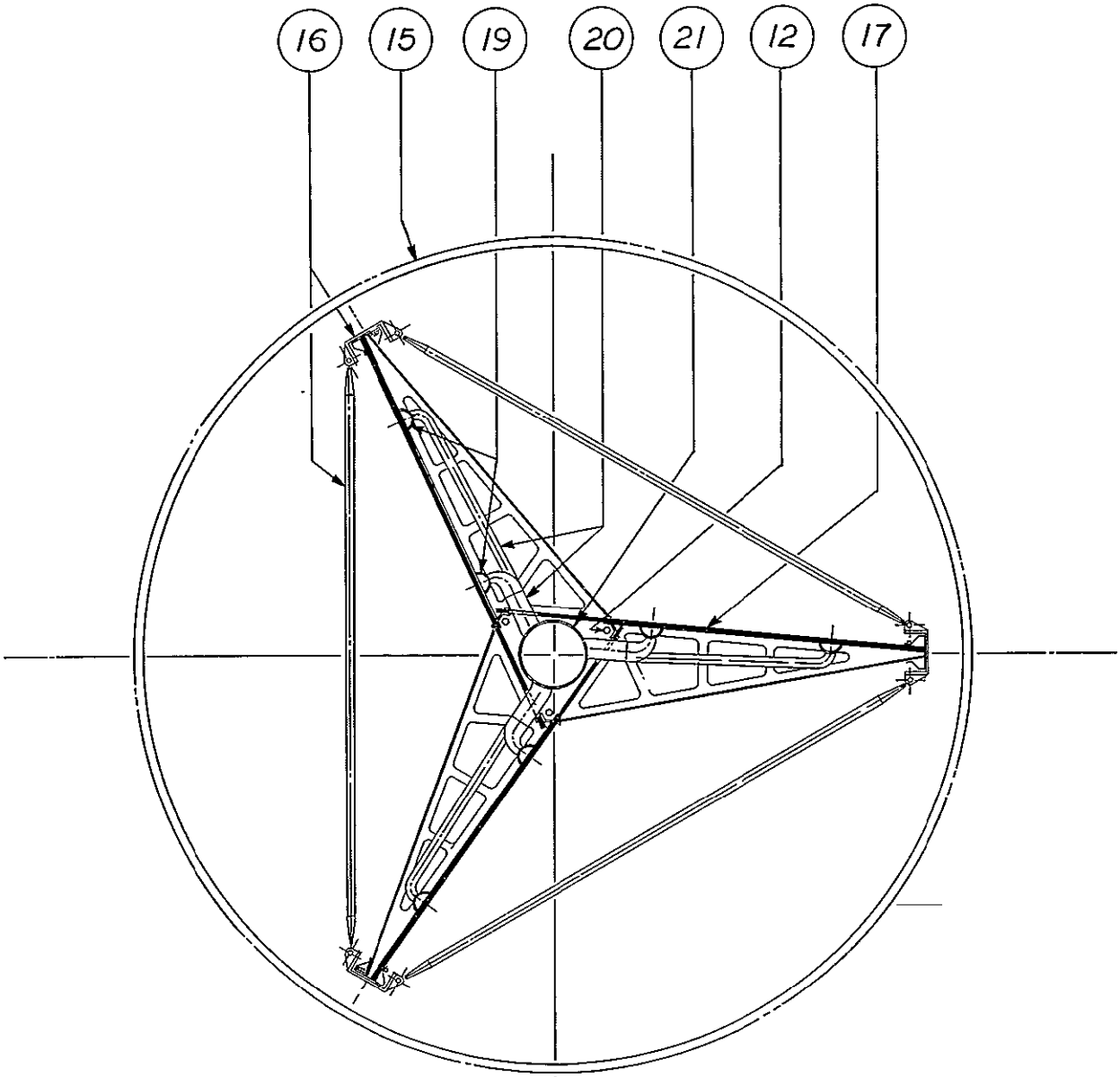

ITEM	DESCRIPTION
12	CESIUM RETURN LINES
15	FLIGHT FAIRING
16	DISPOSABLE LAUNCH SUPPORT STRUCTURE
17	VAPOR CHAMBER PANEL — 12
19	CESIUM CONDENSING DUCT — 24
20	CESIUM VAPOR HEADERS
21	CESIUM VAPOR FEED DUCT

Figure 2-40. Main Radiator Assembly (Section)

The vapor chamber panels, each with two vertical condensing ducts, are mounted individually on studs protruding from the central truss. Of course, that area of the panel which overlaps the central truss does not view space and, consequently, rejects no heat. This configuration was chosen for three main reasons. First, the overlapping triangle center gives each panel an exposed radiating area equal to that it would have if it could run on a true radius line right to the spacecraft centerline; this keeps the radiator length to a minimum by maximizing radiating area per unit length. Secondly, this arrangement eliminates the need for separate micrometeoroid armor for the long vapor feed and condensate return lines, the radiator panels and trusswork serving instead. Third, this arrangement facilitates field assembly and test; individual panels can be shop fabricated and tested. They are assembled by bolting to the central truss and making field welds at the vapor and condensate headers. With the exception of the tapered panels in the top bay, all panels are identical and interchangeable; the three top panels are identical.

2.6.1.3 Spacecraft Lower Assembly

The spacecraft lower assembly is a compound cylindrical section which contains, in descending order, the main power transformers and rectifiers, the science and communications equipment, and the thruster system. The propellant is stored in two saddle tanks in this bay, and the deployable main antenna is tucked under the thrusters within the perimeter of the launch vehicle payload adapter. After reaching earth orbit, the adapter is jettisoned and the antenna moves out to one side clearing the thrusters.

The single phase transformers and rectifiers which are used to convert the output of each MHD generator phase were mounted here rather than in the MHD bay to minimize the weight near the top of the spacecraft, to enjoy the cooler environment of the lower assembly and to keep the rectifiers in a lower radiation environment for added reliability. This choice relies on the fact that high slot voltage (700 to 950 volts) permits separate connection for each slot to run the full length of the radiator without severe cable weight penalty. The cables are radiatively cooled, running in wireways in the permanent structures at the outside edges of the radiator panels.

2.6.2 REACTOR AND SHIELD DESIGN

2.6.2.1 Reactor

The MHD power system requires a nuclear reactor heat source which can operate with coolant outlet temperatures ranging from 1600 to 2200°F. If possible, the reactor should be lithium-cooled in order that there is at least an option to use the reactor coolant directly in the MHD cycle. Since no reactors of this type are under active development at present, it is important to base MHD reactor parameter estimates on reactor development work which has been done. The following reactor design characteristics were generated on the basis of the PWAR-20 SNAP-50 design of 2.2 MW output (Reference 13). These characteristics are considered representative for an MHD reactor with minimum development time and risk. Extrapolations to other power levels and temperatures are based on data in Reference 14. Size extrapolation assumes that core size grows only in diameter and not in length, with core sectional area proportional to power. This assumption will give a conservative shield size estimate. The reactor design characteristics are listed in Table 2-16. Figures 2-41 and 2-42 show the size and weight variation with output power and Figure 2-43 shows an elevation view of the baseline design (3.64 MW) reactor and shield.

TABLE 2-16. MHD REACTOR DESIGN CHARACTERISTICS

Reactor Type (spectrum)	Fast
Design Life (full power hours)	20,000
Fuel	95% dense UC/UN
Coolant	Lithium
Coolant Outlet Temperature	Nominal 2000°F Range 1700 to 2300°F
Inlet to Outlet Coolant Temperature Difference	Nominal 100°F Range 75 to 125°F
Reactor Coolant Pressure Drop	Nominal 10 psi
Reactor Coolant Inlet Pressure	Nominal 53 psi*

* Higher as necessary to suit MHD cycle conditions.

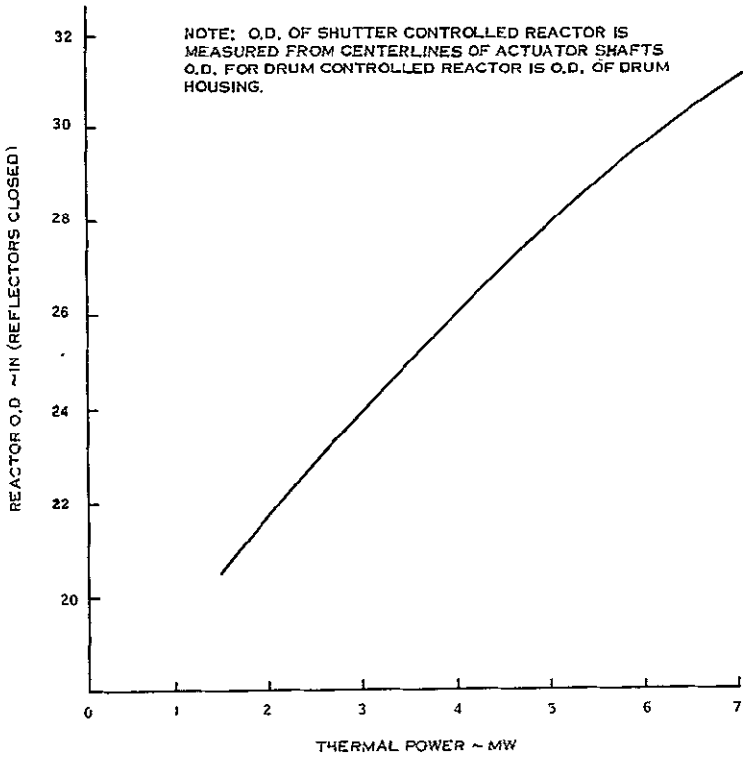

Figure 2-41. MHD Reactor Diameter

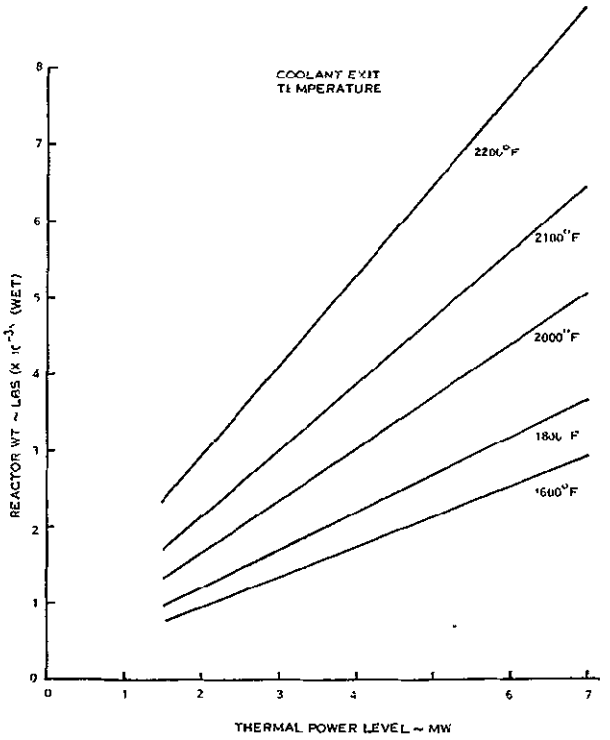

Figure 2-42. MHD Reactor Weight

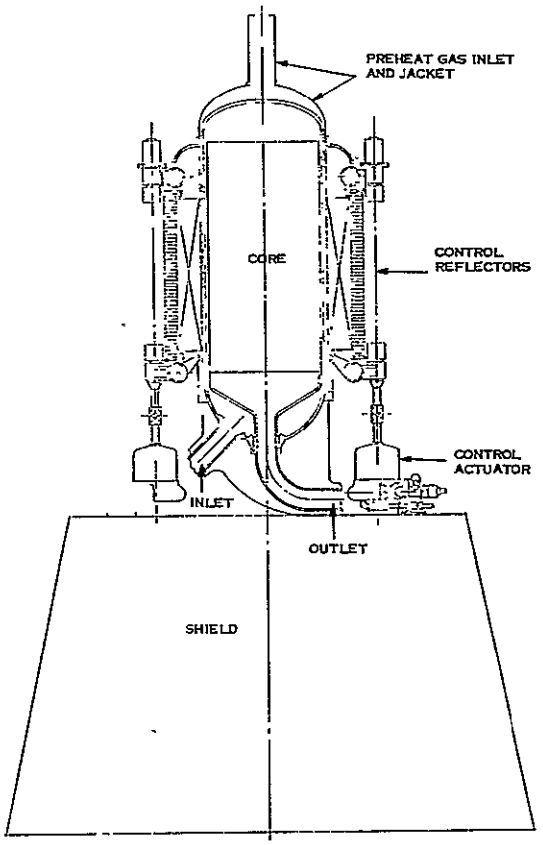

Figure 2-43. MHD Reactor and Shield

The reactor shown in Figure 2-43 uses six reflector shutters for control. The control drive shown in Figure 2-43 and in detail in Figure 2-44 is based on a nutating gear drive which may be used with a liquid-cooled drum control system and derives from a hydrogen flow control valve actuator which was designed by Bendix Corporation Aerospace Division for NASA in the NERVA program (Reference 15). This control drive actuator can be liquid cooled through the connections provided. This actuator can be used for a compact configuration. If desired, a more conventional drive could be installed below the shield with extension shafts running through the shield to the control reflectors. The actuator design could then be simpler but weight would probably be greater and the drives might occupy space below the shield which is desired for MHD equipment.

2.6.2.2 Shield

The radiation shield used in the baseline design is a lithium hydride neutron shield. A 3.5 percent volume fraction of the shield is assumed to be stainless steel containment and support structure, giving the shield an average density of 0.0365 lb/in.^{3} (assuming

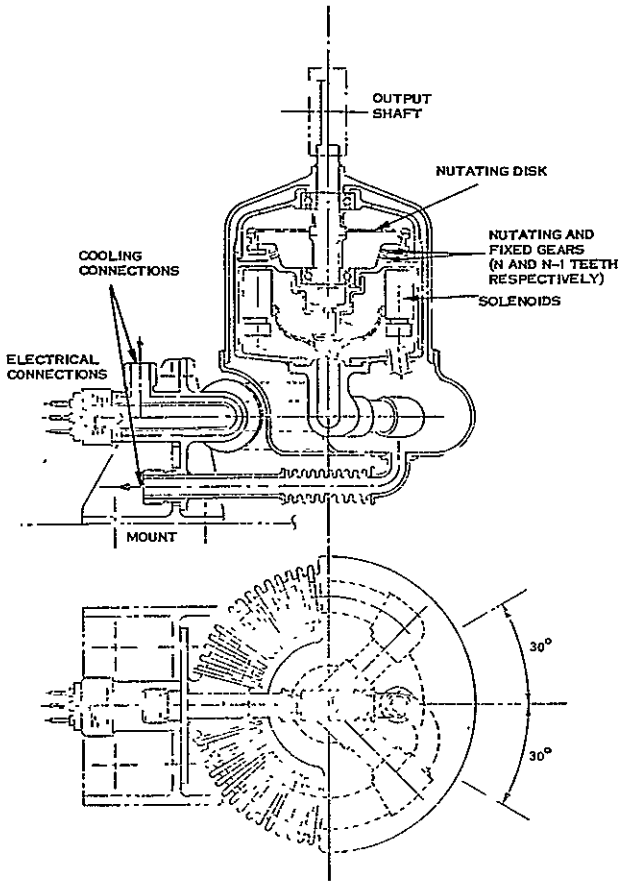

Figure 2-44. MHD Reactor Control Actuator

a specific gravity of 0.78 for cast LiH). An additional 1/16 inch canning plate is allowed for the outside surface of the shield to assist in heat dissipation and to enhance resistance to micrometeorite puncture.

The 33-inch shield thickness is based on a conservative extrapolation of shield analysis reported in Reference 13; this same analysis and extrapolation indicates that no gamma shield is necessary. The radiation shield is assumed to be passively cooled, operating at a temperature of less than 1000°F. Shield heating rate estimates made in Reference 16 (See Figure 2-45) were made for the in-core thermionic reactor. The MHD reactor would have a harder flux spectrum but these heating rates are considered usable for estimating purposes. These heating rates indicate that a small shadow shield such as is used here would generate only about one kW of combined neutron and gamma heat. With ~ 30 square feet of surface area viewing space, the shield can easily reject many times this much heat.

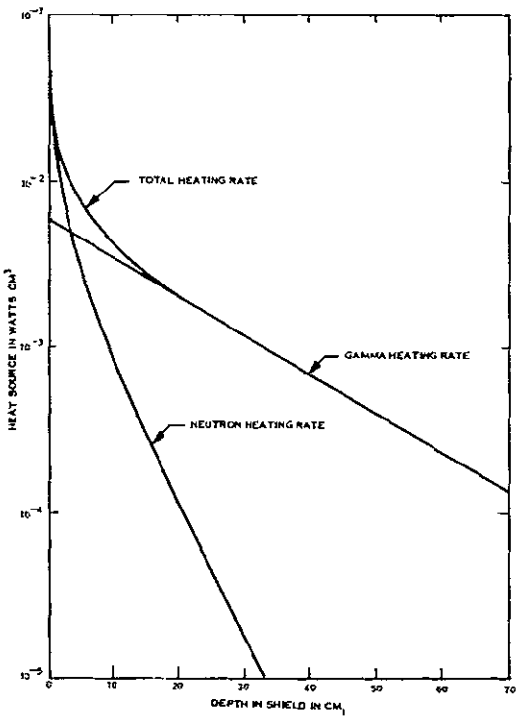

Figure 2-45. Shield Heating Rates

2.6.3 MHD EQUIPMENT

In this section on MHD equipment, we address ourselves to the design aspects of two major pieces of equipment, the MHD generator and the MHD nozzle assembly, and the valves, pumps, etc., which make up the rest of the MHD equipment.

2.6.3.1 MHD Generator

2.6.3.1.1 Generator Design - The MHD generator in the baseline system consists of two laminated iron stator blocks with a wide, shallow lithium slow passage between them. The stator laminations run in the direction of flow, perpendicular to the broad side of the flow passage. The stator blocks are fitted with 25 copper-winding (50 turns each) coils which run through slots in the stators normal to the laminations with each coil loop completed by coming over the outside face of the stator block, opposite the flow passage (see Figure 2-46). As the numbering in Figure 2-46 indicates, the coils are numbered and designated as slots serving various sections of the generator duct. Slots 0 and 22 have two coils each and serve the upstream and downstream compensating poles, as well as the first and last

121

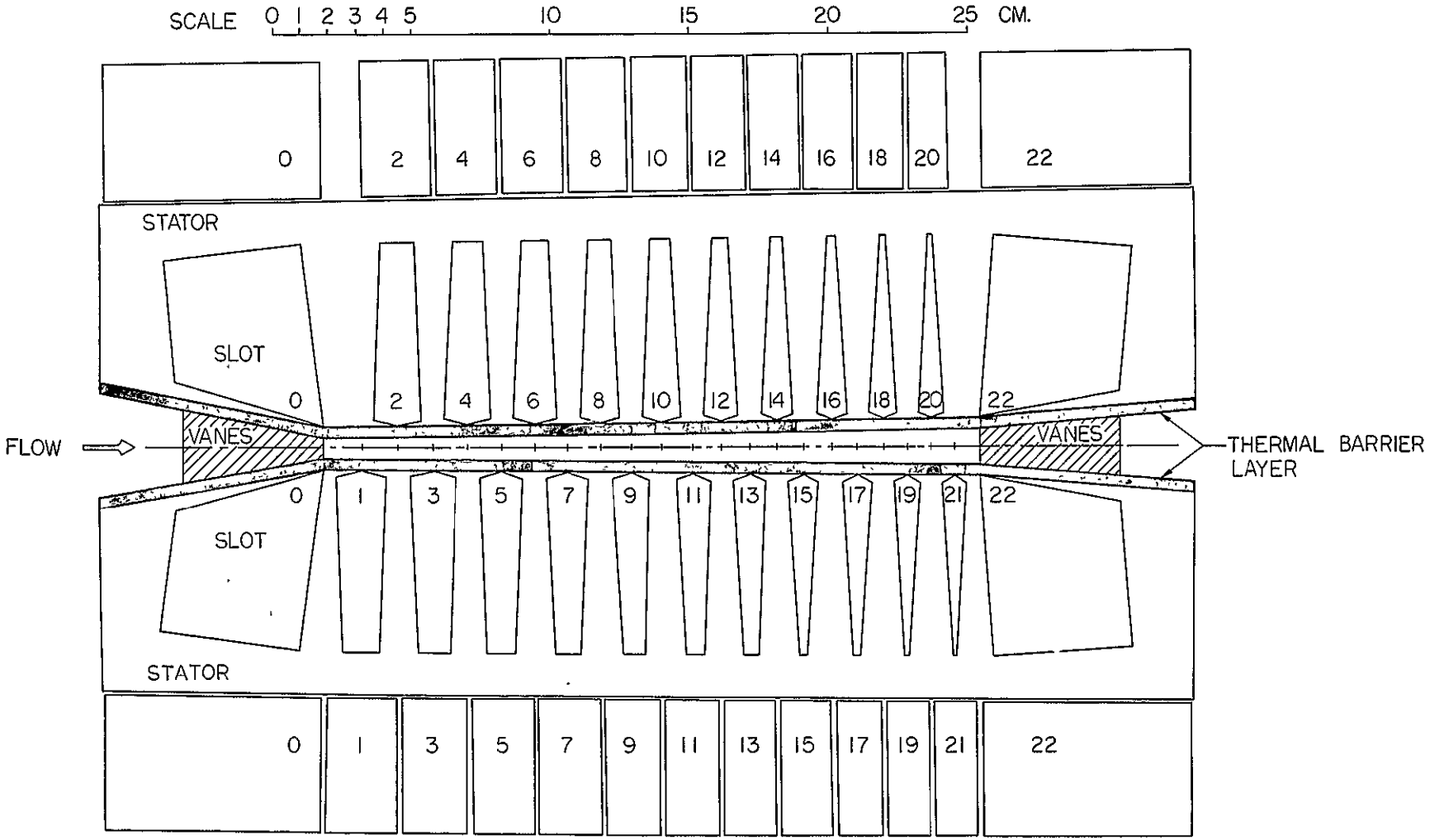

Figure 2-46. Baseline Design MHD Generator

segments of the travelling wave region. Table 2-17 lists each slot, the location of its pole piece with respect to the travelling wave region of the generator, and the slot widths. Table 2-18 lists the slip, fluid velocity, field velocity and field intensity at each slot point; Table 2-19 lists the major energy quantities received or generated in each sector/slot, the kinetic energy input, $\frac{\dot{m}}{2}(V_i^2 - V_o^2)$, the winding loss ($I^2R$), the net usable power generated in the winding and the reactive power of the winding. Note that the first coil of the generator (slot 0) has negative net power, requiring the input of 81.31 kWe of power, and that the last coil (slot 22) generates 138.15 kWe, almost half of the net power produced by the entire generator. This is characteristic of a linear generator of this type, the large powers demanded at the inlet and generated at the exit are due to the abrupt establishment and termination of the machines magnetic field. This power generation asymmetry almost demands that slots 0 and 22 be wired together. Fortunately, these two slots are almost in phase with one another and are wired together with some additional phase correcting capacitance (see Paragraph 2.6.6). An additional advantage can be taken of the way the MHD generator produces power. Slots 0 and 22 are obviously vital, but the other slots produce only small amounts of power (between 1 and 7 percent). If vital auxiliaries are powered by slot 22, then an open-circuit failure of one of the other slots would not have a significant effect on power output, if the power conditioning system is not seriously perturbed by the input change. This is, in fact, one of the reasons for choosing the baseline design power conditioning system (again, see Paragraph 2.6.6).

The generator stator material is assumed to be Hyperco 27, saturating at about 2 Tesla ($\sim$ 130,000 lines/in.^{2}); there might be some advantage in using Hyperco 50 which saturates at about 2.4 Tesla. The winding material in the MHD generator is assumed to be copper with no cladding of any kind. In high temperature winding systems of this sort, it is usually advantageous to use silver conductors and, whether silver or copper, the conductors should be clad with a protective layer of nickel or Inconel to prevent diffusion of conductor material through the insulation at temperature. The baseline design calculations are based on the assumption that 80 percent of the slot cross-sectional area is occupied by conductor material. The inclusion of cladding material and heavier insulation may reduce this conductor area fraction to as little as 50 percent (see paragraph 2.6.3.1.3).

TABLE 2-17. BASELINE DESIGN MHD GENERATOR DIMENSIONS

Slot No.	Distance From Beginning Of Travelling Wave Region (CM)	Flow Channel Height At Slot Pole Piece (CM)	Width of Slot At Widest Point Near Point Piece (CM)	Width of Slot At Narrowest Point, Opposite Pole Piece (CM)
0	0.00	0.754	5.021	5.021
1	1.33	0.774	1.742	1.276
2	2.63	0.795	1.692	1.215
3	3.91	0.016	1.642	1.153
4	5.17	0.837	1.592	1.090
5	6.39	0.859	1.542	1.026
6	7.60	0.882	1.492	0.961
7	8.77	0.905	1.442	0.895
8	9.92	0.928	1.394	0.830
9	11.05	0.952	1.345	0.763
10	12.15	0.977	1.297	0.697
11	13.22	1.002	1.250	0.630
12	14.28	1.028	1.204	0.564
13	15.30	1.054	1.158	0.498
14	16.30	1.081	1.114	0.433
15	17.28	1.108	1.070	0.369
16	18.24	1.136	1.027	0.307
17	19.17	1.165	0.985	0.248
18	20.08	1.194	0.944	0.191
19	20.97	1.224	0.904	0.138
20	21.84	1.254	0.865	0.091
21	22.69	1.286	0.827	0.052
22	23.57	1.320	5.021	5.021

Slot Depth = 6.58 cm
Wall Thickness (Stator-To-Fluid) = 0.4 cm
Li Channel Width = 25.1 cm

Compensating Pole	Length (cm)	Duct Average Height (cm)	No. of Vanes
Upstream	5.02	1.73	18
Downstream	5.02	1.66	28

TABLE 2-18. BASELINE DESIGN MHD GENERATOR DYNAMIC CHARACTERISTICS

Slot No.	Slip	Fluid Velocity (M/sec)	Wave Velocity (M/sec)	Field Strength (TESLA)
0	0.212	114.4	94.4	0.470
1	0.203	111.4	92.6	0.479
2	0.194	108.6	90.9	0.488
3	0.186	105.8	89.2	0.497
4	0.178	103.0	87.5	0.507
5	0.170	100.4	85.8	0.517
6	0.163	97.8	84.1	0.527
7	0.156	95.4	82.5	0.538
8	0.149	92.9	80.9	0.549
9	0.143	90.6	79.3	0.560
10	0.136	88.3	77.7	0.571
11	0.130	86.1	76.2	0.583
12	0.125	83.9	74.6	0.594
13	0.119	81.8	73.1	0.607
14	0.114	79.8	71.7	0.619
15	0.109	77.8	70.2	0.632
16	0.104	75.9	68.8	0.645
17	0.100	74.1	67.4	0.659
18	0.095	72.2	66.0	0.673
19	0.091	70.5	64.6	0.687
20	0.087	68.8	63.3	0.701
21	0.083	67.1	62.0	0.716
22	0.079	65.4	60.6	0.732

TABLE 2-19. BASELINE DESIGN MHD GENERATOR, POWER SUMMARY

Sector	Input Power (Kinetic Energy) (KW)	Winding Loss (KW)	Net Power (KW)	Reactive Power (KVA)
0	16.08	0.59	-81.31	151.8
1	30.72	0.22	18.51	51.4
2	29.10	0.23	17.72	51.1
3	27.56	0.24	16.94	50.9
4	26.10	0.25	16.17	50.7
5	24.71	0.26	15.41	50.6
6	23.39	0.28	14.66	50.5
7	22.14	0.29	13.92	50.4
8	20.97	0.31	13.21	50.3
9	19.86	0.33	12.50	50.3
10	18.80	0.36	11.80	50.3
11	17.80	0.39	11.12	50.4
12	16.86	0.42	10.46	50.4
13	15.97	0.46	9.80	50.5
14	15.13	0.51	9.16	50.6
15	14.34	0.56	8.53	50.7
16	13.59	0.63	7.91	50.9
17	12.89	0.71	7.29	51.1
18	12.22	0.80	6.67	51.3
19	11.59	0.92	6.05	51.5
20	11.00	1.07	5.41	51.7
21	10.44	1.26	4.75	52.0
22	5.72	1.05	138.15	190.7
Total	416.96	12.14	294.84	1410.2

2.6.3.1.2 Generator Cooling - The MHD generator stator iron and the coils must be protected from the high temperature of the lithium stream. The stator iron must be kept well below its Curie temperature ($\sim 1400^{\circ}F$) to maintain magnetic permeability; the copper coils should be held at a temperature low enough to keep the copper's resistance, and therefore the coil losses, at an acceptable level. Consideration was given at first to the use of cooling pipes running through the back iron of the stator blocks as shown in Figure 2-47. This technique is not attractive because analysis showed a stator temperature gradient of about $800^{\circ}F$ between the channel wall and the cooling pipes, including transfer of coil losses into the stator. Cooling the coils independently reduces this gradient to $700^{\circ}F$, still an unacceptable value. Figure 2-48 shows a second alternative considered. The section shown in this figure is taken at one side of the lithium channel looking in the direction of flow. Heat transfer from the lithium to the stator is retarded by the ceramic plate and a vacuum gap provided by a layer of ceramic microspheres; then a thin layer of ducts carrying NaK coolant, lying between the ceramics and the stator, remove the heat that does come through. The coolant ducts are small and separated from one another by strips of electrical insulation to prevent the generation of transverse eddy currents. Analysis showed these small ducts to be an attractive way to cool the stator iron but not effective for cooling the windings. With NaK coolant and heat loads in the realm of 25 to 50 kW, the size of these cooling ducts is limited by fabrication capabilities; pressure drop and pumping power are very small. The slotted wall and ceramic layer, proposed in Reference 17, is assumed to be sufficient in limiting heat load to 35 kW (2 sides) if the back side is $\sim 800^{\circ}F$. The 0.10 inch ducts shown in Figure 2-48 are more than adequate for removing this heat; for the baseline design the combined layer was assumed to be not 0.200 inches, but 0.158 inches (4 mm) for purpose of calculation. The effect of the thickness of this layer on generator performance is discussed in Paragraph 2.3.2.1.3.

To remove the winding loss heat, a finned aluminum winding loom with stainless steel NaK coolant passages is used to cool the external run of each coil. This loom and the cooling analysis are discussed in Paragraph 2.3.2.3.3, and depicted in Figure 2-14.

2.6.3.1.3 MHD Generator Design Problems - An appraisal of the MHD generator design reveals a number of areas where serious development problems exist or where modification of analytical assumptions or methods should be considered.

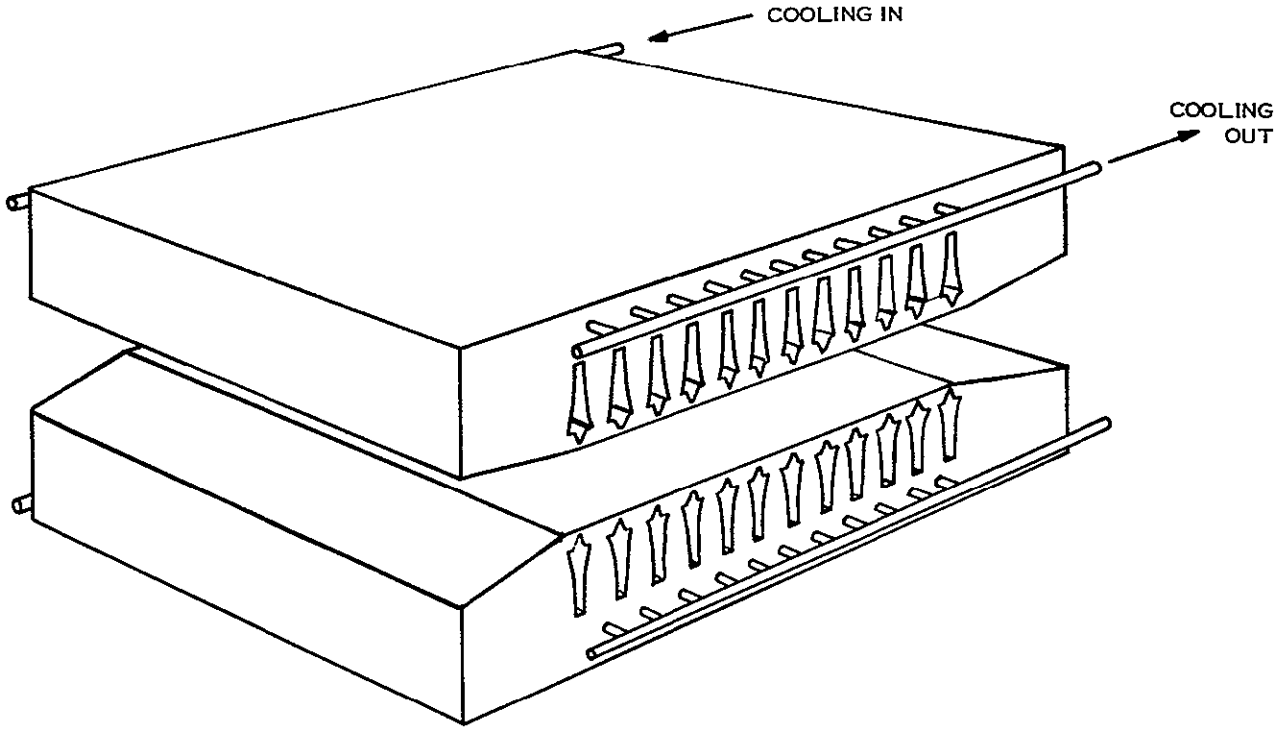

Figure 2-47. Cooling Pipes in MHD Stator Block

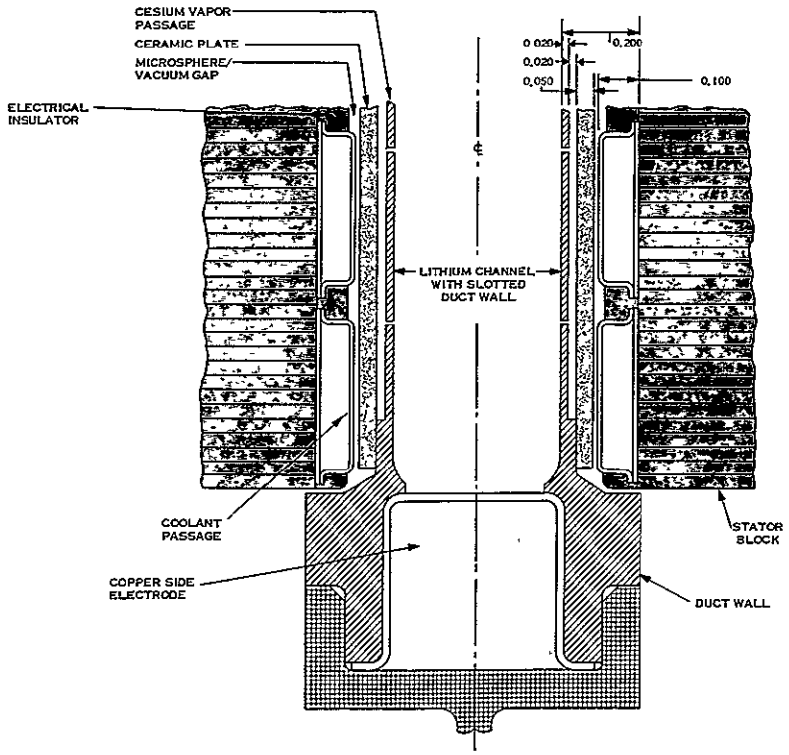

Figure 2-48. MHD Stator Cooling Passages at Lithium Duct Face

A. Can Loss - In order to assess the degree of need for a nonconducting or at least segmented duct, an approximate calculation was made for the duct loss assuming a 0.060 inch refractory metal duct. Duct loss is given by (Reference 18 and 19) the following formula for a moving field of amplitude B lines/in.^{2} with a wave velocity of V_R in./sec. The duct electrical resistivity (ohm-in.) is ρ.

$$\frac{\text{Loss (kW)}}{\text{in.}^3 \text{ duct wall}} = V_R^2 B^2 \times \frac{12.5}{\rho} \times 10^{-20}$$

Taking B = 38,400 lines/in.^{2} (0.607T) and V_R = 2880 in./sec (73.1 m/sec) corresponding to values given at slot No. 13 near the center of the duct. The loss per unit duct volume is ($\rho = 20 \times 10^{-6}$ ohm-in.) 75 kW/in.^{3}.

For a duct wall volume of approximately 12 in.^{3} (2 x 10 in. x 10 in. x 0.06 in.) the total loss is of the order of 900 kW. This result is of course meaningless in the sense that the electromagnetic effect of such large duct wall currents would greatly increase the winding load current and would completely invalidate the present design. The result is only shown to emphasize the absolute need for a nonconducting, (or at least segmented) duct. The use of a refractory metal duct in the manner of current state of the art induction type EM pumps, which operate at duct flux density levels approximately 1/4 that of this design and at field wave velocities approximately 1/6 of that used here, is completely out of the question.

B. Core Loss. The core loss has been approximately evaluated with the use of experimental data for total core loss (eddy current plus hysteresis) in watts per pound for Hyperco 27 0.004 inch thick laminations as a function of flux density and frequency. At a frequency of 300 Hz, 20,000 gauss (2T) the core loss is of the order of 20 watts per pound. This corresponds to 3600 watts for the 180 pound core. This loss is small (but not negligible) compared to the I^2R loss in the windings. The temperature difference involved in conducting this loss through a Hyperco 27 stator is of the order of 150°F assuming the core is cooled at the back. It may be noted, however, that 0.9 is a more realistic value of stacking factor for flame sprayed alumina interlaminar insulation type cores with 0.004 inch laminations.

C. Winding Loss. It has been found that large errors result from the calculation of the winding loss on the basis of applying an average current density and average ac/dc resistance (Rac/Rdc) ratio, and an average space factor over the entire slot cross section. The reasons for this are the following:

1. The presence of a slotliner ground insulator, of turn to turn insulation, and of low conductivity nickel or Inconel coating in the silver (or copper) conductors affects the effective available conducting cross section of the various conductors stacked in the tapered slot quite non-uniformly. This causes inequality of the current density in slot conductors, at least with the present slot dimensions.

2. Since the slot leakage field flux density varies greatly from the top to bottom of the slot, the conductor eddy current density and the Rac/Rdc ratio also vary greatly. Formulae for this effect available in the literature cover only the case of a constant width slot. The average value of the Rac/Rdc ratio for 50 series conductors approximately 1.13 mm thick at 300 cps (silver at 700°F) is approximately 1.4, but the ratio varies from essentially 1.0 for the bottom conductor to 2.2 for the top conductor (near the open end of the slot) (Reference 20).

The following conclusions can be stated:

1. A 20 to 30 mil thick ceramic slot liner (smaller thicknesses being mechanically impractical), combined with wrap-around E or S glass serving turn to turn insulation, combined with several mils of nickel or Inconel coating results in prohibitively high current densities in the conductors placed near the bottom of the narrow slots. The design must be modified to widen some of the slots at the narrow end.

2. In conjunction with wider slots at the narrow end, design for non-uniform conductor thickness may be advantageous. The effect of thickness on Rac/Rdc loss ratio is much smaller at the slot bottom than at the top. This would tend to equalize current density and loss per unit volume.

3. The winding loss calculation portion of the generator design computer program might be modified to calculate current density and Rac/Rdc ratio for each individual conductor, taking into account the effects of varying conductor dimensions, leakage field flux density, and variation of temperature. This could be done in conjunction with a somewhat detailed design selection of the conductor and slot insulation system.

D. Winding Heat Transfer. Because of extremely high current density in some of the slot conductors (region of the narrow end of slots 18 through 21) the conductor cooling mode based on heat conduction along the conductors in the slot portion to a cooled, out-of-stack region of the conductors is not adequate in this portion of the winding. Also, even the wide

region of these same slots is somewhat marginal with respect to hot spot to coolant ΔT because of the high Rac/Rdc ratio prevailing locally near the open end of the slots. As stated above, it is essential to reduce the peak local current density in some of the slots. Also, it appears that a more detailed calculation procedure for conductor temperature distribution is necessary. This procedure should account for intra conductor heat transfer across turn to turn insulation and associated interface thermal resistances and also for heat transfer into the stack across the slot insulator and associated interfacial thermal resistances. Some data is available (Reference 21) in the magnitude of such interfacial thermal resistances under vacuum conditions.

2.6.3.2 MHD Nozzle Assembly

One key problem was investigated in the design of the MHD nozzle assembly, how to prevent unacceptable distortion of the nozzle geometry due to creep effects. The baseline system uses a nozzle with a very wide and shallow bore, 9 to 10 inches wide and only about an inch high in the throat. Made of Cb-1Zr and operating at $\sim 1800^{\circ}$F for 10 to 20,000 hours, internal pressure can distort this rectangular flow passage to an elliptical shape. The pressure profile can be considered roughly the same as that reported in Reference 22 and illustrated in Figure 2-49. A calculation of design stresses and material thickness requirements was made using the nozzle geometry shown in Figure 2-50. It was assumed that the limit of acceptable distortion would be a 5 percent increase in the flow passage width or height, d

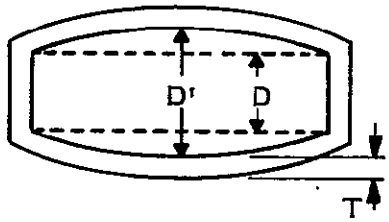

$d' \leq 1.05\,d$

Thus, the beam (side) deflection, y, is 2.5 percent of the passage dimension, and the strain, ϵ, is

$$\epsilon = \frac{32C}{\ell^2}\, y = \frac{16t}{\ell^2}\, y$$

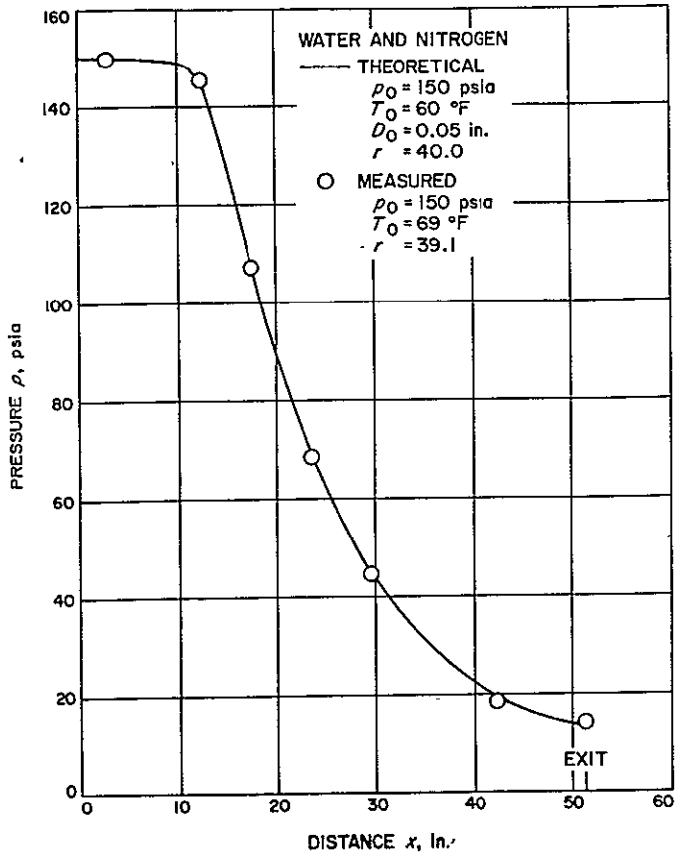

Figure 2-49. Comparison of Theoretical and Experimental Pressure Profiles in a Two Phase Nozzle

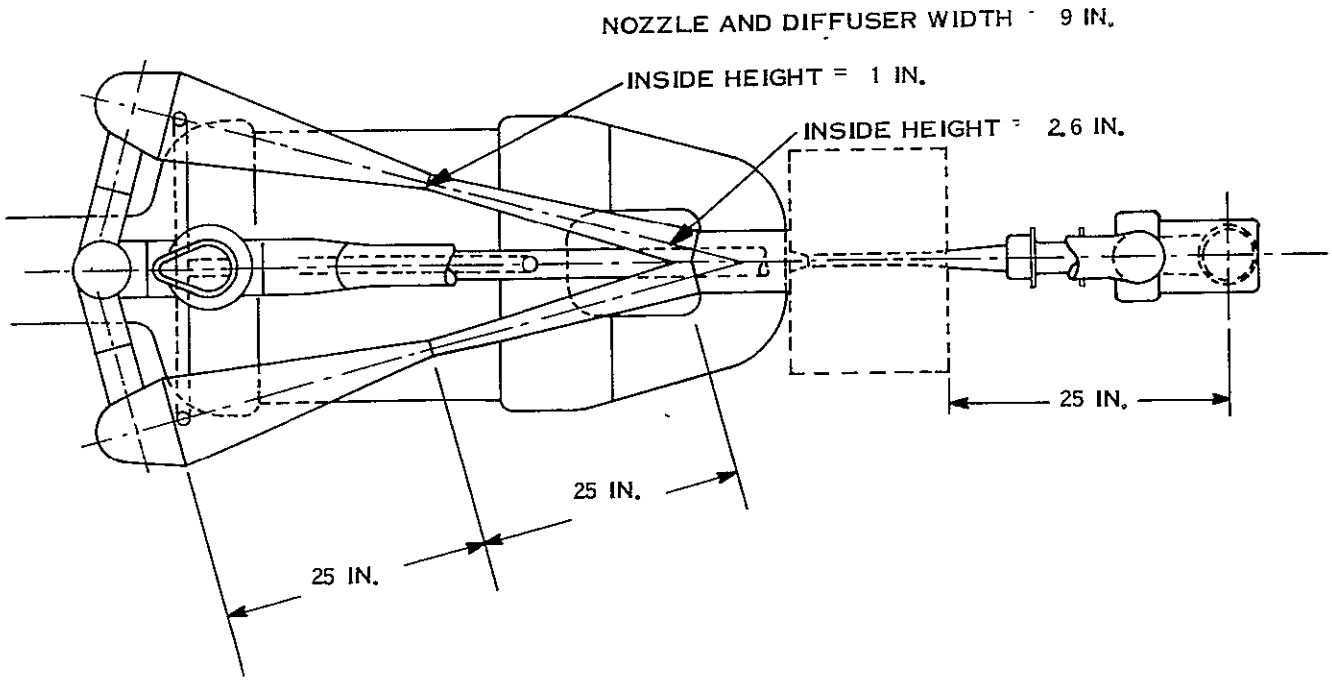

Figure 2-50. MHD Nozzle and Diffuser Size

and the stress, σ, is

$$\sigma = \frac{Mc}{I} = \frac{P\ell^2}{12} \times \frac{6}{t^2} = \frac{P\ell^2}{2t^2}$$

where

t = the height or thickness of the beam

ℓ = the beam length

c = distance from neutral axis to outermost fiber of the beam

M = the bending moment

I = the moment of inertia

P = internal pressure

For throat deflection

ℓ = 9 in., ℓ^2 = 81 in.^{2}, d = 1 in.

y = 0.025 x 1.0 = 0.025 in.

$$\%\epsilon = \frac{1600\ t}{\ell^2}\ y = \frac{1600 \times 0.025}{81}\ t = 0.495\ t$$

For outlet end deflection

ℓ = 9 in., ℓ^2 = 81 in.^{2}, d = 2.6 in.

y = 0.025 x 2.6 = 0.065 in.

$$\%\epsilon = \frac{1600 \times 0.065}{81}\ t = 1.28\ t$$

It was assumed that the nozzle internal pressure is 100 psia at the throat and 10 psi at the outlet end. Therefore, for throat stress:

$$P = 100 \text{ psi}$$

$$\sigma = \frac{100 \times 81}{2t^2} = \frac{4050}{t^2}$$

For outlet end stress

$$P = 10 \text{ psi}$$

$$\sigma = \frac{10 \times 81}{2t^2} = \frac{405}{t^2}$$

To evaluate these stresses in terms of material thickness two materials, Cb-1Zr and TZM, were considered and the following assumptions were made:

a. Cb - 1Zr properties are taken from Reference 23, page 9-26, Figures 9-11 and 9-15 with the time scale of Figure 9-11 of Reference 23 increased by a factor of 1000 to take advantage of the improvements available through annealing. Figures 2-51 and 2-52 here are reproductions of Figures 9-11 and 9-15 of Reference 23. The 0.5 percent creep curve is estimated to be $\sim$ 33 percent of the 1 percent curve (see Figure 2-51).

b. TZM properties are taken from Reference 24 (page 479, Figure 7) indicating that $\sigma_{TZM} \approx 10 \times \sigma_{Nb\text{-}1Zr}$ at 1800°F. Consequently, the stress scale of Figure 2-51 can be multiplied by 10 and the figure used for TZM.

c. The side of the nozzle acts as a fixed-fixed beam.

d. No stress or load redistribution takes place due to creep.

e. Five percent change in passage width allowed for creep over 15,000 hours,

Using these assumptions and the preceding relationships of stress and wall thickness, the wall thicknesses in Table 2-20 were calculated. The weights of the Cb-1Zr nozzle assembly and the TZM nozzle assembly were calculated by assuming that all of the nozzle upstream of the throat and the downstream diffuser are made of throat (100 psi) wall thickness, and that the nozzle downstream of the throat is made of the wall thickness calculated for the end (10 psi). This is an optimistic assumption if the pressure profile shown in Figure 2-49 is representative. The weight calculated for the Cb-1Zr nozzle was 1270 pounds; the weight of the TZM nozzle was calculated to be 850 pounds. The TZM nozzle

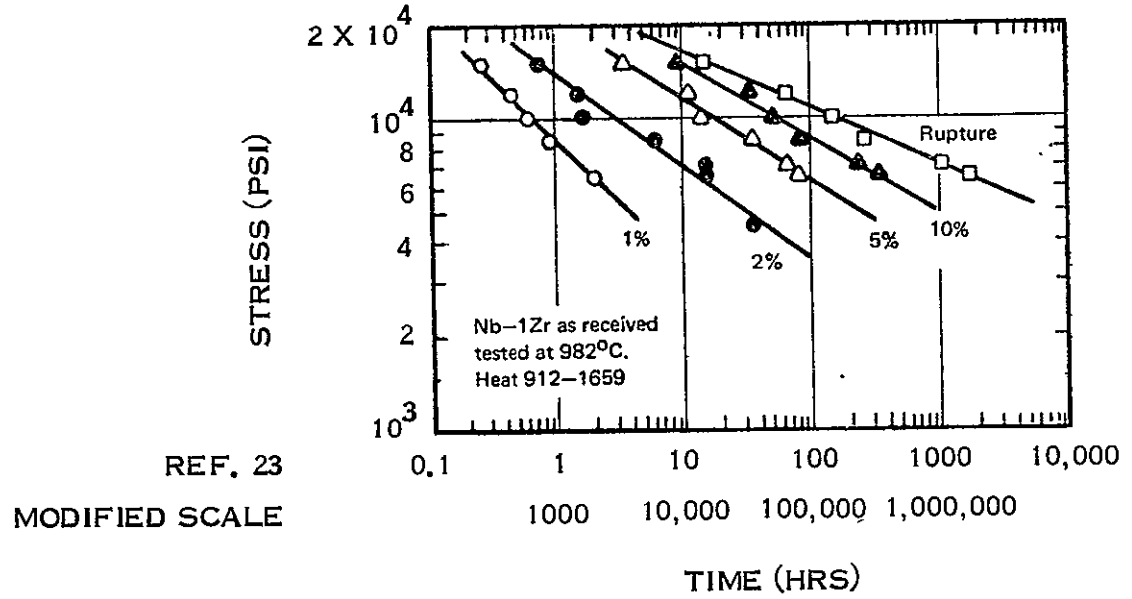

Figure 2-51. Creep Rupture Data for Nb-1Zr Alloy Sheet Tested in Vacuum at 982°C

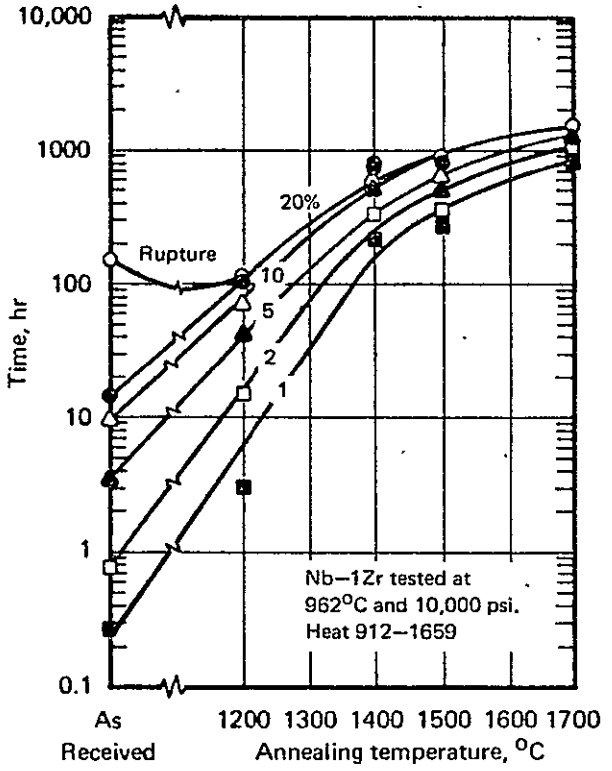

Figure 2-52. Effect of One Hour Pre-test Annealing Treatment on Creek Rupture Strength of Nb-1Zr Alloy Sheet Tested in Vacuum at 982°C

is used in the weight summary, realizing that a Cb-1Zr inner liner may be needed for chemical compatibility with the liquid metal streams.

TABLE 2-20. MHD NOZZLE WALL THICKNESSES

THROAT

T = 1800°F
P = 100 psia

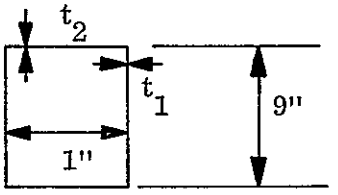

Material	t_1 (in)	t_2 (in)
Nb-1Zr	1.3	0.9
TZM	0.7	0.5

END

T = 1800°F
P = 10 psia

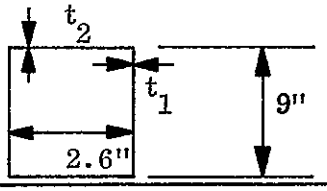

Material	t_1 (in)	t_2 (in)
Nb-1Zr	0.7	0.5
TZM	0.3	0.25

2.6.3.3 Valves and Piping

For the baseline design MHD system, the temperature conditions are such that stainless steel can be used as the containment and piping material on the radiator side of the recuperator and Cb-1Zr for the recuperator and higher temperature sections. Table 2-21 lists the valves required in the MHD power system. It has been assumed that all of these valves can be variations of the high temperature alkali metal valve developed by GE-NSP under NASA Contract NAS3-8514. This valve is shown in Figure 2-53. The motor-operated versions are assumed to have a NaK-cooled drive motor assembly on the pinion gear shaft. The estimated weights of the valves when dry are listed in Table 2-21 and are extrapolated from the 1-inch size valve presently on test which weighs 5.5 pounds dry, without a drive motor. All the valves except the check valve, LV-3, are assumed to be globe type as is the existing valve. There might be an incentive to make some of the valves, especially LV-1 and LV-2, gate valves to minimize pressure drop. Certainly, the development of the globe valve assumes the material technology to build a gate valve for this service; the problem would

Table 2-21. MHD System Valves

Valve	Service	Size Inches	Type	Remarks	Estimated Weight Pounds
LV-1	Lithium Nozzle Inlet	3.5	Motor-Oper. Globe		13
LV-2	Lithium Diffuser Outlet	3.5	Motor-Oper. Globe		13
LV-3	Startup Pump Bypass	2.6	Swing Check		5
LV-4	Lithium Accumulator Control	3.5	Motor-Oper. Globe	1/4-in. port above seat, closed when backseated	13
LV-5	Lithium Loop Drain	1/4	Globe	Seal Weld Cap	2
LV-6	Lithium Loop Vent	1/4	Globe	Seal Weld Cap	2
CV-1	Cesium Nozzle Inlet	1.5	Motor-Oper. Globe		9
CV-2	Radiator Loop Outlet	1.5	Motor-Oper. Globe		9
CV-3	Cesium Loop Drain	1/4	Globe	Seal Weld Cap	2
CV-4	Cesium Loop Vent	1/4	Globe	Seal Weld Cap	2

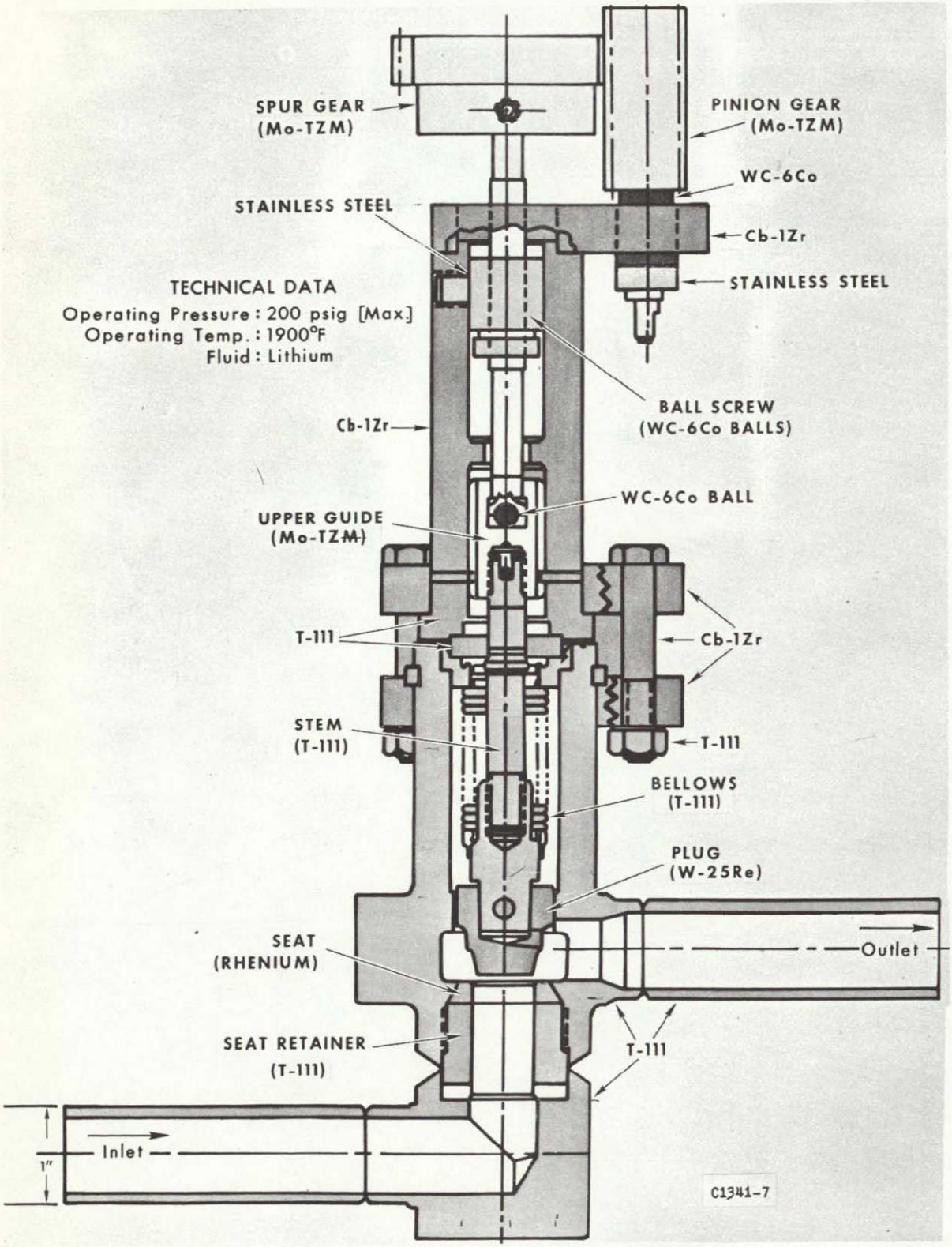

Figure 2-53. Schematic View of High Temperature Alkali Metal Valve

be in reconfiguration. The full-shut to full-open stroke of a gate valve is characteristically greater than that of a globe valve. As a consequence the bellows and other bonnet parts of the design shown in Figure 2-53 would have to lengthen appreciably. Configuration of such a gate type valve was considered briefly but dropped as not worth pursuit at this level of investigation.

The MHD system uses two accumulators for liquid metal inventory and pressure control, both are assumed to be cylindrical, gas-pressure-controlled, bellows type accumulators with a single outlet. The design parameters of these accumulators are listed in Tables 2-22 and 2-23. The lithium accumulator is designed to be exposed to the high ($\sim$150 psia) lithium system pressure only during startup. Valved over to the cesium pump suction by closing Valve LV-4, the lithium accumulator would operate at much lower pressure through the mission and therefore require less creep strength. A shell weight saving of up to 700 pounds is achieved by this approach.

2.6.3.4 Pumps

The MHD power system uses one very large EM pump and several small ones. Guidance for EM pump selection was taken from References 25 and 26 and experience with the potassium boiler feed pump built and being tested by GE-NSP under NASA Contract NAS3-9422 (see Figures 2-54 and 2-55).

Three small pumps are needed to circulate the high and low temperature NaK in the auxiliary radiators (see Paragraph 2.6.4) and to circulate lithium through the reactor during system warmup prior to initial start. Since the small pumps must operate on battery power during system warmup, and their small size makes power conditioning losses negligible, dc conduction pumps of the type illustrated in Figure 2-56 were chosen. The lithium startup pump was estimated to require 350 watts of power for eight hours at 0.7 volts dc to produce a lithium flow of 10 pounds per second at a head of 1 psi. The estimated weight of this pump is 6 pounds and its overall efficiency is 18 percent. Since the weight of this small pump is almost trivial, an assigned weight of 10 pounds for each of the three DC pumps is carried in the weight summary and no further analysis was made.

TABLE 2-22. LITHIUM ACCUMULATOR DESIGN PARAMETERS

Fluid	Lithium
ΔV intake (warmup)	1100 $in.^3$
ΔV expel (startup)	2200 $in.^3$
Temperature	$1800^{o}F$
Pressure, startup, $\leq$ 10 hours	150 psia
run, 10-20,000 hours	5 psia
Material	Cb-1Zr
Shell OD	14 in.
Wall Thickness	0.13 in.
Shell Length	48 in.
Bellows	2 ply, 0.010 in. thick
Bellows Length	34 in.
Number of Convolutions	43
Length of One Convolution	0.786 in.
Bellows OD	13 in.
Bellows ID	10 in.
Dry Weight	132 lb
Wet Weight (at launch)	173 lb

TABLE 2-23. CESIUM ACCUMULATOR DESIGN PARAMETERS

Fluid	Cesium
ΔV intake	160 $in.^3$
ΔV startup	3000 $in.^3$
Temperature	1100^{o}F
Pressure	10 psia
Material	Stainless Steel
Wall Thickness	0.040 in.
Shell Length	40 in.
Shell OD	18.5 in.
Bellows	2 ply, 0.010 in. thick
Bellows Length	26 in.
Number of Convolution	33
Length of Convolution	0.786 in.
Bellows OD	17.5 in.
Bellows ID	14.5 in.
Dry Weight	65 lb
Wet Weight (at launch)	270 lb

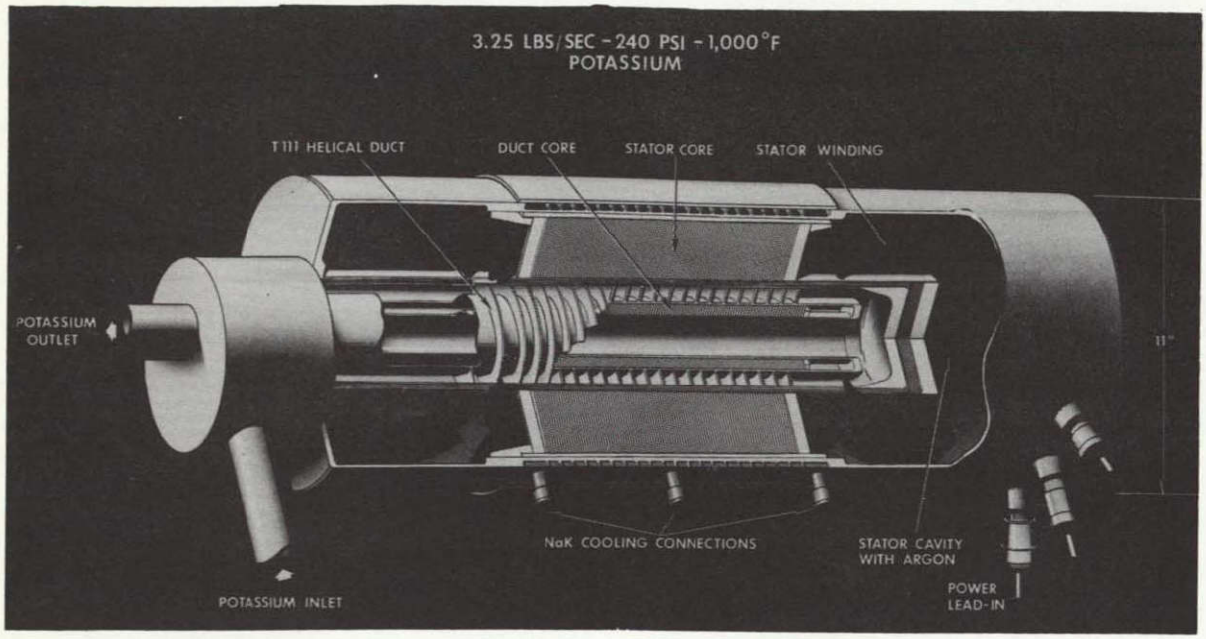

Figure 2-54. Potassium Boiler Feed Pump - Cutaway

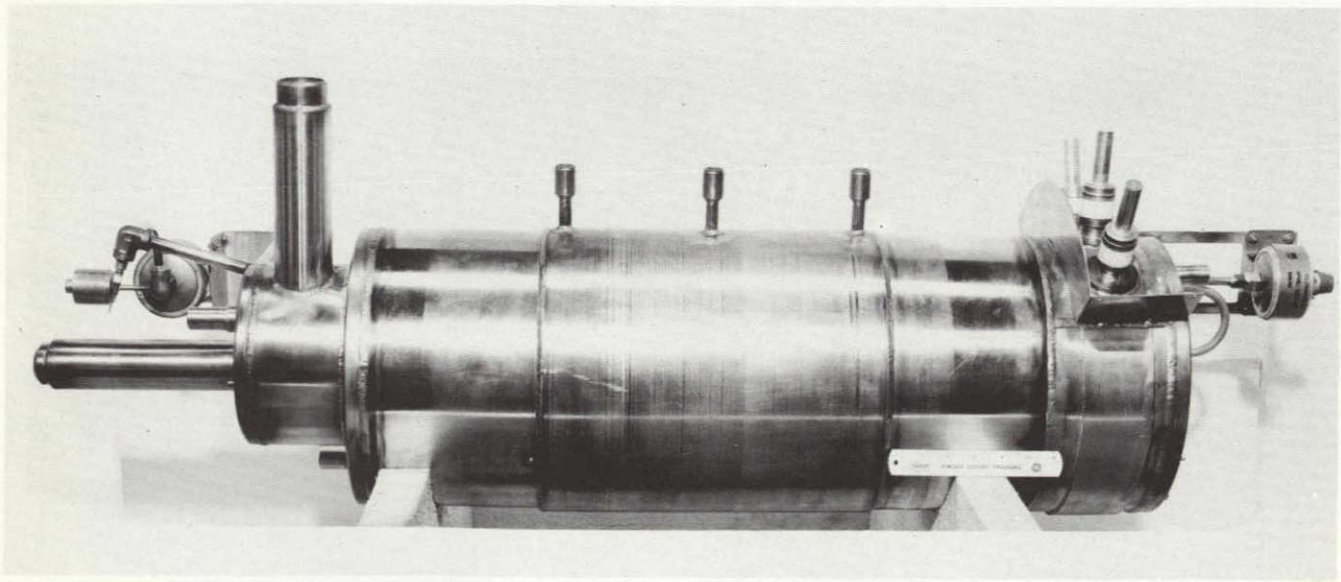

Figure 2-55. Potassium Boiler Feed Pump - Final Assembly

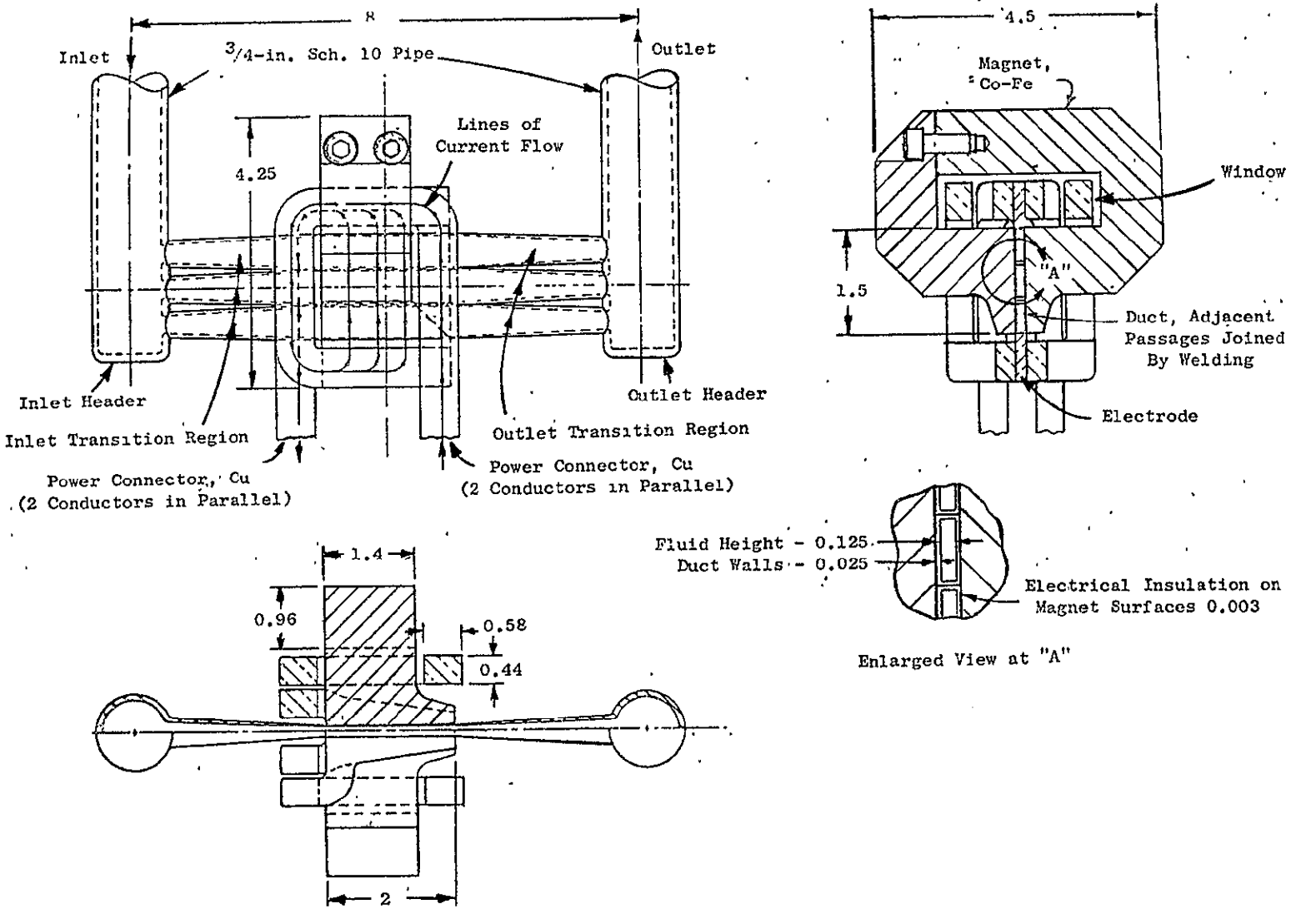

Figure 2-56. DC Conduction Pump

The cesium pump, on the other hand, is required to pump ~13 pounds per second of cesium at a head of 140 to 150 psi. The power required is of the order of 20 kWe. To develop such a high pumping head, the designer is usually inclined toward choice of the helical ac pump; the reliability of the ac pump is also an attractive advantage. In addition, the pump designs analyzed in Reference 25 indicate that the weight advantage enjoyed by dc pumps over ac pumps dwindles from 2.5:1 at low or average heads to as little as 1.5:1 at high heads. Since the MHD system produces ac power at relatively high voltage, it will be easier to supply power to an ac pump. A last, and important consideration, is that the development required for an ac pump would be much less than for a dc pump because of the experience already gained with pumps such as the one shown in Figure 2-55. Thus, it was decided that the cesium pump should be a 3 phase helical induction (ac) pump for the following reasons:

a. Reliability

b. High Head Capability

c. Competitive Weight

d. Minimum Power Conditioning

e. Minimum Development Cost.

Using the Pump Capability Parameter (PCP) as explained in Reference 25, a design curve for the cesium pump was drawn up (Figure 2-57). The slope of the curve is consistent with the designs presented in Reference 25; two points on the curve represent the potassium boiler feed pump operating today and a design reported in Reference 26; the baseline design cesium pump falls between. One further assumption was made, however. It seems reasonable that continued development of this type pump can achieve improved efficiency at current weights or lower weight with current efficiency. It would be very optimistic to expect significant improvement in both simultaneously. The curve in Figure 2-57 represents current weight; current efficiency is just over 16 percent. Since the MHD power system is expected to weigh at least ~40 pounds/kWe output, an efficiency saving is considered more attractive than a weight saving. Consequently, cesium pump design is based on Figure 2-57 weight and an efficiency of 20 percent to reflect design available when the MHD system might be flight-ready.

2.6.4 RADIATOR DESIGN

The MHD power system employs a large, direct-condensing, vapor chamber main radiator to condense the cesium working fluid. The system also uses a number of smaller auxiliary radiators.

2.6.4.1 Main Radiator Design

Study guidelines for the MHD spacecraft specify the use of a triform vapor chamber fin radiator with condensing cesium as the primary fluid. As previously mentioned (Subsection 2.5, Configuration Trade-offs) the cone/cylinder configuration was considered as a possible alternative. Various heat rejection system studies conducted at General Electric have indicated that consideration of radiator structural requirements often decreases the attractiveness of flat panel radiators. Although these conclusions have been based on conduction fin radiator analyses, they might be expected to be valid for vapor chamber fin radiators as well.

Work currently in progress at General Electric under the Vapor Chamber Radiator Study, NAS 3-10615, includes evaluation of four design concepts which are applicable to the MHD radiator. These concepts include:

a. Cylindrical or elliptical tube/fin

b. Rectangular channel

c. Hexagonal honeycomb

d. Rectangular channel/fin

These geometries were compared on the basis of utilization in a cone cylinder, load bearing radiator for the advanced Rankine cycle. Radiator inlet and outlet temperatures were 1200 and 980^{o}F, respectively. Vapor chamber construction was assumed to be stainless steel; wicking material was assumed to be 150 by 150 mesh screen. Sodium, potassium and cesium were the candidate fluids.

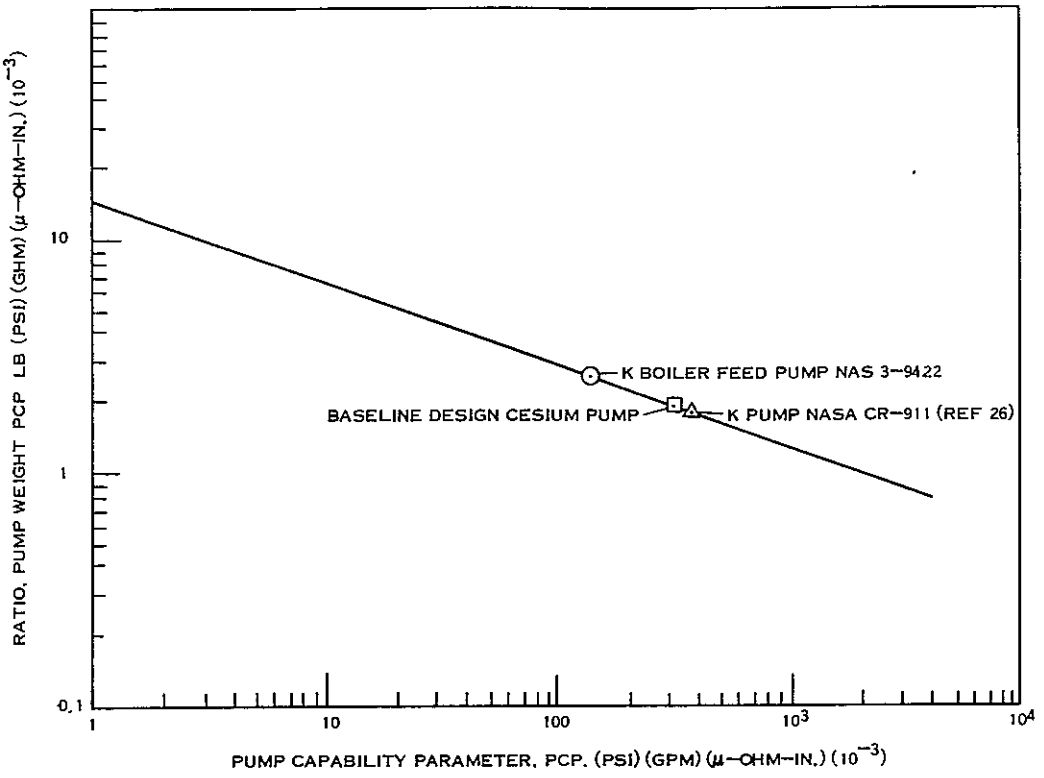

Figure 2-57. Specific Weight Relationship - Three Phase Helical Induction Pump

Radiator weights for each combination of geometries and fluids were calculated over a range of parameters as illustrated in Figures 2-58, through 2-61. A comparison of the vapor chamber fin specific weight versus vapor chamber condenser length is shown in Figure 2-62. The "A" and "C" designations refer to a 0.20 inch and 0.010 inch fin thickness, respectively. During this phase of the study potassium and cesium were excluded from further study due to sodium's superior performance (see Figure 2-63).

In order to obtain a more complete evaluation of the overall radiator weight the vapor chamber fin results were combined with an analysis of the primary ducts. Two duct geometries were examined as shown in Figures 2-64 and 2-65. Figure 2-64 shows an unpenetrated duct whereas the duct in Figure 2-65 is penetrated by the vapor chamber fin. A summary of the thermally optimum total radiator weights including primary ducts, vapor chambers, wicks, and fluid inventory is presented in Table 2-24.

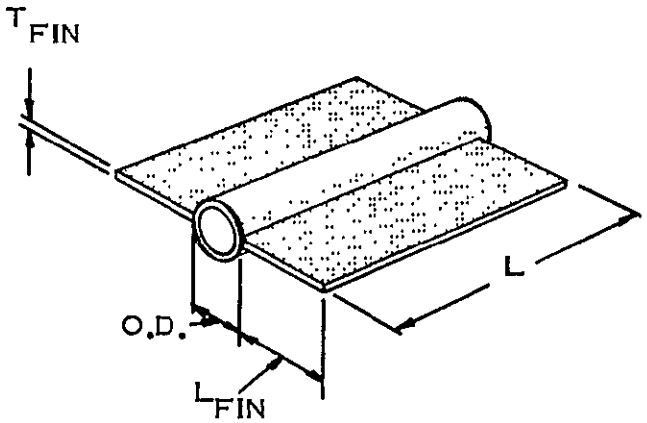

PARAMETERS EVALUATED

LENGTH (L) = 0.50', 1.0', 1.5', 2.0'

O. DIAMETER (O.D.) = 0.500", 0.750", 1.000"

FIN THICKNESS (T_{FIN}) = 0.010", 0.020", 0.040"

FIN LENGTH (L_{FIN}) = 0.000", 0.125", 0.250", 0.500"

TUBE THICKNESS = 0.015

Figure 2-58. Concept 1, Cylindrical or Elliptical Tube Fin

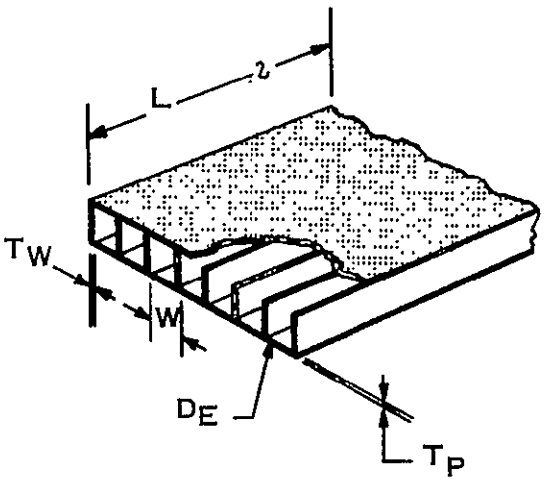

PARAMETERS EVALUATED

LENGTH (L) = 0.500', 1.000', 1.500', 2.000'

EQUIV. DIA. (D_E) = 0.250", 0.500", 0750"

CHANNEL WIDTH (W) = 0.250", 0.375", 0.500", 0.750"
1.000", 1.500"

PLATE THICKNESS (T_P) = 0.015" 0.023"

INNER WALL THICKNESS (T_W) = 0.010"

Figure 2-59. Concept 2, Rectangular Channel

147

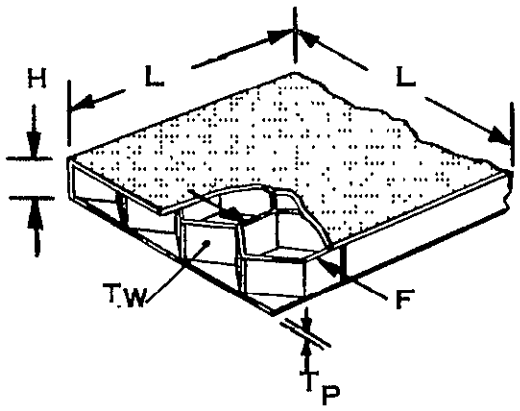

PARAMETERS EVALUATED

LENGTH (L) = 0.50', 1.00', 1.50', 2.00'

DISTANCE ACROSS FLATS (F) = 0.250", 0.500", 1.000", 2.000", 3.000"

HEXAGON HEIGHT (H) = 0.250", 0.500", 0.750"

PLATE THICKNESS (T_P) = 0.005", 0.010", 0.020"

INNER WALL THICKNESS (T_W) = 0.005", 0.010", 0.020"

Figure 2-60. Concept 3, Hexagonal Honeycomb

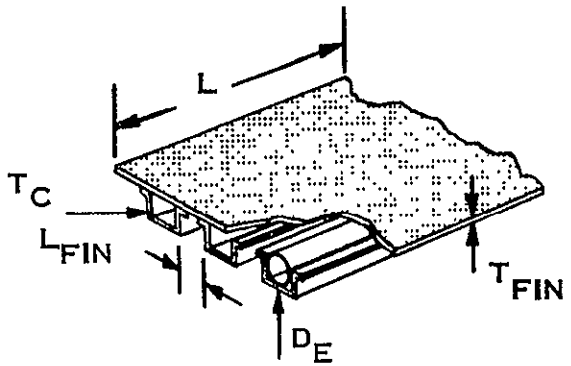

PARAMETERS EVALUATED

LENGTH (L) = 0.50', 1.00', 1.50', 2.00'

EQUIV. DIA. (D_E) = 0.500", 0.750", 1,000"

FIN THICKNESS (T_{FIN}) = 0.010", 0.020", 0.040"

FIN LENGTH (L_{FIN}) = 0.000", 0.125", 0.250", 0.500"

CHANNEL THICKNESS (T_C) = 0.015"

Figure 2-61. Concept 4, Rectangular Channel Fin

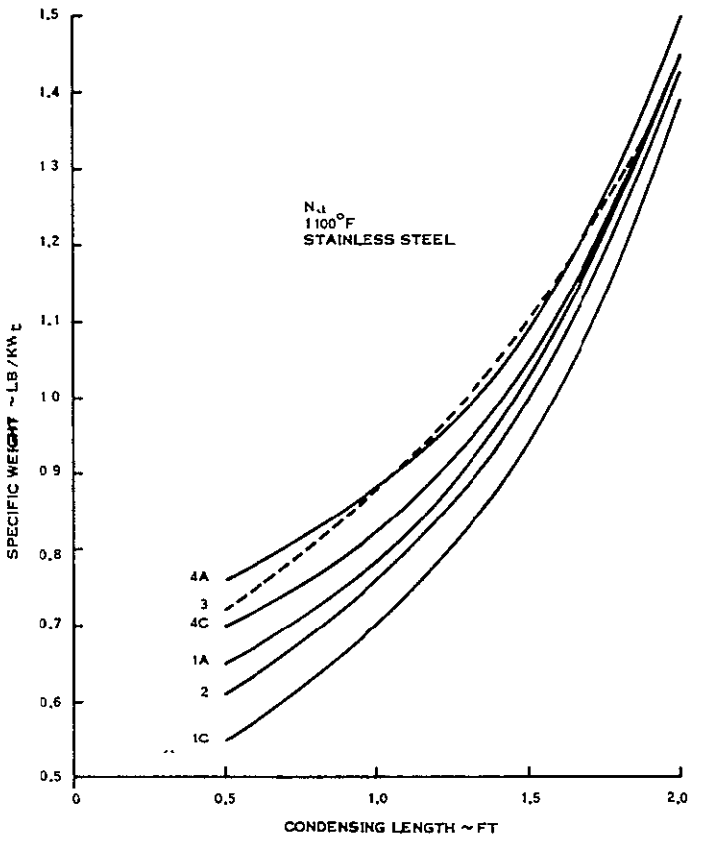

Figure 2-62. Comparison of Condensing Configuration

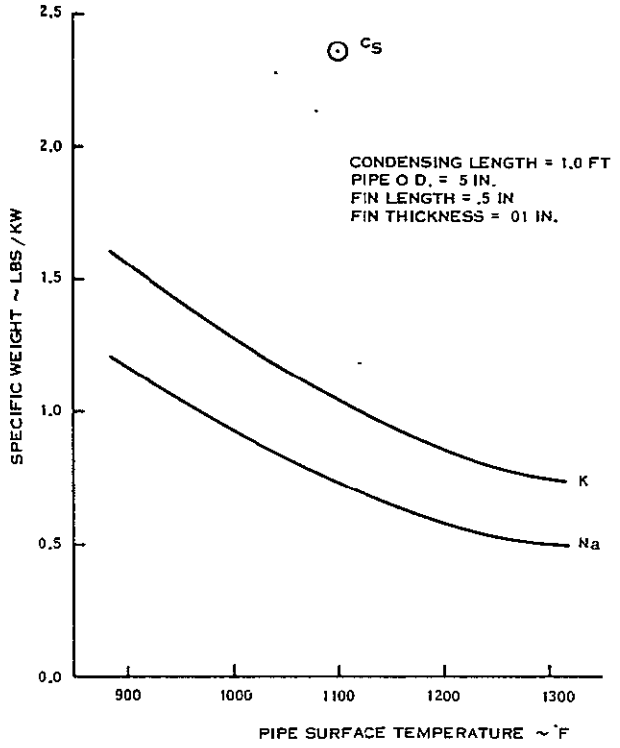

Figure 2-63. Fluid Comparison Finned Cylinder Geometry

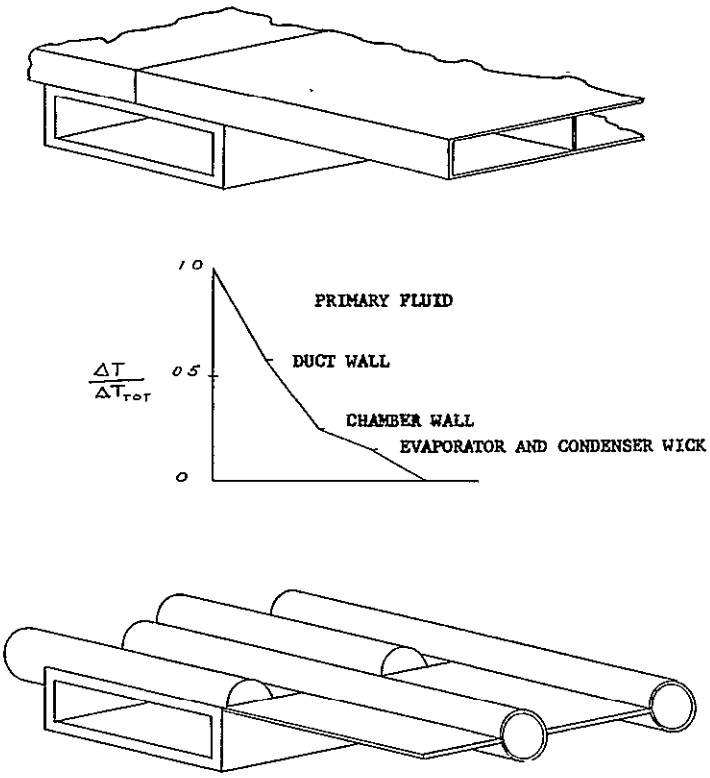

Figure 2-64. Dust-Chamber Concepts - Unpenetrated Duct

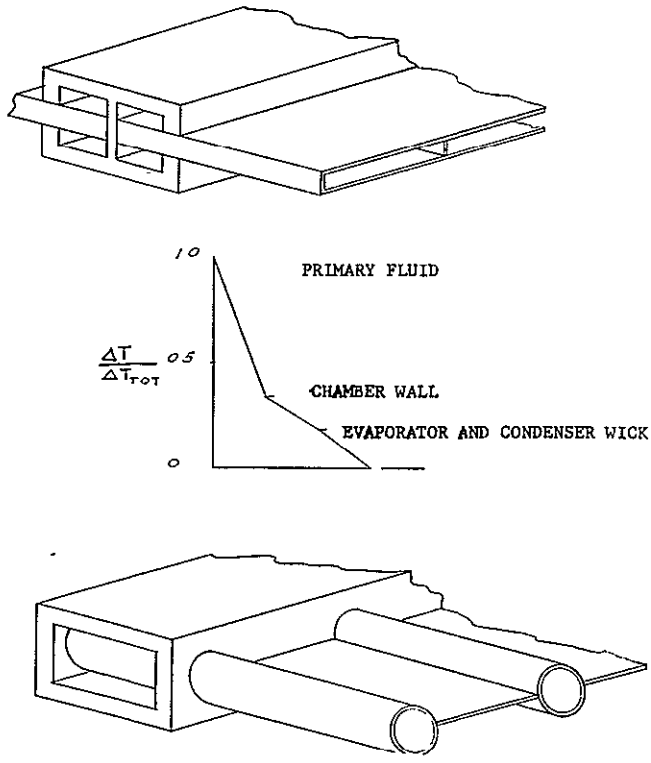

Figure 2-65. Duct-Chamber Concepts - Penetrated Duct

TABLE 2-24. SUMMARY OF RADIATOR WEIGHTS
(NO STRUCTURAL CONSIDERATIONS)

CONFIGURATION (OPEN DUCTS)	WEIGHT (LBS.)	AREA (FT^2)	NUMBER OF CHAMBERS
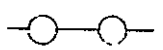 1, 10 mil fins	1510	855	11,500
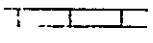 2	1670	630	9,200
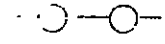 1, 20 mil fins	1700	800	8,500
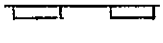 4, 10 mil fins	1710	885	8,900
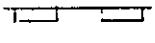 4, 20 mil fins	1850	860	6,550
 3	2500	950	281,000
(CLOSED DUCTS)			
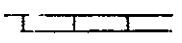 2	1520	750	11,100
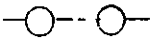 1, 10 mil fins	1800	1000	12,800
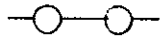 1, 20 mil fins	1950	950	9,050
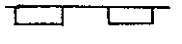 4, 10 mil fins	1980	990	8,950
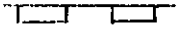 4, 20 mil fins	2075	950	7,700
 3	2850	1370	405,000

The next step in the radiator geometry evaluation was consideration of additional structural members required to support a 15,000 pound power-plant during a Saturn V launch where the radiator is the aerodynamic fairing. Table 2-25 summarizes the complete radiator system weight including structural weight. The lightest weight is obtained using Configuration No. 2 with an unpenetrated duct.

Fabricability of these concepts was also investigated. The easiest geometries to fabricate are cases 1 and 4, however, 2 was also felt to be possible. The fabrication of geometry 3 was judged to be extremely difficult since each honeycomb section must be sealed from adjacent cells.

A final comparison of the concepts on the basis of thermal, structural and fabrication considerations is presented in Figure 2-66. A rating has been assigned to each geometry under each criteria. In view of these results, the concepts, in order of preference, are: rectangular channel, cylindrical and rectangular channel/fin, and hexagonal honeycomb.

Using the rectangular vapor chamber fin geometry, a reference design for the vapor chamber fin radiator was formulated. Sodium was selected as the vapor chamber working fluid because of its high surface tension and latent heat of vaporization. The radiator material of construction was assumed to be stainless steel throughout.

The primary concern in ensuring a reliable vapor chamber design is to satisfy the following expression:

$$\Delta P_c \geq \Delta P_w + \Delta P_v$$

where

ΔP_c = capillary pump pressure rise

ΔP_w = wick frictional pressure drop

ΔP_v = vapor pressure drop

TABLE 2-25. SUMMARY OF RADIATOR WEIGHTS

CONFIGURATION (OPEN DUCTS)	AREA FT^2	NO. OF CHMB'S	WEIGHT RAD.	RINGS REQ'D	RING WT-LBS	REQ. SHEET THK.	SHEET WT.	TOTAL WT.
1, 10 mil fins	855	11,500	1510	6	303	.019	363	2176
2 15 mil plates	630	9,200	1670	4	195	.018	166	2031
1, 20 mil fins	800	8,500	1700	6	283	----	---	1983
4, 10 mil fins	885	8,900	1710	6	314	.019	375	2399
4, 20 mil fins	860	6,550	1850	6	305	----	---	2155
3 .5"cell (.0075")	950	281,000	2500	6	324	.0095	155	2979
(CLOSED DUCTS)								
2 15 mil plates	750	11,100	1520	4	232	.018	197	1949
1, 10 mil fins	1000	12,800	1800	10	560	.018	382	2742
1, 20 mil fins	950	9,050	1950	10	532	----	---	2482
4, 10 mil fins	990	8,950	1980	8	436	.023	470	2886
4, 20 mil fins	950	7,700	2075	8	418	----	---	2493
3 .5" cell (.0075")	1370	405,000	2850	8	464	.011	362	3676

153

CONFIGURATION	THERMAL	STRUCTURAL	FABRICATION	TOTAL RATING (LOW IS GOOD)
1 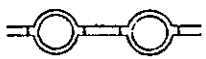	1 HIGH RATIO OF FLOW AREA TO HEAT PIPE CIRCUMFERENCE MINIMUM WEIGHT	4 LOW LOAD AREA AND SMALLER PRIMARY DUCT RADIUS OF GYRATIONS CAUSE LOCAL AND PANEL INSTABILITIES	1 CONSIDERED ON A PAR WITH (4) IF EXTRUSION IS USED	6
2 	1 HIGH EFFECTIVE RADIATOR TEMP. GOOD EVAPORATOR INTERFACE MINIMUM RAD. AREA	1 THERMALLY DEFINED GEOMETRY MORE CLOSELY MEETS LOCAL AND PANEL STABILITY REQUIREMENTS	2 SOMEWHAT MORE DIFFICULT THAN (1) OR (4) BUT USE OF FLANGES PERMITS GOOD BRAZE	4
3 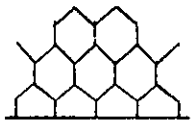	3 GOOD EVAPORATOR INTERFACE POOR HEAT TRANSFER	2 INCREASED RADIATOR AREA REQUIREMENTS NECESSITATE LARGER BAYS ∴ THUS INCREASE PANEL INSTABILITY	3 CONSIDERED VERY DIFFICULT IN THE CHARGING & SEALING OF CHAMBERS	8
4 	2 GOOD METEOROID RESISTANCE AREA COMPARABLE TO (1), HIGHER WEIGHT	3 LOW LOAD AREA AND SMALL PRIMARY DUCT RADIUS OF GYRATION CAUSE LOCAL AND PANEL INSTABILITIES	1 CONSIDERED TO BE SIMPLE TO FABRICATE BY WELDING OR BRAZING	6

Figure 2-66. Evaluation Summary and Recommendations

The capillary pump pressure rise can be estimated by the following expression:

$$\Delta P_c = \frac{2\sigma}{\gamma_P \cos\theta}$$

where

σ = fluid surface tension

γ_P = effective pore radius of capillary wick

$\cos\theta$ = contact angle between the fluid and the wick

From a design standpoint, γ_P is the only degree of freedom in changing the capillary pressure rise, since σ and θ are functions of the fluid. In order to increase the capillary pressure rise, a fine mesh (200 by 200) stainless steel wire screen was selected. This choice provides a substantial pumping capability without imposing too high a frictional pressure drop.

The condenser fluid passage is designed with the following objectives in mind:

a. Minimize the return fluid pressure drop

b. Maintain the fluid in a predictable configuration.

An illustration of the condenser wick geometry is shown in Figure 2-67. The wire diameter is 0.020 inches in diameter and the mesh size is 150 by 150.

Due to the dependence of the sodium vapor temperature on pressure, it is necessary to design the vapor passage so as not to induce any discernable pressure drop in the vapor. The required cross sectional flow area of the vapor is primarily dependent upon the length, width and the temperature level of the heat pipe. Arrangement constraints fix the width of the the triform radiator panel at 64 inches. If one primary fluid duct were used, the condenser would be approximately 32 inches in length which past studies have shown to be far from from optimum for this type of application. In order to maintain more reasonable condenser

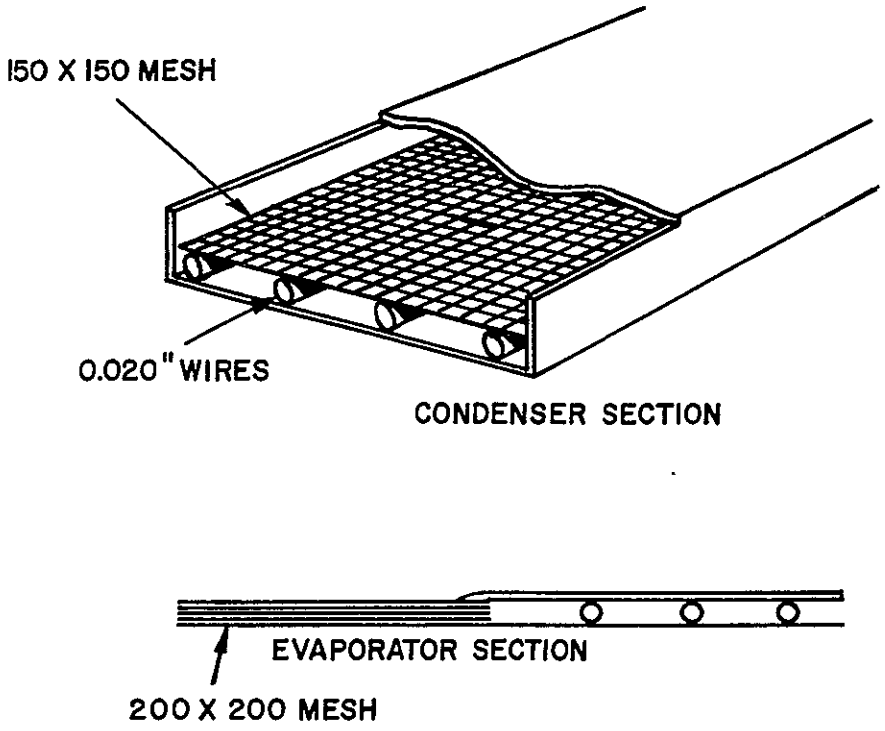

Figure 2-67. Vapor Chamber Wick Geometry

lengths (16 inches), two primary fluid ducts were used. The width of each vapor chamber was limited to 1.25 inches as a result of structural considerations arising from internal gas pressure. Under these conditions, the minimum allowable height necessary to allow vapor flow without an observable pressure drop is 0.300 inches.

The purpose of the primary fluid ducts is to transfer heat to the evaporator sections of the sodium heat pipes. If properly designed, the cesium fluid temperature can remain constant along the condensing length of the radiator panel. The design chosen which is attractive from the standpoint of fabrication, flow geometry and meteoroid protection is the half cylinder duct geometry. The duct was sized to limit inlet vapor velocity to <10 ft/sec. for stable flows; key details of the design are illustrated in Figure 2-68.

One design problem which remains with the baseline system is that the vapor entering the radiator, at 1642^{o}F, has too much superheat for good radiator design. With design iteration, the radiator should be sized to provide further subcooling and the recuperator size should be increased to reduce the superheat at the radiator inlet.

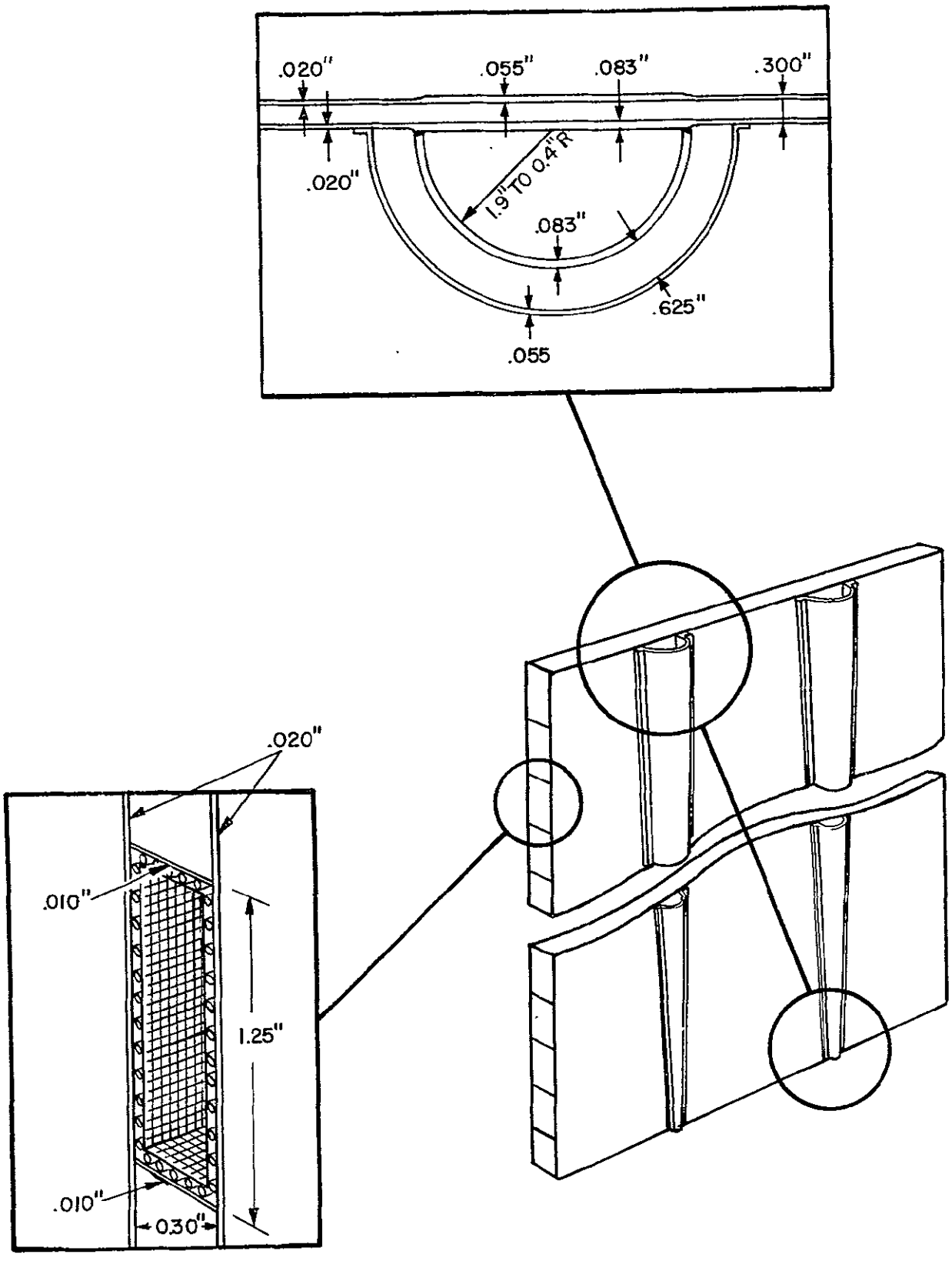

Figure 2-68. Main Radiator Panel Details

2.6.4.2 Auxiliary Radiators

The MHD power system auxiliary radiators are located on the surface of the MHD equipment bay. Table 2-26 lists the salient characteristics of the two active radiators which cool the MHD generator windings, stator, and the pump and valve motors in the MHD bay. The reactor, radiation shield, excitation capacitors, batteries, and the main power conditioning equipment are passively cooled by direct radiation to space.

TABLE 2-26. AUXILIARY-RADIATORS BASELINE DESIGN

Service	Winding Cooling	Stator Cooling
Heat Loads	P_{coil}, 12.2 kW	MHD Generator 35 kW Others 15 kW
Average Temperature	340°F	800°F
Tube Spacing	7.1 in.	3.5 in.
Fin Efficiency	0.88	0.9
Radiator Area	85 ft^2	50 ft^2
Specific Weight	0.97 lb/ft^2	1.9 lb/ft^2

2.6.5 STRUCTURE AND INSULATION

2.6.5.1 Structure

The baseline design spacecraft is made up of two large assemblies connected by a 53-foot long triform main radiator. The head of the spacecraft includes the reactor, radiation shield, and the MHD equipment bay. The reactor is mounted to the top of the radiation shield on short tubular struts. The radiation shield is a stainless steel reinforced, solid lithium hydride block, stiffened both internally and externally. The MHD bay is a rib and skin structural shell extending from the bottom of the shield; internal trusses, ribs and ties carry loads up to the shield or out to the stiffened shell.

The lower assembly of the spacecraft is a cylindrical body containing the main power conditioning equipment, the payload, and the thruster system. All internal loads are carried on the shell structure of the lower assembly; additional trusses are used to take loads

from the radiator spine out to the lower shell. The main radiator is built up on a stainless steel triangular boom 53.25 feet long. This boom is made up of three 1.5- x 1.5- x 0.050-inch thick channel beams which run full length to form the edges of the boom, and 16- x 1.5 x 0.040-inch welded cross bars on all three sides, spaced 39 inches apart. The rectangular openings between the cross bars are spanned by crossed tension ties which run from corner to corner. The vapor chamber panels of the radiator are hung on studs protruding from the channel beams and secured with washers and locknuts. The studs pass through sealed, reinforced holes in the vapor chamber panels. Torsional stiffness is provided by fitting tapered radial trusses between bays. These tapered trusses, shown in Figure 2-40, are made of 1.5- x 1- x 0.060-inch tee section and are welded to the central triangular boom. These radial trusses provide a good structural tie between the central boom and the stiffeners running the full length of the radiator panel outer edges. In addition, they provide support for the feed and return pipes to the two vertical condensing ducts running down each radiator panel.

The outer edges of the radiator panels are fitted with permanent channel type stiffeners which link the panels together to form a light column at each edge of the radiator connecting the head and lower assemblies of the spacecraft. These channels also act as the wireways for all cabling connecting the two ends of the spacecraft.

Following the concept discussed in Paragraph 2.5.3, disposable structure is used to assist the triform radiator in carrying launch loads. Three channels weighing a total of 1970 pounds are fitted over the edge stiffeners of the radiator panels (see Figure 2-35). The size of these channels varies with elevation as is illustrated in Figure 2-69. The disposable structure also includes 320 pounds of stabilizing tubes as illustrated in Figure 2-36. A force and moment distribution diagram for the MHD baseline spacecraft is presented in Figure 2-70.

2.6.5.2 Insulation

In the MHD spacecraft, an effective insulation system is needed to enclose the MHD bay and to isolate the lower assembly of the spacecraft from the main radiator's heat. A trade-off was made to select the insulation from two candidate systems. One is a

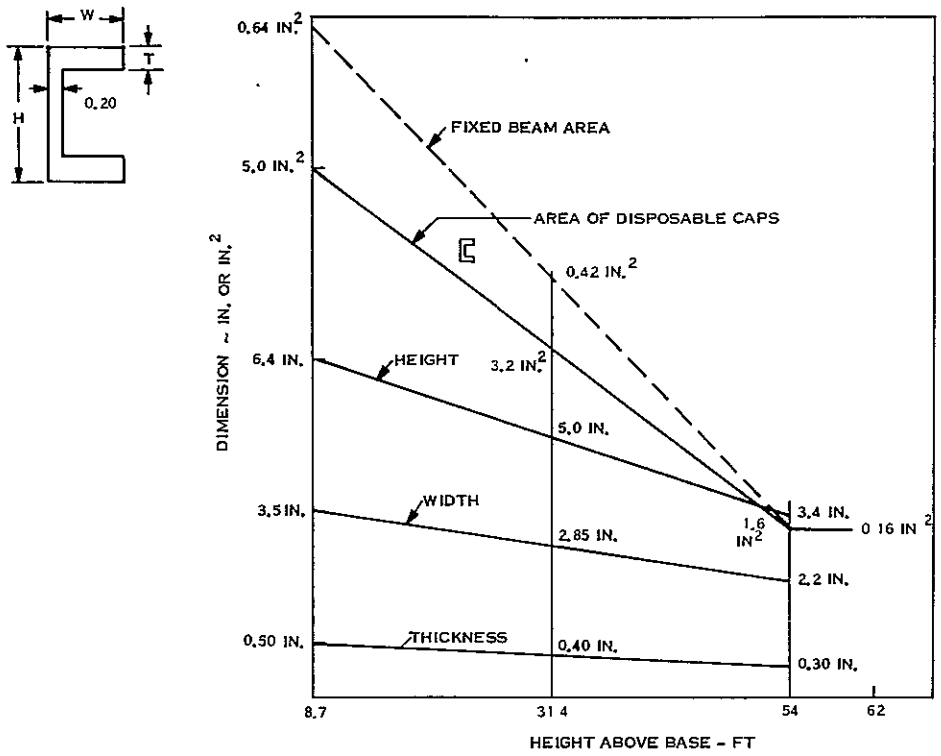

Figure 2-69. MHD - Size of Disposable Structure

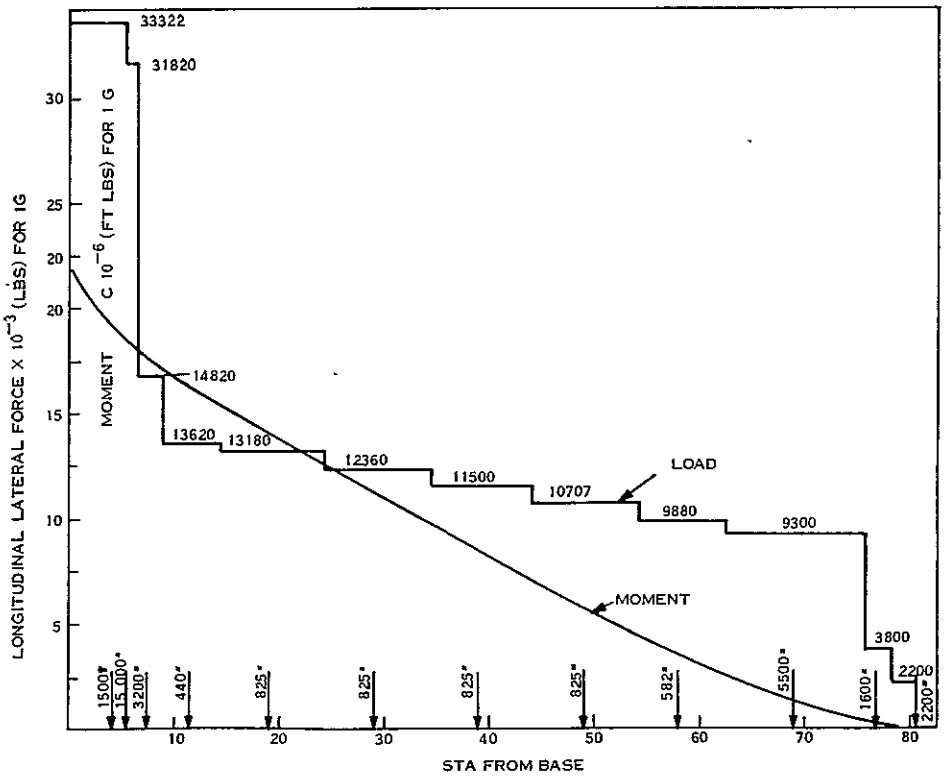

Figure 2-70. MHD - Spacecraft, Unit Force and Moment Distribution

molybdenum/nickel/copper/aluminum multifoil insulation systems which has been successfully tested (Reference 27); the other is a single, thick layer of fibrous insulation, typically Johns-Manville MinK 2000, weighing 25 lb/ft^3. The effective thermal conductance of the half-inch thick (55 layer) multifoil system was estimated to be 20 watts/ft^2 with the insulation weight running 2.2 lb/ft^2 including a 0.020 inch support sheet on the hot (high metal density) side. The conductance of MinK 2000 was estimated to vary with thickness, and were as follows:

Conductance (watts/ft^2)	Thickness (inches)	Weight* (lbs/ft^2
20	4	8.25
40	2	4.125
80	1	2

* Does not include support sheeting

Assuming a 10 percent increase for a support sheet, the 80 watt/ft^2 fibrous insulation system is the same weight as the 20 watt/ft^2 multifoil system; consequently, the multifoil system was selected.

2.6.6 ELECTRICAL SYSTEM DESIGN

The electrical power system and its components have been designed for use in an electrically propelled spacecraft with an MHD generator as a source of power. Estimates have been made of size, weight and efficiency of the equipment.

2.6.6.1 Requirements/Characteristics

The primary requirements of the electrical system are to convert the electrical power developed by the magnetohydrodynamic (MHD) generator to forms suitable for use by the various electrical loads and to distribute the electrical power with proper protection and control.

2.6.6.1.1 Load Requirements - A tabulation of the spacecraft loads and their electrical requirements is given in Table 2-27. Thruster power requirements are shown in Table 2-3. The main portion of the electrical power is required by the ion thruster screen grids which require about 7.2 kW each at 3100 volts dc. A total of 37 thrusters are on the spacecraft of which 31 are active and 6 are spares.

The ion engines, which represent the principal electrical load of the entire system, are known to arc frequently. When arcs occur, it is necessary to shut down the arcing engine to allow the arc to extinguish, then restart it. Since the engines are a large percentage of the total load, it was necessary to investigate whether the arcing and consequent shutdowns significantly diminish the average load represented by the engines. Analysis shows that even at the extreme arcing rate of 20 per hour the reduction in average load is only about 3.5 percent. Since arcing frequency tends to diminish with time, the reduction in average load by thruster arcing may be neglected.

2.6.6.1.2 Mission Requirements - The electrical system must be designed to provide power to the loads under the following conditions during the flight:

a. Full power operation (300 kW) from beginning of mission to the coast period

b. Ten percent power operation (30 kW) during coast; the thrusters are inoperative and only hotel loads and payloads are connected

c. Full power operation (300 kW) from the end of the coast period to attainment of orbit around Jupiter

d. Ten percent power for at least one orbit of Jupiter.

2.6.6.1.3 Electrical System Requirements. The primary function of the electrical system is that it transforms the generator output for use in the electrical loads. Transmission cable weight and the corresponding power losses associated with power transmission require that power be transmitted at as high a voltage as practical.

MHD electrical characteristics are shown in Table 2-28. Electrically, this MHD generator is a 23 slot linear induction machine with capacitors providing the excitation current. Each slot is considered as a separate phase. Relative angles of the phases with respect to a

TABLE 2-27. SPACECRAFT ELECTRICAL LOAD REQUIREMENTS

Item	Function	Power Required - kW
Cesium Pump	Returns cesium condensate to MHD cycle	18.3
Auxiliary Pump	Cools MHD generator windings	0.35
Auxiliary Pump	Cools MHD generator stator, pumps, etc.	0.35
Startup Pump	Circulates Lithium for Startup	0.35
Reactor Controls	Controls reactivity of reactor	1.0
Thrusters	Propulsion	240.0
Payload, Science	Science and Communications	1.0
Guidance and Control	Thrust vector control - ion engines	0.5
System Controls	Protection, switching and control of electrical system	0.5

TABLE 2-28. GENERATOR ELECTRICAL CHARACTERISTICS

Slot	Voltage (Volts)	Current (Amperes)	Current Angle* (Deg)	Phase Angle* (Deg)	Real Power (kW)	Reactive Power (KVAR)
0	704.4	244.5	-36.4	-61.8	-81.31	151.8
1	944.0	57.9	35.5	70.2	18.51	51.4
2	936.5	57.8	33.9	70.9	17.72	51.1
3	928.8	57.8	32.3	71.6	16.94	50.9
4	920.9	57.8	30.7	72.3	16.17	50.7
5	912.8	57.9	29.1	73.1	15.41	50.6
6	904.5	58.1	27.5	73.8	14.66	50.5
7	896.1	58.3	26.0	74.6	13.92	50.4
8	887.5	58.6	24.4	75.3	13.21	50.3
9	878.8	59.0	23.0	76.1	12.50	50.3
10	869.9	59.4	21.6	76.8	11.80	50.3
11	860.9	59.9	20.2	77.5	11.12	50.4
12	851.9	60.4	18.9	78.3	10.46	50.4
13	842.8	61.0	17.6	79.0	9.80	50.5
14	833.7	61.7	16.3	79.7	9.16	50.6
15	824.5	62.4	15.2	80.5	8.53	50.7
16	815.4	63.2	14.0	81.2	7.91	50.9
17	806.2	64.0	13.0	81.9	7.29	51.1
18	797.1	64.9	11.9	82.6	6.67	51.3
19	788.1	65.8	11.0	83.3	6.05	51.5
20	779.1	66.8	10.0	84.0	5.41	51.7
21	770.1	67.8	9.2	84.8	4.75	52.0
22	723.7	325.3	50.2	54.1	138.15	190.7
Total Power Generated					294.84	1410.2
Frequency: 326 Hz						

* Definition:

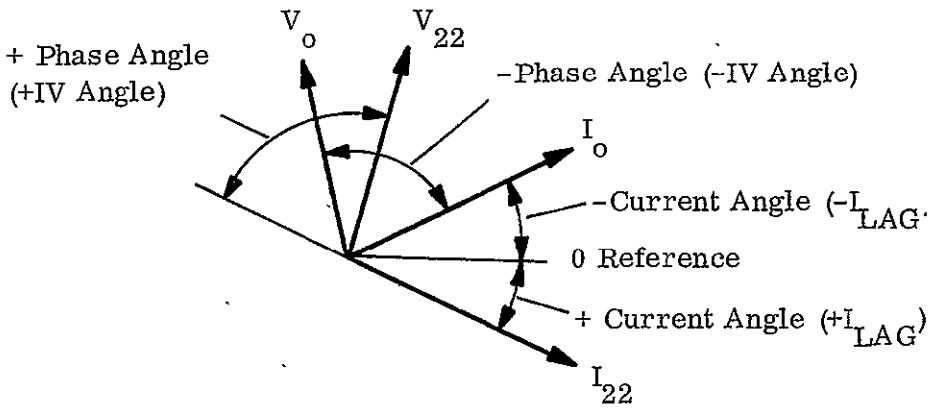

reference are designated as current angle in Table 2-28; angle between the individual phase voltage and current is given as phase angle.

The total power listed in Table 2-28, 294.84 kWe, is the theoretical output power based on perfect travelling wave form. As the analysis of Reference 8 indicates, the output of a generator with a finite number of slots will be lower. In this case, with 23 slots, the penalty is 3 percent, reducing the available power output of the baseline MHD generator to 286 kWe.

2.6.6.2 Electrical Power System Design

The electrical power system for the baseline spacecraft is shown in Figure 2-71.

In this system, the electrical power output from each slot is considered as a separate phase with different output potential. To supply the two distribution busses, each phase is transformed to two standard secondary voltages, rectified, filtered and connected in parallel.

The high voltage output bus provides power to all of the screen electrodes of the ion thrusters. The 3100 volt level is established by the voltage requirements of the screens. Regulation for the high voltage system is assumed to be provided by varying the input voltage to the cesium EM pump, which in turn affects the MHD generator output, see Paragraph 2.6.6.2.7.

The 250 volt output provides power to the remaining spacecraft loads including the several power supplies required for each thruster, as well as the hotel loads and payloads. The 250 volt potential was selected for auxiliary power distribution being relatively high voltage for cable power loss minimization, but below most corona and arc-over levels regardless of atmospheric pressure and humidity. Electrical insulations, and components are frequently rated for maximum voltages not to exceed 600 volts at nominal temperatures. To avoid having to use special high voltage components, and considering the higher operating temperature of the spacecraft, 250 volts was confirmed to be the acceptable maximum.

The electrical power balance for the baseline system is presented in Table 2-29 and a summary of electrical component weights is presented in Table 2-30. As is shown in Table 2-29, the power capacity for the MHD generator is slightly greater (4 kWe) than the sum of all electrical loads and losses.

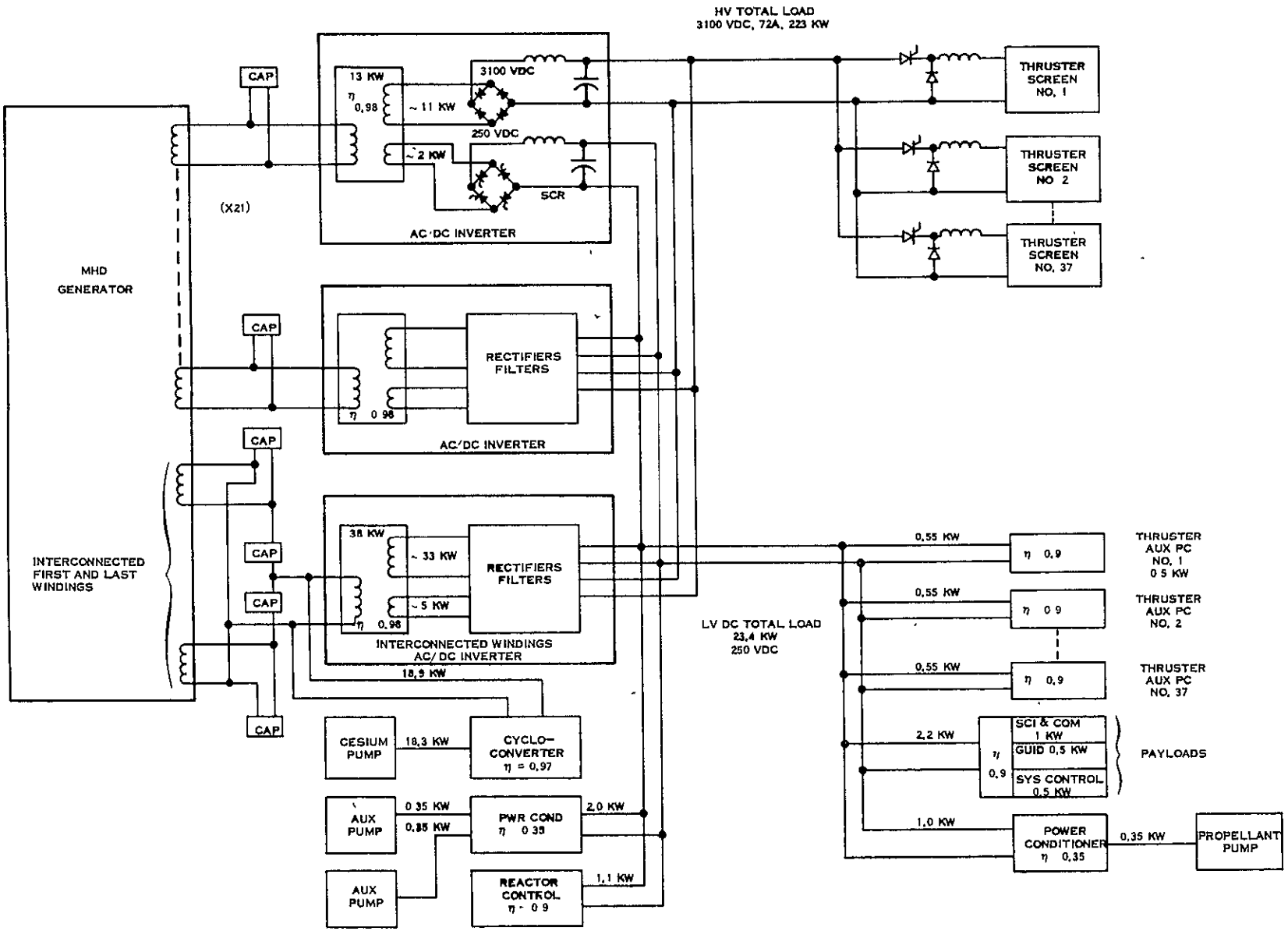

Figure 2-71. MHD Spacecraft Electrical Power System

TABLE 2-29. MHD BASELINE SYSTEM POWER BALANCE

Losses	Watts
Power Transformers	5700
Rectifiers - High Voltage	528
- Low Voltage	220
Filters - High Voltage	1235
- Low Voltage	150
Transmission Cables - Inverter Cable	270
- High Voltage Cable	40
- Low Voltage, EM Cable	150
- Low Voltage, Auxiliary Cable	40
Excitation Capacitor Dissipation (0.5% of 1410 KVAR)	7000
Screen Interrupters	1250
Thruster Auxiliary Power Cond. (15.5 kW, η = 0.9)	1550
EM Pump Power Cond. Cs (18.3 kW, η = 0.97)	550
Auxiliary (1.05 kW, η = 0.35)	2950
Payload Power Cond. (2 kW, η = 0.9)	200
Reactor Controls Power Cond. (1 kW, η = 0.9)	100
(Total Losses)	(21,933)
Loads	
Thruster Screens	223,000
Thruster Auxiliary Power	15,500
Payloads, Science and Communication	1,000
Guidance	500
System Control	500
Cesium Pump	18,300
Small EM Pumps	1,050
Reactor Control	1,000
(Total Losses)	(260,850)
Total Power Required	282,000
Net Power from MHD Generator	286,000
(Surplus Power)	(4,000)

TABLE 2-30. ELECTRICAL SYSTEM WEIGHT SUMMARY

Component	Weight (pounds)	
Inverters		
Transformers	737	
Rectifiers - High Voltage Bus	4	
- Low Voltage Bus	1	
Filters - High Voltage Bus	170	
- Low Voltage Bus	45	
Wire, Brackets, Heat Paths, Control Logic	412	
Total		1369
Excitation Capacitors		
Travelling Wave Region		715
Interconnected First and Last Winding (est)*		530
Screen Supply Interrupters		310
Auxiliary Power Conversion		367
Thruster, Auxiliary Power Conversion		272
Power Distribution Cables		320
Startup Batteries		240

* See Paragraph 2.6.6.2.5 Excitation Capacitor Selection

2.6.6.2.1 Inverter Design - MHD output characteristics and the load requirements lead to candidate circuits for inversion/conversion systems.

The possibility of resolving combinations of the 23-phases into a three phase balanced system was examined and rejected. No amalgamation of the phases would result in a balanced system. An unbalanced system would be difficult for the loads to use, and may introduce harmonic problems. Multi-phase connections were also considered.

A continuation of the three/multi-phase reasoning suggested a complex transformer design whereby the system could be balanced by winding vernier coils in the transformer secondary. For example, a Z connection could be made of the phases, resulting in a near balanced

situation; a small winding would then be wound on a secondary phase with the appropriate voltage and phase angle to balance the system. The disadvantage of this method would be in the complexity of design of the transformer. Assuring proper loading of all the generator outputs to obtain maximum contribution would be difficult.

Considering the various phase angles, different power output capabilities of the phases, and the fact that the majority of the load is at 3100 volts vdc, the best alternative is to transform, rectify, filter and combine the outputs into a common bus.

Details of the basic power inverter are shown schematically in Figure 2-72.

Either of two philosophies may be used in sizing the inversion equipment. One is to design the inverters for each output characteristic; the alternative is to have a universal inverter.

The individual inverter design approach results in minimum weight equipment but would require different designs for each phase. For estimating purposes, equipment weights can be calculated using average MHD generator outputs, recognizing that some equipment may be smaller and lighter than average and some may be larger and heavier. Because of the difference in the electrical characteristics of each phase (slot) in the MHD Generator, 22 different designs would be required.

The alternate philosophy is to have a single design of power conversion equipment and apply this design to all output phases. This approach requires that the conversion equipment be capable of operating with all extremes of MHD output, as it must be capable of handling the largest current and highest voltage of all phases. Difference in input voltage would be corrected by using transformer taps. The inversion equipment would be over-designed.

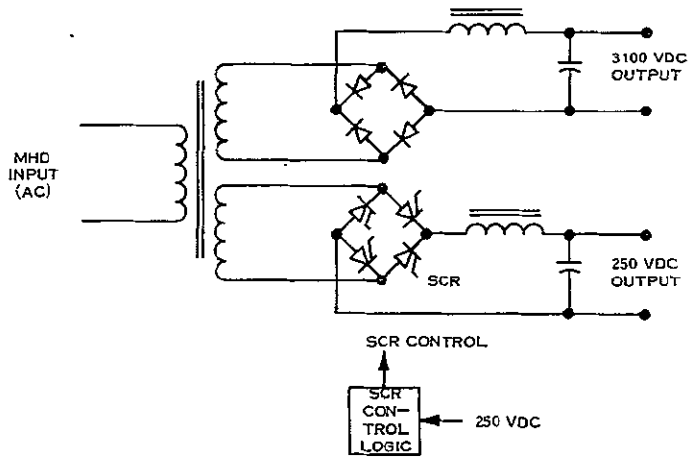

Figure 2-72. Power Inverter

Although the latter approach is preferred from the standpoint of design commonality, the first approach will be used for equipment sizing for this study, since it results in the optimum design for a weight limited spacecraft. The power inversion equipment for the phases in the wave region will be sized for average power output and average voltage, and the equipment for the interconnected phase 0 and 22 in the compensating region will be sized individually. It should be remembered that some inverters may be larger and some smaller than average.

From the MHD Generator data shown in Table 2-28 an average power output of 11.3 kW and an average voltage output of 860 volts vac were selected as characteristic of the travelling wave region.

With disproportional larger power generated in Phase 22 and a power demand in Phase 0, these phases are interconnected. The remaining power is 56.84 kW. To further balance the power contributed to the common bus and to minimize transformation losses the second largest power user, the 18.3 kW cesium pump is connected across the interconnected output via a single phase to three phase cycloconverter.

2.6.6.2.2 Transformer Design - Each transformer for the individual outputs must be unique in design because of different rms voltages and power generated. For sizing, however, an average design was calculated, acknowledging that some transformer may be larger and some may be smaller.

The average transformer design was based on a 13 kilowatt unit with 775 volts ac sine-wave input and the secondaries were assumed to be 3100 volts vac, 4 amperes, and 250 volts vac, 4 amperes. These values were obtained prior to the selection of the baseline design. The baseline design requires an average transformer of 11 kilowatts which would be lighter by approximately 10 percent. Frequency for the average transformer design was 275 Hz compared with the baseline design value of 326 Hz.

Because of the frequency, Silectron AH 4 mil thick core material was selected for the transformer. Magnetic flux density (B) was 12 kilogauss. Design resulted in an HA-320 core (Arnold Engineering Company), with a primary of 407 turns of No. 12 gauge copper

wire, and secondaries of 1628 turns and 135 turns of No. 16 gauge wire. Total weight was found to be 32 pounds with an electrical efficiency of 98 percent. The interconnected first and last phase generator outputs with the cesium pump connected, required a transformer of 35 kilowatts at 500 volts vac prior to the baseline design selection. The baseline design requires a 38 kilowatt transformer which would weigh correspondingly more.

Design of the interconnected output transformer resulted in an Arnold Silectron AH 1207 core, with 111 turns of bifiler wound No. 8 gauge copper wire primary and 690 turns and 55 turns of No. 21 gauge secondaries. Interconnect transformer weight was calculated to be 65 pounds with electrical efficiency of 98 percent.

Total transformer characteristics are as follows:

Weight	Power Loss	Volume
737 Pounds	5700 Watts	3540 $in.^3$ (2.0 ft^3)

2.6.6.2.3 Rectifier Design - Rectification of the high voltage alternating current is performed at the output of each phase transformer through a bridge circuit. Three series 1N1348RA diodes rated at 600 volts Peak Reverse Voltage (PRV) are in each branch. The diodes are rated at 6 amperes maximum allowable forward current, weigh 0.25 ounces and have forward voltage drop of one volt and electrical loss of 4 watts each, for a total of 4.2 pounds and 528 watts loss.

Rectification and low voltage regulation is performed by phase controlled Silicon Controlled Rectifiers (SCR's). In an ac circuit, the SCR must be triggered into conduction at the desired instant of time during the half-cycle of the applied voltage wave during which the anode is positive. In the phase controlled circuit, initiation of conduction is delayed by an angle so that the SCR conducts for only a predetermined portion of the positive half-cycle. In this manner, the average power delivered to the load can be varied, and when coupled with a filter, the output results in a voltage regulated dc bus. When the line voltage reverses every half-cycle, the SCR will be automatically commutated off and consequently will not require special circuits.

The unit seclected for this application is the GE-SCR type C10 series 2N1777A, with a repetitive PRV of 400 volts and a 7. 4 ampere rms limit. Total weight for the SCR's for the 250 volt bus is 1. 1 pounds and electrical losses are 220 watts.

2. 6. 6. 2. 4 Filter Design - In both the high voltage and low voltage circuits, the output filters are used to lower the ripple factor after the transformer output has been rectified. The filters act as storage devices supplying power during periods when the transformer output is below the level of the common bus.

The problem was to design an LC filter which would reduce the pulsating full-wave rectified output to a 3100 volt dc level with 5 percent permissible ripple. Twenty-two parallel inverters will be providing power to the bus with fixed phase differences.

Analysis has shown that for the 3100 volt system, an inductor in each circuit should be at least 340 mh, with a capacitor on the common bus of 4 8 μfd. For the low voltage system, the individual inductors should not be less than 25 mh with a common capacitor of 75 μfd.

Attention was given to the critical inductance to prevent current cutout during the cycle. There is a minimum inductance for a given current below which cutout would occur, although for larger values than this critical value, the conduction would continue for the full cycle. If the rectifier is to pass current throughout the entire cycle, the peak current delivered must not exceed the dc component. The dc value is (E_{dc}/R_L) and the peak ac current is $(2\,E_{dc}/3)\ (1/X_L)$. Hence, for current flow during the full cycle (Reference 28):

$$\frac{E_{dc}}{R_L} \geq \frac{2\,E_{dc}}{3} \quad \frac{1}{X_L}$$

from which the critical inductance is found to be

$$L_C = \frac{2\,R_L}{3W}$$

For the high voltage and low voltage filter circuits the critical inductance is 182 mh, and 12 mh, respectively.

Inductor design resulted in selection of Silectron, 4 mil thick core material. Parameters for the inductors for the traveling wave outputs are as follows:

Bus	Core	Turns/Wire	Weight (each)	Power Loss (each)
250 volts	AH - 223	200 No. 16 gauge	1.6 pounds	6 watts
3100 volts	AH - 188	1000 No. 18 gauge	7.2 pounds	53 watts

For the interconnected first and last outputs, the inductor for the high voltage is estimated to have a weight of 16.5 pounds and a loss of 125 watts; the 250 volt bus inductor is computed to weigh 3.7 pounds with a loss of 15 watts.

Because of the common busses, individual filter capacitors are not necessary; single capacitors will suffice for each bus. Capacitors for the LC filters for the 250 and 3300 volt busses were appraised at minimum capacitance of 72.3 μfd and 4.8 μfd, respectively. The high voltage capacitor was selected to be 5.8 μfd - 7500 volts dc, GE catalog No. 14F1418, dc case style 70, weighing 10 pounds. The low voltage capacitor was selected to be 75 μfd, 1000 volts dc, GE catalog No. 23F1024, dc Case style 72, weighing 6.6 pounds.

2.6.6.2.5 Excitation Capacitor Selection - The function of the capacitors which are connected in parallel with the load to the MHD generator is to supply the excitation component of current in order for the generator to deliver the required power. Computer analysis has shown that except for the interconnected first and last windings, a total of 713.6 μfd is required to be connected across the outputs for an average of 34 μfd each.

A limited industry search has shown that no units are avilable without development; however, the technology exists for designing a capacitor to meet the requirements.

General Electric Company, Capacitor Department was asked to make an estimate of the size and weight of a bank of capacitors, and reports that a building block unit of 5 μfd, 6 x 4 x 3 inch, weighing 5 pounds may be developed for this application. Applying the specific weight of 1 pound/μfd and 14.4 cubic inches/μfd, the capacitors for the traveling wave region would weigh 715 pounds and have a volume of 10,300 cubic inches, 6 cubic feet.

Selection of the excitation capacitor requirement for the interconnected first and last winding output is not complete, however two approaches are being considered and are shown in Figure 2-73. Capacitance for the three capacitor methods requires 645 μfd, 690 μfd and 390 μfd for C_1, C_2 and C_3, respectively. Weight and size estimates for C_1 and C_2 knowing the capacitance cannot be performed as above since these parameters are a function of reactive volt amperes, and are considerably less for these capacitors than for the others. Capacitances for the four capacitor method have not been calculated, but will result in less capacitance than the other method. For arrangement purposes these interconnect capacitors were assumed to be the same size as 70 of the standard 5 μfd units and a weight estimate of 530 pounds, 1.5 times standard, is carried.

2.6.6.2.6 Thruster Screen Interrupters - The high voltage electric system configured for the MHD generator is based on the use of a common thruster screen supply with individual static-circuit interrupters for each thruster.

In order that a common screen supply be feasible several factors must be considered. If all screens are fed from a common supply, all are interconnected electrically. Hence, it is necessary that such interconnection be compatible with the complete electrical system, including the thruster auxiliary power conditioners. Also, it must be possible to isolate individual thrusters from the common supply in the event that the thrusters fail on momentary arc-over.

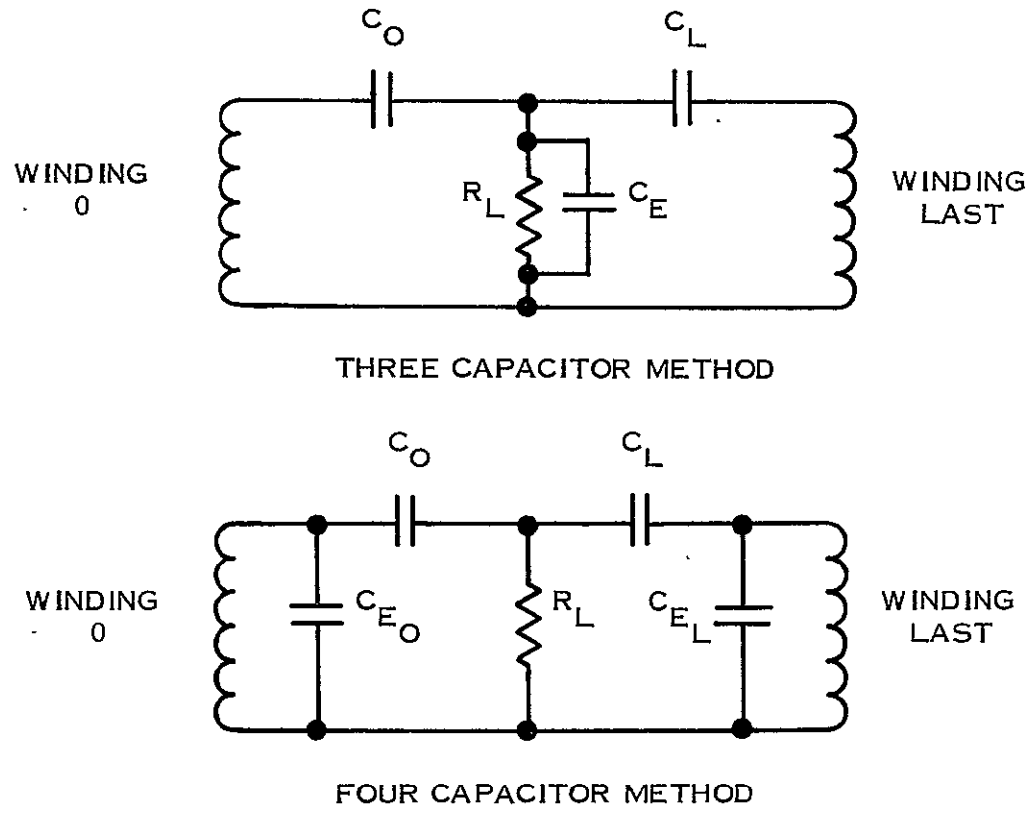

Figure 2-73. Interconnection, First and Last Winding

Each individual thruster screen is fed from the common high voltage bus at the thrusters through a series network consisting of a high speed electronic switch (SCR) and a series reactor (L). Simplified schematic diagrams of the common bus connection and the static switch used as the screen circuit interrupter are shown in Figures 2-74 and 2-75. A number of SCR's are connected in series to withstand the high voltage of the screen supply and are connected in parallel with resistor-capacitor networks to provide for proper steady state and transient voltage division. Commutation of the SCR's is provided by capacitor C (Figure 2-75).

The interrupters operate immediately upon the development of a fault. Series inductors provide the energy necessary to clear the fault, as well as providing momentary, transient circuit isolation during faults. In order to minimize system weight, it is assumed that electromechanical switches for permanent circuit interruption are not required. The SCR interrupts the circuit between screen and the power bus in the event of an arc within

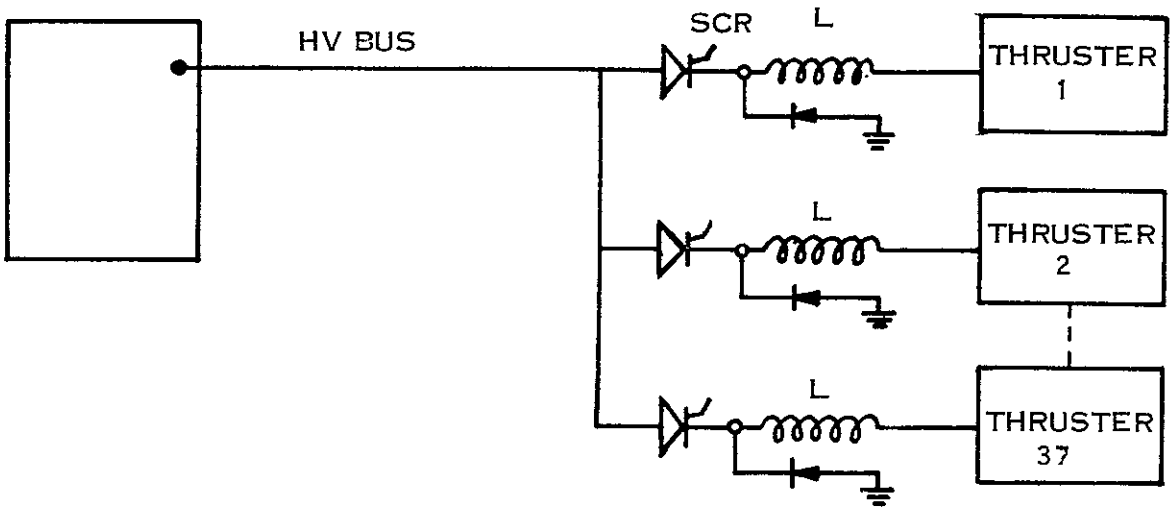

Figure 2-74. Individual Screen Circuit Interruption

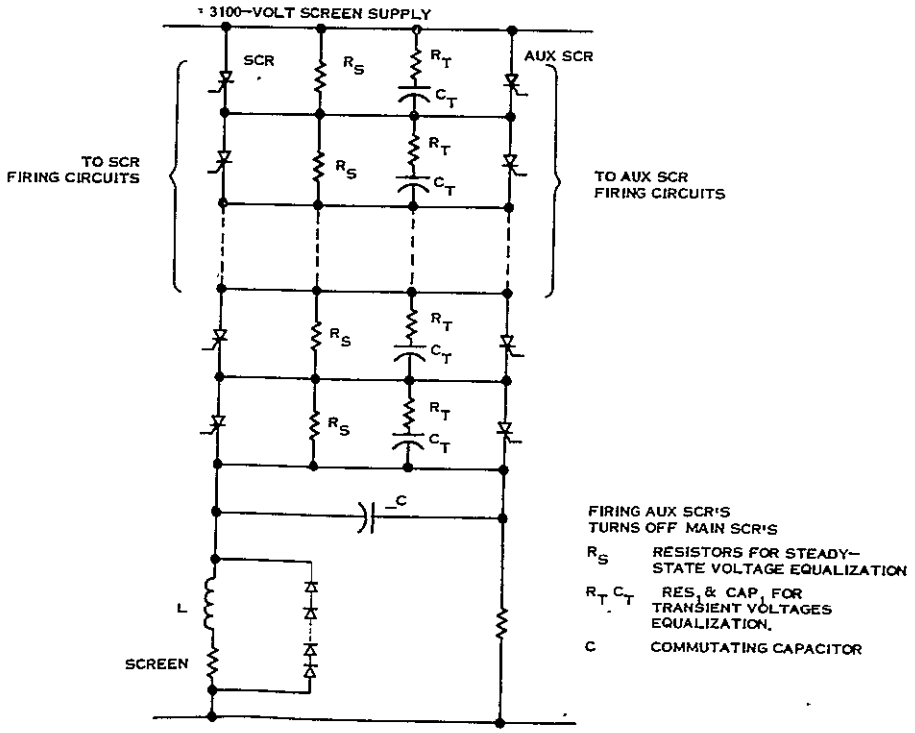

Figure 2-75. Typical Circuit, Screen Circuit Interrupter

176

the thrusters, as detected by a sudden drop in voltage at the screen, the appearance of voltage across the series reactor, L, or a commanded signal. Following circuit interruption by the SCR, energy stored in the inductor L continues to supply power to the arc for a period of up to two milliseconds. The SCR remains off for a period of 0.2 seconds to allow time for the arc to clear and the thruster conditions to return to normal. After 0.2 seconds, the SCR is again switched on, reestablishing screen voltage and hopefully restoring full thruster operation. If, for example, the arc restrikes two more times within a short period of time, the screen supply to that thruster and the inputs to the auxiliary power supplies for that thruster are permanently disconnected. This thruster is considered completely disabled and one of the six spare thrusters is automatically placed into operation to replace it.

During the spacecraft coast period when the thrusters are not required to operate, power to the thrusters is disconnected by the static switches in the screen supplies and by the contactors in the input circuits to the auxiliary thruster power supplies.

2.6.6.2.7 Auxiliary Power Conditioning - EM Pump Power Conditioning - There are five EM pumps in the system; four of which are used in the MHD power system. Largest is the cesium pump, being rated for 18.3 kW. The other pumps, which are two auxiliary pumps and a propellant pump, are rated at 0.35 kW each. Batteries supply the fifth pump, which is used only for MHD startup.

The cesium pump design requires three phase 60 Hz power for proper operation. Alternating current power was selected because of the power availability and because the development of high power ac pumps is more advanced than dc pumps.

There are several methods by which the desired voltage and frequency can be obtained from the MHD output. Dynamic conversion using a motor generator is undesirable because of the inherent weight of low frequency machinery. Static conversion by use of standard power conditioners is not recommended to change from 326 Hz to 60 Hz because of unnecessary losses and because of the large capacitor weight.

For power conditioning for the cesium pump, a cycloconverter (synchronous static frequency divider) is selected. The cycloconverter reduces the generator frequency to the 60 Hz range suitable for the pump. A transformer may be necessary to reduce the generator output voltage to the voltage required by the pump, however analysis is not complete.

A cycloconverter is a means of changing the frequency of alternating power using controlled rectifiers which are ac line commutated. The basic block diagram of a cycleconverter is shown in Figure 2 76. The function of the logic circuit is to provide the control turn-on signal for the SCR's in the proper time and sequence.

The silicon control rectifier circuit of the cycloconverter shown in Figure 2-77 is the circuit which handles the power and produces the low frequency output voltages. These low frequency output voltages are obtained by alternately providing a series of positive dc voltages and then a series of negative dc voltages from the high frequency (326 Hz) input to each phase of the output.

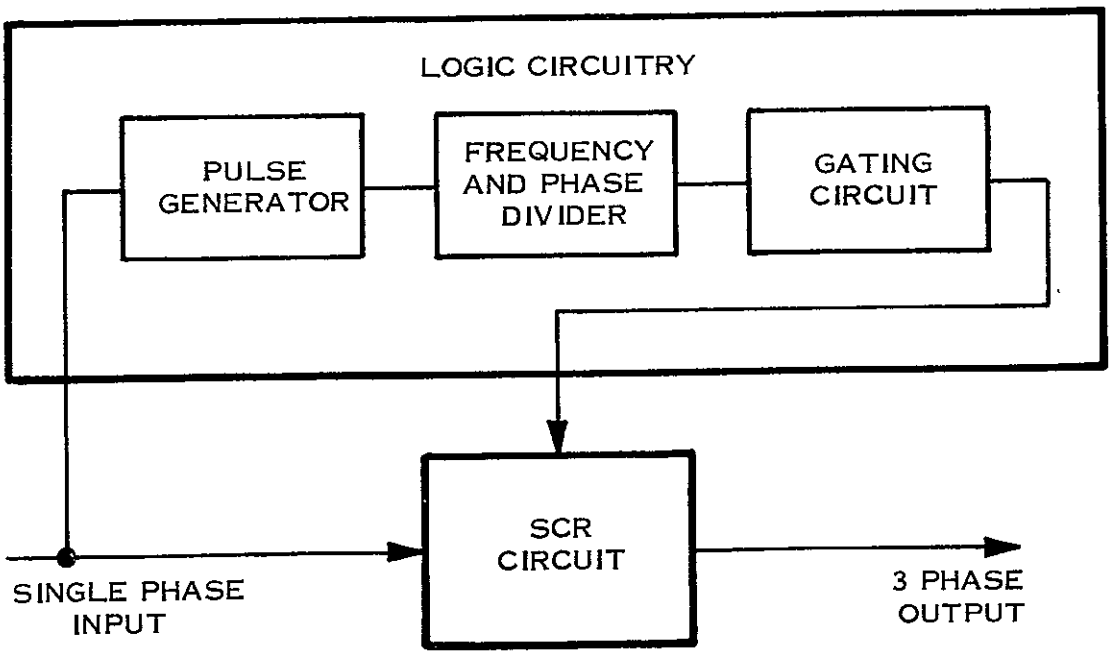

Figure 2-76. Block Diagram, Cycloconverter

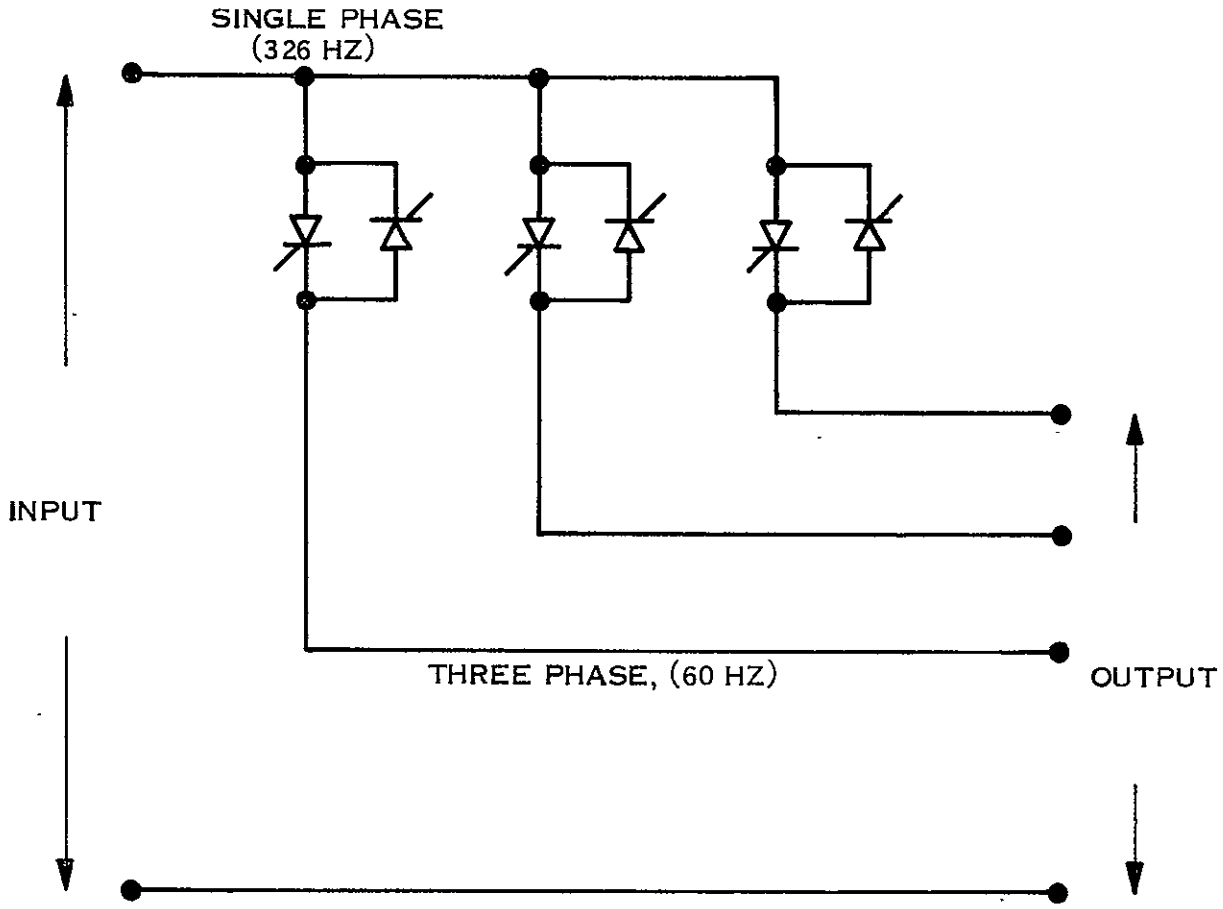

Figure 2-77. Cycloconverter SCR Circuit

The method of operation is apparent by referring to Figure 2-78, a single phase part of the three phase system (Reference 29).

Thus, if SCR_1 and SCR_2 are triggered, the dc output would be in the polarity shown in Figure 2-78. If SCR_3 and SCR_4 were triggered instead, the output polarity would be reversed. Thus, by alternately triggering the SCR pairs at a frequency lower than the supply frequency, a square wave of current would flow in the load resistor. A filter would be needed to eliminate the ripple, if necessary.

In order to produce a sine wave output, the triggering of the individual SCR's would have to be delayed by varying degrees so as to produce the waveform shown in Figure 2-79.

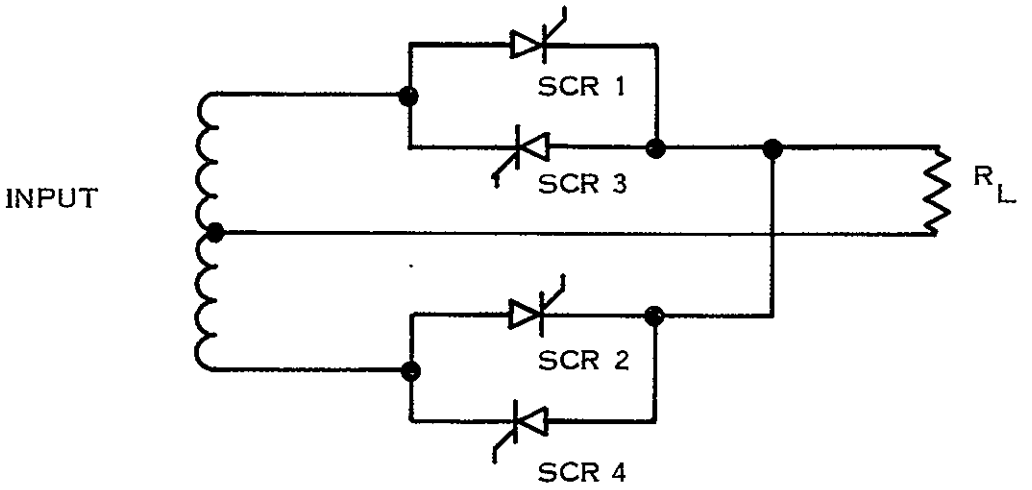

Figure 2-78. Single Phase Cycloconverter

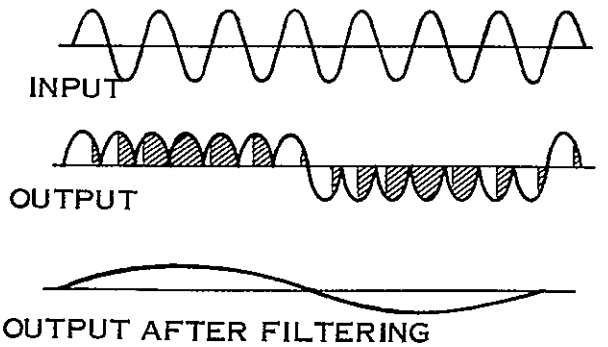

Figure 2-79. Single Phase Cycloconverter Waveforms

With the use of a cycloconverter, the generator windings need not be rated at the full kVA load of the pump, nor are capacitors required to supply the VAR because of the inherent power factor correcting capability of the cycloconverter. This correction is due to the fact that the energy stored in the magnetic field of the load is constantly being shifted by the frequency converter from one low frequency phase to another without going back to the generator (Reference 26).

Estimates of the characteristics of the cycloconverter are based upon a design reported in Reference 26; the weight is taken as 40 pounds, efficiency as 97 percent and the size 8 x 6 x 10 inch.

Control of the cesium pump and consequently control of the MHD generator output voltage, can be accomplished by electronically delaying the firing of the SCR's in the frequency divider to provide a lower rms voltage.

The auxiliary pumps and the propellant pumps are direct current conduction pumps (see Paragraph 2.6.3.4) and therefore require power at relatively low voltage, $\leq$ 1 volt dc. Using conventional power conversion techniques to transform the system's ac output to dc at such low voltage, efficiencies of less than 50 percent are encountered. With ac-dc conversion, the voltage drop in the output rectifiers approximates or exceeds the output voltage. Since these dc EM pumps are quite small, $\sim$ 350 watts each, the penalty of even low efficiency power conversion is negligible; therefore, it was assumed that all three normally operating pumps (two cooling pumps and the propellant pump) are provided with power from the low voltage dc bus with power conditioning efficiency assumed to be 0.35.

Auxiliary power conditioning is also required for the following operations:

a. Reactor control

b. Special ion engine units

c. Spacecraft guidance control

d. Payload

Table 2-31 shows the weight and efficiencies for the auxiliary power conditioners. The weights presented for the special ion thruster units are those provided by JPL. No losses are shown for the special ion engine units, since this power loss is already factored into the ion thruster efficiency used to calculate the beam power.

Table 2-31. Auxiliary Power Conditioning Characteristics

Component Application	Power Input kWe	Power Conditioning Efficiency, %	Weight Pounds	Losses Watts
Main EM Pump	18.9	97	40	550
Auxiliary EM Pumps, MHD bay	2.0	35	10	1300
Propellant Pump	1.0	35	5	650
Reactor Control	1.1	90	15	100
Special Ion Engine Units	16.1	90	272	(see text)
Payload Units				
Science	1.0	90	10	100
Guidance	0.5	90	10	50
Control	0.5	90	10	50

2.6.6.2.8 Startup Batteries - Three EM pumps are required for MHD power system startup. These are the two auxiliary pumps for coolant circulation and a lithium circulation pump. The lithium startup pump requires 350 watts for 8 hours at about 0.7 volts dc, which is 2800 watt-hours of energy. Since the main electrical power is not yet available,

the startup energy must be supplied by batteries. The two auxiliary cooling pumps together are assumed to require similar energy, and will double the battery requirement.

Two types of batteries could be used: silver zinc or silver cadmium, the latter was selected because of recharge capability. To supply the necessary energy, 18 cells are connected in parallel, supplying 2800 ampere-hours at one volt. Each cell has 150 ampere-hour capacity, measuring 1.7 x 5.5 x 7.6-inch, and weighing 5.8 pounds. Total weight for each of the two sets is 120 pounds with 14 pounds allowed for mounting, casing, and potting. Total size is 12.6 x 18.3 x 8.6-inch each set.

2.6.6.2.9 Electrical Cable Design - Five major sets of power distribution cables are required for the MHD electrical system. Cables conduct power from the generator to the transformer/inverters in the thrusters section, excitation cables from generator to capacitors, from the inverters forward to the EM pumps, from the inverters to the high voltage ion engines, from the inverters to the engine auxiliary power conditioners and payloads.

Cable optimization is not complete; however, the following estimates have been made:

Cable Designation	Weight Pounds	Power Loss Watts
Inverter Cable	100	270
Excitation Cables	150	---
High Voltage Cables	5	40
Low Voltage - EM Pumps	50	150
Low Voltage - Engine Aux, Payloads	15	40

2.6.7 MISSION ANALYSIS

A preliminary appraisal of the mission capabilities of the baseline design spacecraft was made. Using terminology recommended by the NASA-OART electric propulsion systems analysis task group, the spacecraft initial mass, m_o, is defined as:

$$m_o = m_{ps} + m_p + m_t + m_n$$

where the masses are

m_{ps} = low thrust propulsion system

m_p = propellant

m_t = tankage

m_n = net spacecraft (guidance, thermal control, attitude control, telecommunications, structure, science, etc.) - includes the science payload, m_L

The propulsion system is further broken down:

$$m_{ps} = m_w + m_{ts}$$

where these masses are

m_w = power subsystem

m_{ts} = thrust subsystem

Drawing from the detailed weight breakdown (Table 2-15) of the baseline design, these masses are given in both pounds and kilograms in Table 2-32.

Table 2-32. MHD Baseline Spacecraft Mass Definitions

Item	Pounds - Mass - kg.	
m_o initial mass	35,670	16,180
m_{ps} low thrust propulsion system	18,600	8,440
m_w power subsystem	15,810	7,170
m_{ts} thrust subsystem	2,790	1,270
m_p propellant	14,500	6,580
m_t tankage	230	100
m_n net spacecraft	2,340	1,060
m_l science payload	2,065	940

Figure 2-80 shows a simple block diagram of the systems electrical energy flow and the derivation of the baseline design system's specific mass. The figure of merit, α, is there defined in two ways; the propulsion system specific mass, α (or α_ϵ), is 77.5 lb/kWe, while the power system specific mass, α_W, is 66 lb/kWe.

Figure 2-81 shows the reference mission profile for low energy earth escape and thrust-coast-thrust flight to achieve orbit around Jupiter. There are two orbits around Jupiter which were considered: a high orbit at 11.7 million miles and a low orbit at 2.62 million

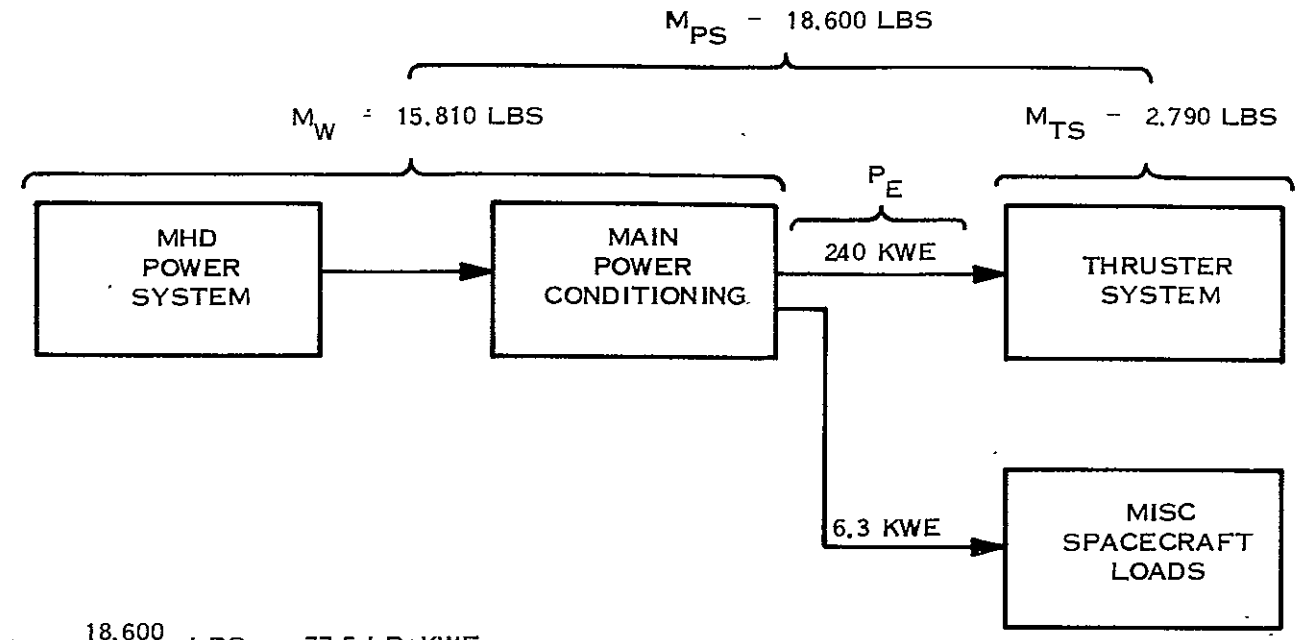

α - $\frac{18,600}{240}$ LBS - 77.5 LB/KWE

α_W - $\frac{15,810}{240}$ LBS = 66 LB/KWE

Figure 2-80. Specific Mass Schematic

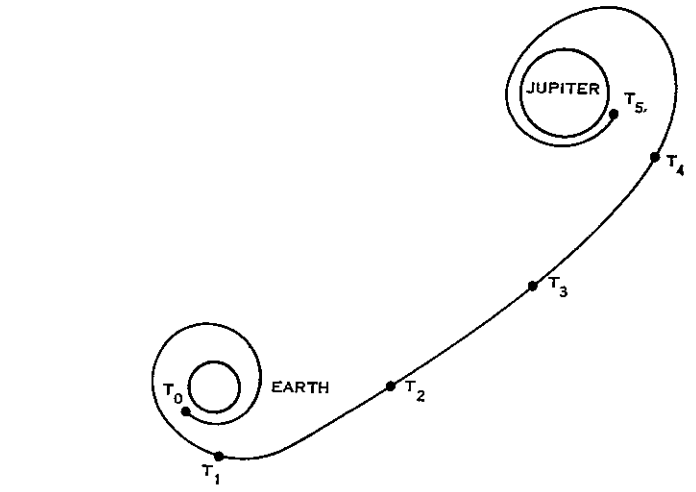

T_{ESCAPE}	$T_1 - T_0$
$T_{HELIOCENTRIC}$	$T_4 - T_1$
$T_{CAPTURE}$	$T_5 - T_4$
T_{THRUST}	$(T_2 - T_0) + (T_5 - T_3)$
T_{COAST}	$T_3 - T_2$
T_{TRIP}	$T_5 - T_0$

Figure 2-81. Reference Mission Profile

miles. In both cases, the orbit radius is measured from the center of the planet; for reference, the radius of Jupiter is 43,450 miles. For each of these terminal orbits a set of flight parameters was calculated, see Table 2-33, including the trip time. The specific impulse was varied from the 5000 second nominal for the thruster subsystem (Paragraph 2.2.2) to 4000 seconds and 6000 seconds to determine trip time sensitivity. The variation of required propellant mass fraction with trip time is plotted in Figures 2-82, 2-83, and 2-84 for each Jovian orbit and each of the specific impulse values. In Table 2-33 and in the three figures, the baseline design mass fractions used are corrected for the different propellant masses used; the thruster subsystem and tankage were adjusted in direct proportion to propellant flow rate.

From the plots, it is evident that the baseline design is capable of attaining the high Jupiter orbit in about 900 days; and cannot attain the low orbit around Jupiter in any reasonable trip time. Changes in specific impulse seem to affect launch weight requirements more than trip time.

A more detailed appraisal of mission capabilities cannot be made until the second half of this study when the variation of system specific mass with power level has been determined.

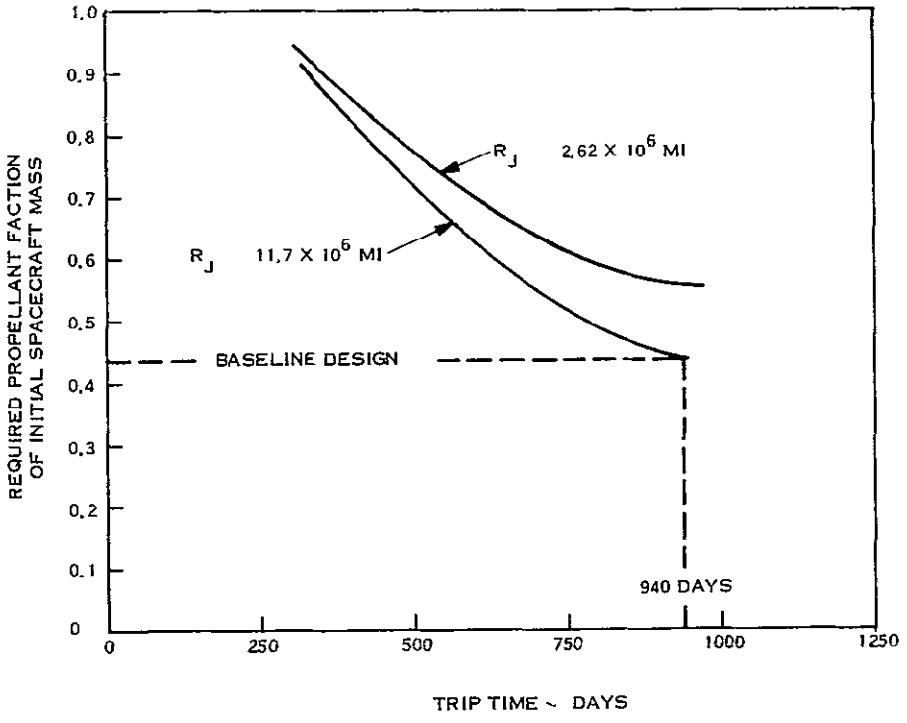

Figure 2-82. Propellant Mass Fraction vs. Trip Time, Isp = 4000 Seconds

TABLE 2-33. VARIATION OF TRIP TIME WITH SPECIFIC IMPULSE FOR BASELINE DESIGN

Specific Impulse (Sec)	Trip Time (Days)	Jupiter Orbit (10^6 mi)	Propellant Flow/Rate (lb/hr)	Required $1-\frac{m_p}{m_o}$	Required m_p/m_o	Adjusted Baseline Design m_o (lbs)
4000	360	11.7	1.6740	0.13677	0.86323	m_p/m_o = 0.43621
4000	540	11.7	1.6740	0.32796	0.67204	
4000	720	11.7	1.6740	0.47423	0.52577	940 days
4000	900	11.7	1.6740	0.55415	0.44535	38,376
4000	360	2.62	1.6740	0.10837	0.89163	m_p/m_o = 0.43621
4000	540	2.62	1.6740	0.25987	0.74013	
4000	720	2.62	1.6740	0.37578	0.62422	no trip
4000	900	2.62	1.6740	0.43911	0.56089	38,376
5000	360	11.7	1.3392	0.16843	0.83157	m_p/m_o = 0.39008
5000	540	11.7	1.3392	0.38523	0.61477	
5000	720	11.7	1.3392	0.53715	0.46285	890 days
5000	900	11.7	1.3392	0.51096	0.48904	34,331
5000	360	2.62	1.3392	0.13982	0.86018	m_p/m_o = 0.39008
5000	540	2.62	1.3392	0.31979	0.68021	
5000	720	2.62	1.3392	0.44591	0.55409	no trip
5000	900	2.62	1.3392	0.51096	0.48904	34,331
6000	360	11.7	1.1159	0.19799	0.80201	m_p/m_o = 0.35276
6000	540	11.7	1.1159	0.43366	0.56634	
6000	720	11.7	1.1159	0.58675	0.41325	825 days
6000	900	11.7	1.1159	0.66213	0.33787	31,633
6000	360	2.62	1.1159	0.16954	0.83046	m_p/m_o = 0.35276
6000	540	2.62	1.1159	0.37135	0.62865	
6000	720	2.62	1.1159	0.50244	0.49756	no trip
6000	900	2.62	1.1159	0.56699	0.43301	31,633

Note: All of above values are for 10,000 hour thrust time and a science payload of one metric ton.

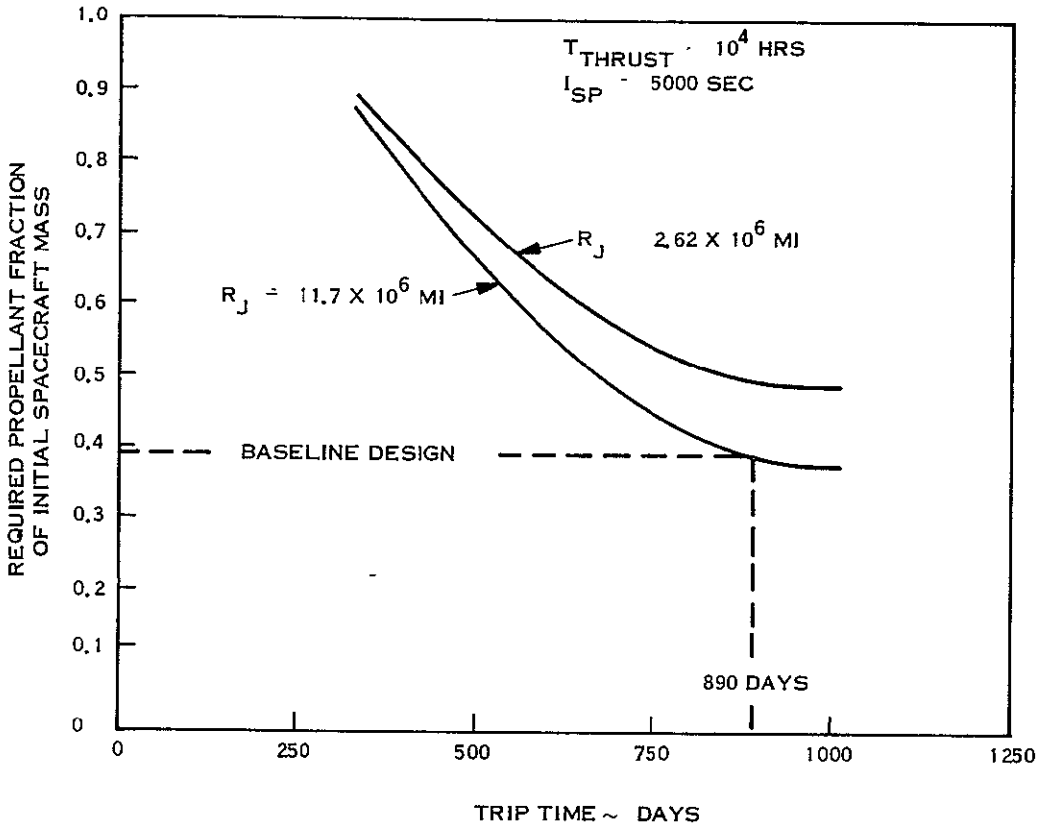

Figure 2-83. Propellant Mass Fraction vs Trip Time, Isp = 5000 Seconds

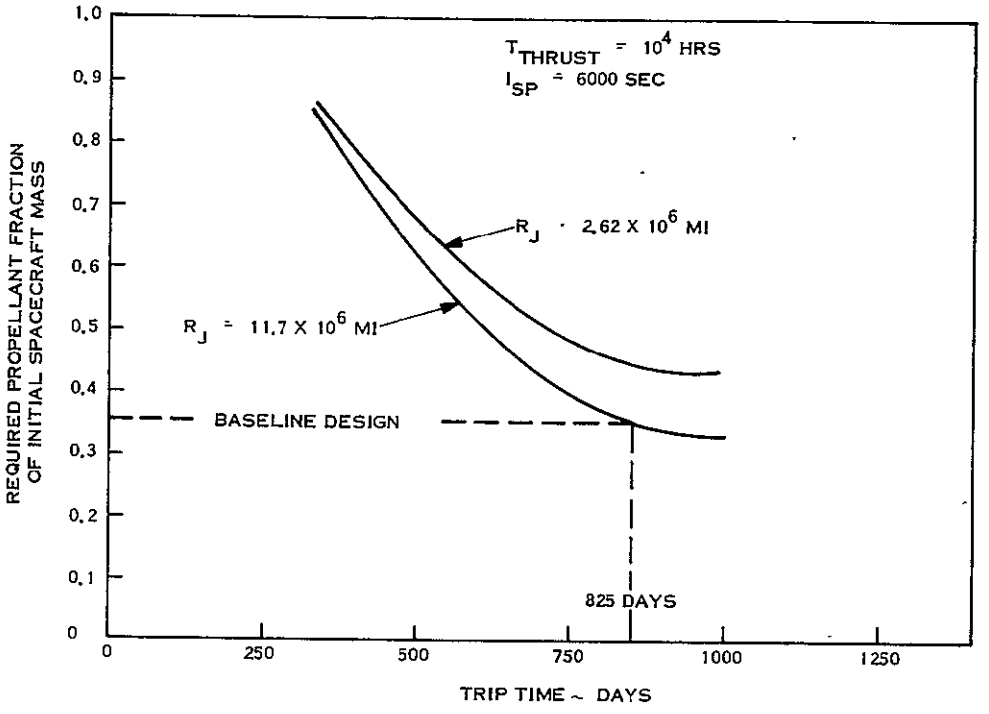

Figure 2-84. Propellant Mass Fraction vs. Trip Time, Isp = 6000 Seconds

3. CONCLUSIONS

4. RECOMMENDATIONS

5. NEW TECHNOLOGY

6. REFERENCES

3. CONCLUSIONS

From review of the work done in the first half of Phase I and evaluation of the baseline design system, the following conclusions are drawn:

1. The one-loop MHD system is more attractive than a two-loop configuration, although coolant activation by irradiation or fission produce leakage from reactor fuel elements might require the use of a two-loop system. The problems should be reappraised when more reactor data are available.

2. In order to shut down the MHD system during the flight coast period and Jupiter orbit operations, it would be necessary to provide an auxiliary power system to provide hotel load and payload power. The inclusion of shutdown and restart capability and a separate power system requires a more complex plant design. On the other hand, it is not unreasonable to assume that the MHD system can be operated at reduced power levels. If it cannot, a relatively small power-flattening shunt can be incorporated. Therefore, the system should be designed for continuous operation.

3. The rectangular channel vapor chamber using sodium working fluid is the most attractive design for the primary radiator. The triform geometry appears most attractive for the direct condensing vapor chamber radiator, since auxiliary structure is most easily incorporated and most easily jettisoned from it. The radiator net weight can then be minimized for both launch and electric-propelled flight.

4. The baseline design system exceeds the Titan III C/7 payload capability by about 7500 pounds or about 25 percent, and its length of 82 feet is slightly greater than the maximum allowed for the existing launch facilities. Neither excess is of alarming proportion when considered against normal growth or uprating of launch vehicles and their facilities in the ten year span needed to develop a flight MHD power system.

5. The reactor for the MHD power system is defined on the basis of data generated in the SNAP-50 Program about five years ago. Developments or studies since that time may indicate changes in the reactor design which will significantly affect MHD power system design, such as: larger core diameter requiring a larger shield, or a greater vulnerability to fission product leakage requiring an intermediate loop. Also of concern in reactor design is the fact that a reactor of this type would be developed not solely for the MHD power system but for other power systems (e.g., Potassium Rankine and Brayton) and manned missions as well. Consequently, the standard fast reactor developed might very well not be a slender, radiatively-cooled type but rather a short squat device with rotating drum controls and an active cooling system for the control drum assembly. All of the changes expected or possible in reactor design would involve design penalties on the MHD power system.

6. The MHD generator has a number of design features which require further investigation or development work, among them are:

   a. The duct wall separating the lithium flow from the stators. As was shown in the generator discussion, a continuous metal wall of any credible thickness is simply not acceptable; it would impose very large eddy current losses.

   b. The tapered winding slots in the generator stators become too narrow for acceptable conductor shapes and insulation systems near the outlet end of the generator. It may be necessary to design the generator with more conventional rectangular slots.

   c. Generator analysis is optimistic in calculating electrical losses in the windings. In particular, the percentage of slot area assumed to be conductor is high. Assumption of a lower area fraction would increase either weight or winding loss and might require a lower number of turns per slot with lower slot voltage. This last might have serious consequences for excitation capacitor design. Lower conductor area would also make coil cooling more difficult.

7. The MHD nozzle weight was calculated somewhat optimistically but is still high. Conversations with Dr. Elliott at JPL indicate that the wide shallow shape which was assumed to be necessary for successful impingement separation is probably not necessary. A more square shape makes design for creep stress much easier.

8. In the baseline design, it was assumed that the impinging nozzles could successfully separate the liquid and vapor phases without friction loss. It may be necessary to use a separator of some sort to achieve adequate separation. This would add to the system's frictional losses and thereby reduce system efficiency.

9. The payload section of the spacecraft appears to be very small compared to the whole 82 foot length. However, the payload bay has a volume of 95 cubic feet and an outside surface area of 40 square feet, both of which are considered reasonable for a payload of one metric ton. The size of the payload bay can be increased significantly without significant increase in the spacecraft weight.

10. The high specific mass of the MHD power system seems to require greater trip times than originally assumed. The increase in trip time can be of real significance to time related design problem areas - radiation exposure, creep stress, erosion, etc.

4. RECOMMENDATIONS

The following recommendations are made based on the first half work and the specific conclusions drawn in Section 3.

1. Use the baseline design as depicted for the parametric evaluations of the second half--i.e., a one-loop, continuously operating system using a triform vapor chamber radiator.

2. In the second half consider the effects of changes in reactor design on the MHD system.

3. In the second half consider the effects of reducing the number of conductors per MHD generator slot and the winding packing fraction.

4. In the parametric analysis of the second half, consider the effects of vapor-liquid separator inefficiency on overall design.

5. TECHNOLOGY

No new technology items have been identified.

6. REFERENCES

1. GESP-7011, A Design Study For a Thermionic Reactor Power System For a Nuclear Electric Propelled Unmanned Spacecraft, Quarterly Progress Report Number 1, May 23, 1969.

2. Thrust Subsystem Design for Thermionic-Electric Spacecraft Study, JPL Memo T. Masek to N. Simon, February 20, 1969.

3. Elliott, David G., "Variable-Velocity MHD Induction Generator With Rotating-Machine Internal Electrical Efficiency", AIAA Journal, Volume 6, Number 9, pp. 1695 - 1702, September 1968.

4. GESP-7017, A Design Study For A Magnetohydrodynamic Power System for a Nuclear Electric Propelled Unmanned Spacecraft, Quarterly Progress Report Number 1, September 1969.

5. Pierson, E. S. and Jackson, W. D., "The MHD Induction Machine," TR AFAPL-TR-107, May 1966, Air Force Aero-Propulsion Lab., Wright-Patterson Air Force Base, Ohio.

6. Elliott, D. G. et al., "Theoretical and Experimental Investigation of Liquid-Metal MHD Power Generation", Electricity from MHD, Vol. II, International Atomic Energy Agency, Vienna, 1966, pp. 995 - 1018.

7. Cerini, D. J. and Elliott, D. G., "Performance Characteristics of a Single-Wavelength Liquid-Metal MHD Induction Generator with End-Loss Compensation," AIAA Journal, Vol. 6, No. 3, March 1968, pp. 503 - 510.

8. Elliott, D. G., "Effect of Slots on MHD Induction Generator Efficiency", Tenth Symposium on Engineering Aspects of Magnetohydrodynamics, pp. 51-52, Cambridge, Mass., March, 1969.

9. Elliott, D. G., and Weinberg, E., "Acceleration of Liquids in Two-Phase Nozzles," Technical Report 32 - 987, Jet Propulsion Laboratory, Pasadena, Calif., July 1, 1968.

10. Reneau, L. R., Johnston, J. P., and Kline, S. J., "Performance and Design of Straight, Two Dimensional Diffusers, " Report PD-8, Department of Mechanical Engineering, Stanford, Calif., September 1964.

11. GESP-7013, A Design Study For a Thermionic Reactor Power System For A Nuclear Electric Propelled Unmanned Spacecraft, Quarterly Progress Report No. 2, August, 1969.

12. GE-PIR Number U-1K25-072, J. Garrity, J. Cokonis to W. A. Prickett, Addendum to Structural/Dynamic Analysis of Thermionic Spacecraft Configurations, August 4, 1969.

13. PWAC-445, Preliminary Design of the 2 MWT Reactor and Shield (PWAR-20) For The SNAP-50/SPUR Powerplant, December 30, 1964.

14. PWAC-643, SNAP-50/SPUR Program Engineering Progress Report, July 1, 1964 to September 30, 1964.

15. PWAC-457, 35 and 300 kWe SNAP-50/SPUR Powerplants for the Manned Orbiting Space Station Application.

16. Letter from F. R. Mynatt(ORNL) to W. Z. Prickett (G. E.) dated September 23, 1969.

17. Hays, L. G., and Cerini, D. J., Liquid Metal Magnetohydrodynamic Power Conversion NASA-JPL Space Programs Summary, Vol. III, 37 - 49 and 37 - 50, February 1968 and April 1968.

18. Calculations of Can Losses in Canned Motors, R. C. Robinson, I. Rowe, L. E. Donelan, Paper 57 - 134, AIEE Winter General Meeting, New York, January, 1957.

19. General Electric Medium A. C. Motor Department Design Data Curve No. 144 HA 406 revised, R. G. Rhudy/G. Angst.

20. Performance and Design of Alternating Current Machines, M. G. Say and E. N. Pink, Pitman and Sons, London, 1936.

21. Final Report - Potassium Turboalternator Design Study, Contract NAS 3-10933, November 1969.

22. Elliott, D. G. and Weinberg, E., JPL Technical Report 32 - 987, "Acceleration of Liquids in Two-Phase Nozzles", July 1, 1968.

23. GEMP-685, R-69-NSP-9, Creep-Rupture Data for the Refractory Metals to High Temperature, March, 1969.

24. Heller, J. A., Moss, T. A. and Barna, G. J., 4th Intersociety Energy Conversion Engineering Conference, pp. 465 - 483, Washington, D. C., September 1969.

25. R 65SD3010, Electromagnetic Alkali Metal Pump Research Program, R. G. Rhudy and J. P. Verkamp, September, 1965.

26. NASA CR-911, Design Two Electromagnetic Pumps, G. E. Diedrich and J. W. Gahan, November 1967.

27. ALO 3632-39, UC-33, Union Carbide Corporation Linde Division, Quarterly Progress Report of Research and Development in a Thermal Insulation Study, December, 1968 to February 1969.

28. Seely, S., Electronic Engineering, McGraw-Hill.

29. General Electric Silicon Controlled Rectifier Manual, Fourth Edition.

GENERAL ELECTRIC
SPACE DIVISION
SPACE SYSTEMS ORGANIZATION